

NEAR-INFRARED POLARIMETRY IN THE GALACTIC CENTER

ON PROPERTIES OF SAGITTARIUS A* AND A DUSTY S-CLUSTER OBJECT

INAUGURAL-DISSERTATION

zur

Erlangung des Doktorgrades
der Mathematisch-Naturwissenschaftlichen Fakultät
der Universität zu Köln



vorgelegt von

BANAFSHEH SHAHZAMANIAN SICHANI
aus Isfahan, Iran

Köln 2016

Berichtersteller:

Prof. Dr. Andreas Eckart
Prof. Dr. J. Anton Zensus

Tag der letzten mündlichen Prüfung: 30.10.2015

ABSTRACT

Near-infrared polarimetry observation is a powerful tool to study the central sources at the center of the Milky Way. My aim of this thesis is to analyze the polarized emission present in the central few light years of the Galactic Center region, in particular the non-thermal polarized emission of Sagittarius A* (Sgr A*), the electromagnetic manifestation of the super-massive black hole, and the polarized emission of an infrared-excess source in the literature referred to as DSO/G2. This source is in orbit about Sgr A*.

In this thesis I focus onto the Galactic Center observations at $\lambda = 2.2 \mu m$ (K_s -band) in polarimetry mode during several epochs from 2004 to 2012. The near-infrared polarized observations have been carried out using the adaptive optics instrument NAOS/CONICA and Wollaston prism at the Very Large Telescope of ESO (European Southern Observatory). Linear polarization at $2.2 \mu m$, its flux statistics and time variation, can be used to constrain the physical conditions of the accretion process onto the central super-massive black hole. I present a statistical analysis of polarized K_s -band emission from Sgr A* and investigate the most comprehensive sample of near-infrared polarimetric light curves of this source up to now. I find several polarized flux excursions during the years and obtain an exponent of about 4 for the power-law fitted to polarized flux density distribution of fluxes above 5 mJy. Therefore, this distribution is closely linked to the single state power-law distribution of the total K_s -band flux densities reported earlier by us.

I find polarization degrees of the order of $20\% \pm 10\%$ and a preferred polarization angle of $13^\circ \pm 15^\circ$. Based on simulations of polarimetric measurements given the observed flux density and its uncertainty in orthogonal polarimetry channels, I find that the uncertainties of polarization parameters under a total flux density of ~ 2 mJy are probably dominated by observational uncertainties. At higher flux densities there are intrinsic variations of polarization degree and angle within rather well constrained ranges. Since the emission is most likely due to optically thin synchrotron radiation, the obtained preferred polarization angle is very likely reflecting the intrinsic orientation of the Sgr A* system i.e. an accretion disk or jet/wind scenario coupled to the super-massive black hole. Our pola-

rization statistics show that Sgr A* must be a stable system, both in terms of geometry, and the accretion process.

I also investigate an infrared-excess source called G2 or Dusty S-cluster Object (DSO) moving on a highly eccentric orbit around the Galaxy's central black hole, Sgr A*. I use for the first time the near-infrared polarimetric imaging data to determine the nature and the properties of DSO and obtain an improved K_s -band identification of this source in median polarimetry images of different observing years. The source starts to deviate from the stellar confusion in 2008 data and it does not show a flux density variability based on our data set. Furthermore, I measure the polarization degree and angle of this source and conclude based on the simulations on polarization parameters that it is an intrinsically polarized source with a varying polarization angle as it approaches Sgr A* position. I use the interpretation of the DSO polarimetry measurements to assess its possible properties.

ZUSAMMENFASSUNG

Polarimetriemessungen im nahen Infrarotwellenlängenbereich stellen eine sehr effektive Methode dar, die Strahlungsquellen im Zentrum der Milchstrasse zu untersuchen. Ziel meiner Dissertation ist es diese polarisierte Strahlung im zentralen Lichtjahr zu analysieren. Dies betrifft insbesondere die nicht-thermische, polarisierte Strahlung von Sagittarius A* (Sgr A*). Hierbei handelt es sich um eine Quelle, die mit dem supermassiven Schwarzen Loch im Zentrum der Milchstrasse assoziiert wird, sowie die polarisierte Emission der Infrarotexzessquelle, die als DSO/G2 bezeichnet wird. Diese Quelle befindet sich in einer Umlaufbahn um Sgr A*.

In dieser Arbeit konzentriere ich mich auf die Beobachtungen des galaktischen Zentrums bei einer Wellenlänge von $\lambda = 2.2 \mu\text{m}$ (K_s -Band), die im Polarimetriemodus über verschiedene Epochen in den Jahren 2004 bis 2012 durchgeführt wurden. Diese Polarimetriebeobachtungen wurden mit Hilfe des adaptiven Optik Systems NAOS/CONICA und einem Wollaston-Prisma am VLT (Very Large Telescope) der ESO (Europäische Südsternwarte) durchgeführt. Die lineare Polarisation bei $2.2 \mu\text{m}$, ihre Flussdichtestatistik und zeitliche Variabilität können benutzt werden, um den Akkretionsprozess auf das zentrale super-massive Schwarze Loch zu charakterisieren. Ich präsentiere eine statistische Analyse der Polarisationsmessungen von Sgr A* und untersuche dabei die bisher vollständigste Stichprobe von Lichtkurven der polarisierten Strahlung. Ich kann mehrere polarisierte Flußdichteausbrüche nachweisen und finde für Flußdichten oberhalb von 5mJy in der logarithmischen Darstellung des Häufigkeitsdiagramms der Flußdichteveriationen ein Potenzgesetz mit einer Steigung von 4. Diese Verteilung hängt daher eng mit dem Einzelzustands-Potenzgesetz der K_s -Band Flußdichteverteilung zusammen, welches bereits vorher von uns gefunden wurde.

Ich finde einen Polarisationsgrad von $20\% \pm 10\%$ und einen bevorzugten Polarisationswinkel von $13^\circ \pm 15^\circ$. Basierend auf Simulationen dieser Messungen, den beobachteten Flußdichten und ihren Meßfehlern in orthogonalen Meßkanälen, finde ich, daß die Unsicherheiten in der Bestimmung der Polarisationsparameter unterhalb einer Flußdichte von $\sim 2\text{mJy}$ durch Beobachtungsunsicherheiten dominiert wird. Für höhere Flußdichten

bewegen sich die intrinsischen Variationen von Polarisationsgrad und -winkel in wohldefinierten Grenzen. Da die Emission mit großer Wahrscheinlichkeit von optisch dünner Synchrotronstrahlung stammt, ist es auch sehr wahrscheinlich, dass der beobachtete bevorzugte Polarisationswinkel die intrinsische Orientierung des Sgr A*-Systems widerspiegelt: also eine Akkretionsscheibe oder ein Jet/Wind-Szenario welches mit dem supermassiven Schwarzen Loch gekoppelt ist. Unsere Polarisationsstatistik zeigt, dass Sgr A* sowohl in Bezug auf seine Geometrie als auch in Bezug auf den Akkretionsprozess ein stabiles System darstellen muß.

Ich untersuche ebenfalls die Infrarotexzess-Quelle genannt G2 oder DSO (Dusty S-cluster Object - staubiges Objekt im S-Sternhaufen), welches sich auf einer hochexzentrischen Umlaufbahn um das zentrale Schwarze Loch Sgr A* befindet. Zum ersten Mal benutze ich hier die infraroten Polarimetriedaten, um die Natur des DSO zu bestimmen. In Medianen von abbildenden Polarisationsmessungen der vergangenen Jahre konnte ich eine verbesserte Identifikation des DSO erzielen. Die Quelle löste sich im Jahre 2008 klar aus dem stellaren Konfusionshintergrund und zeigt unseren Daten nach keine signifikante Flußdichtevervariabilität. Weiterhin kann ich auf Grund von Simulationsrechnungen zeigen, dass die gemessenen Polarisationsgrade und -winkel quellintrinsisch sind. Während der Annäherung des DSO an Sgr A* zeigt die Quelle eine variable Polarisation. Ich nutze die Interpretation der Polarimetriemessungen des DSO zur Bestimmung seiner möglichen Eigenschaften.

CONTENTS

Contents	v
1 Introduction	1
1.1 The Galactic Center	1
1.2 Sagittarius A*	6
1.3 Radiation mechanisms of Sgr A*	7
1.4 Flaring activity of Sgr A*	9
1.5 The Dusty S-cluster Object (DSO/G2) at the GC	10
1.6 Polarization at the GC	11
1.7 Outline of the dissertation	12
2 Observation and Data Reduction	15
2.1 Observations	15
2.2 Adaptive Optics	17
2.3 Standard data reduction process	19
2.4 Deconvolution	20
2.4.1 PSF estimation	20
2.4.2 Lucy-Richardson deconvolution	21
3 K_s-band Near Infrared Polarimetry of Sgr A*	23
3.1 Introduction	23
3.2 Observations and data reduction	25
3.2.1 Flux density calibration	28
3.2.2 Polarimetry	31
3.3 Data analysis	34
3.3.1 Statistical behavior of polarization measurements	34
3.3.2 Polarization degree and polarization angle	42
3.3.3 Analysis of the polarized flux density distribution	47
3.3.3.1 Best fits of the polarized flux density distribution and the goodness of fit	48
3.3.3.2 The polarized flux density distribution for bright flare fluxes	49

3.3.3.3	A heuristic analytic explanation of the polarized flux density distribution	50
3.3.4	Relation between total flux density and polarization degree	53
3.4	Discussion	55
3.4.1	Mechanisms that contribute to the polarization	55
3.4.2	Variable polarized flux density	56
3.4.3	The preferred polarization angle	58
4	Near infrared polarized observations of the Dusty S-cluster Object (DSO/G2) at the Galactic Center	61
4.1	Introduction	61
4.2	Observations and data reduction	65
4.2.1	Position of the DSO	66
4.3	Results	68
4.3.1	Lightcurves	68
4.3.2	Polarimetry	68
4.4	Discussion	71
5	Summary and conclusion	75
	Bibliography	81
	List of Figures	99
	List of Tables	101
	List of Acronyms	103
	Acknowledgements	105
	Erklärung	107

INTRODUCTION

1.1 The Galactic Center

It is generally believed that super-massive black holes (SMBHs) exist at the center of most galaxies and the closest example is located at the center of our own galaxy, the Milky Way. The Galactic Center (GC) is a unique laboratory to study different astrophysical processes such as star formation, stellar dynamics, physics of the interstellar medium and emissions associated with the accretion into the closest SMBH, Sgr A*. The existence of a SMBH at GC, located at ~ 8 kpc or ~ 28000 light years away from us (Reid, 1993; Eisenhauer *et al.*, 2005; Ghez *et al.*, 2008), plays an important role in understanding of the physical processes and the interaction between black holes and their host galaxies. In this dissertation, I focus on Sgr A* and a dusty source in the near vicinity of the SMBH. However, before discussing them, I present a short introduction to the GC structures in a larger extent.

The Galactic Center is obscured by dust along the line of sight in the optical regime, therefore its observations are carried out at shorter or longer wavelengths. Figure 1.1 shows the central region of the Galaxy in different frequencies using different telescopes.

Sagittarius A (Sgr A) complex located at the nucleus of the Milky Way is the most luminous region in the image. The infrared radiation (red) comes from the stars and their winds that warm up the regions around them and lead to observing compact sources and filaments in the field of view (FOV). The star forming regions and many stars can be observed in the near-infrared (NIR) light (yellow). In the left side of the mosaic image, the Arches and

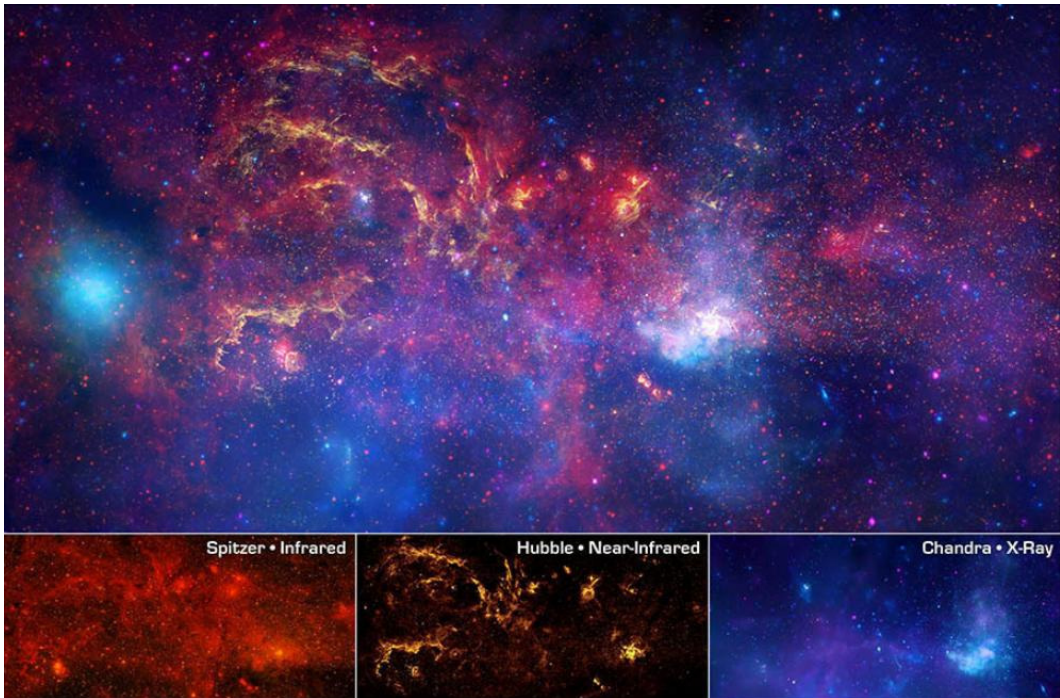


Figure 1.1: Composite image of the Galactic Center in near-infrared, infrared and X-ray (top) and the same region in the separate mentioned wavelengths (bottom). The center of the Galaxy is located within the bright white region to the right of and just below the middle of the images. The scale of the image is $40 \text{ pc} \times 30 \text{ pc}$. (from: Chandra X-ray observatory website. Credit for Chandra image: NASA/CXC/UMass/Q. D. Wang et al.; for Hubble image: NASA/ESA/STScI/Q. D. Wang (University of Massachusetts, Amherst); for Spitzer image: NASA/JPL-Caltech/SSC/S. Stolovy.)

Quintuplet massive stellar clusters heat the gas nearby to glow brightly as arc-like structures.

The X-ray emission (blue) arises from the very hot gas heated by outflows and winds of the central black hole and/or stellar explosions. The most luminous region in the X-ray is Sagittarius A. A zoom-in image of Sgr A complex in the X-ray can be seen in Fig. 1.2. Chandra observes a bright cloud at the very center where the radio point source, Sgr A* is located. Sgr A* is not separated from the structures around like Sgr A East due to the confined resolution of Chandra. Sgr A East has a shell-like structure and is a non-thermal X-ray/radio source which is thought to be a supernova remnant at the GC (Ekers et al., 1975, 1983). Sgr A East surrounds Sgr A west, which is a three-armed structure, the so-called mini-spiral, and a molecular ring called circumnuclear disk (CND). The CND with

a radius of about 1.5 to 5 pc and a mass of about a few $10^4 M_\odot$ (Genzel *et al.*, 1985; Mezger *et al.*, 1989; Requena-Torres *et al.*, 2012) contains dense molecular clouds ($10^4 - 10^7 \text{ cm}^{-3}$) (e.g., Guesten *et al.* (1987); Wright *et al.* (2001); Herrnstein and Ho (2002); Christopher *et al.* (2005) and few 100 K warm dust (Zylka *et al.*, 1995; Lau *et al.*, 2013)). The mini-spiral which is composed of ionized gas and dust, emits thermal emission (see Fig. 1.3). The projected motion of the ionized gas rotates around the center with a velocity of $\sim 100 \text{ km s}^{-1}$ at a distance of about 3 light years (Yusef-Zadeh *et al.*, 1998). If the gas rotation is on a Keplerian orbit around the center, the enclosed mass would be $\sim 3.5 \times 10^6 M_\odot$ which can be considered as a manifestation for the existence of a black hole at the GC. Most of the ionized material comes from the inner edge of the CND. There is an accumulation of stars forming the nuclear stellar cluster (NSC) at the center of the Galaxy. High resolution imaging facilities such as adaptive optics and Speckle imaging made a detailed observation of this cluster possible. Figure 1.4 shows a three color composite image of the NSC around Sgr A* taken in the NIR. Most of the stars of the nuclear cluster are old (super-)giants and asymptotic giant branch (AGB) stars. In addition, young stars with the mass of $30 - 100 M_\odot$ can be found in this region (Krabbe *et al.*, 1995; Genzel *et al.*, 1996; Paumard *et al.*, 2006). These hot young stars show Helium line emission from their exterior atmosphere and are called He-stars. They are massive blue super-giants and Wolf-Rayet (WR) stars with ages

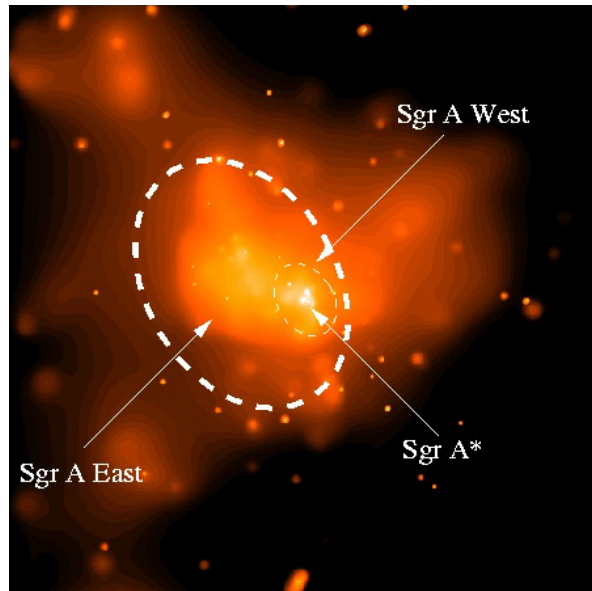


Figure 1.2: 1.5-3.0 keV band X-ray image of Sagittarius A complex observed by Chandra from the inner $\sim 20 \text{ pc} \times 20 \text{ pc}$ of the galaxy. Image credit: NASA Chandra X-Ray Observatory and Penn State University.

between 2 to 9 million years, which are dynamically unrelaxed due to their young age. The presence of young stars very close to the SMBH is not fully understood, since star formation in the central region should be suppressed due to the strong tidal interactions with the black hole. However, different scenarios have been suggested to describe the existence of young stars. One of the scenarios suggested by Jalali *et al.* (2014) using hydrodynamical simulations, shows that strong orbital compression of the clumps along their highly eccentric orbital motion around Sgr A* provokes the enhancement of the gas densities to the values higher than the tidal density of the SMBH. As a result, star formation can happen close to the black hole. One example can be IRS 13N, a compact group of stars located 0.1 pc away from Sgr A*, that is considered to host young stellar objects (YSOs) with ages of less than a million year (Eckart *et al.*, 2004, 2013; Mužić *et al.*, 2008).

A distinct distribution of young stars, called the S-stars, is located in the central arc-second. The S-stars are blue, massive, and mostly B main sequence stars with very high

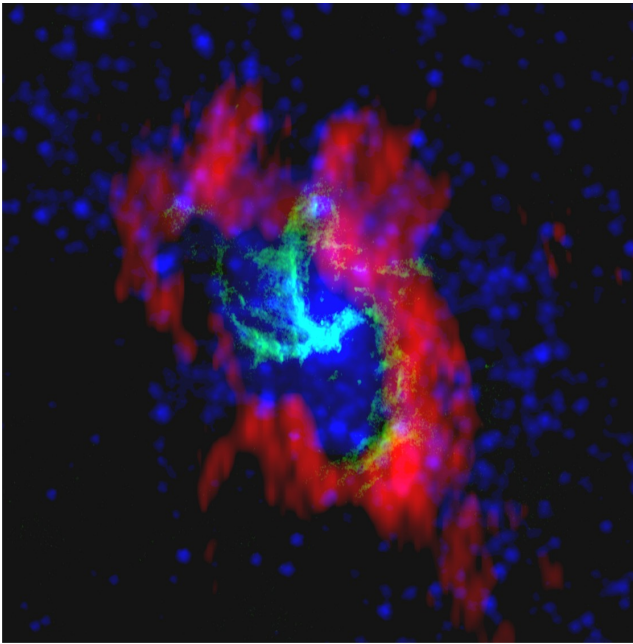


Figure 1.3: Multi-wavelength image of the central few parsecs of the Galactic Center. The observations are in radio ($\lambda = 1.2$ cm) by NRAO Very Large Array (green) and BIMA (red), and in infrared by NASA Spitzer Space Telescope (blue). The three-armed structure in radio (green) is the warm, ionized gas that is overlapped on the cold molecular HCN emission (red) coming from the CND. Stars are illustrated in blue. The image scale is $1.8'' \times 1.8''$. Image credit: NRAO/AUI.

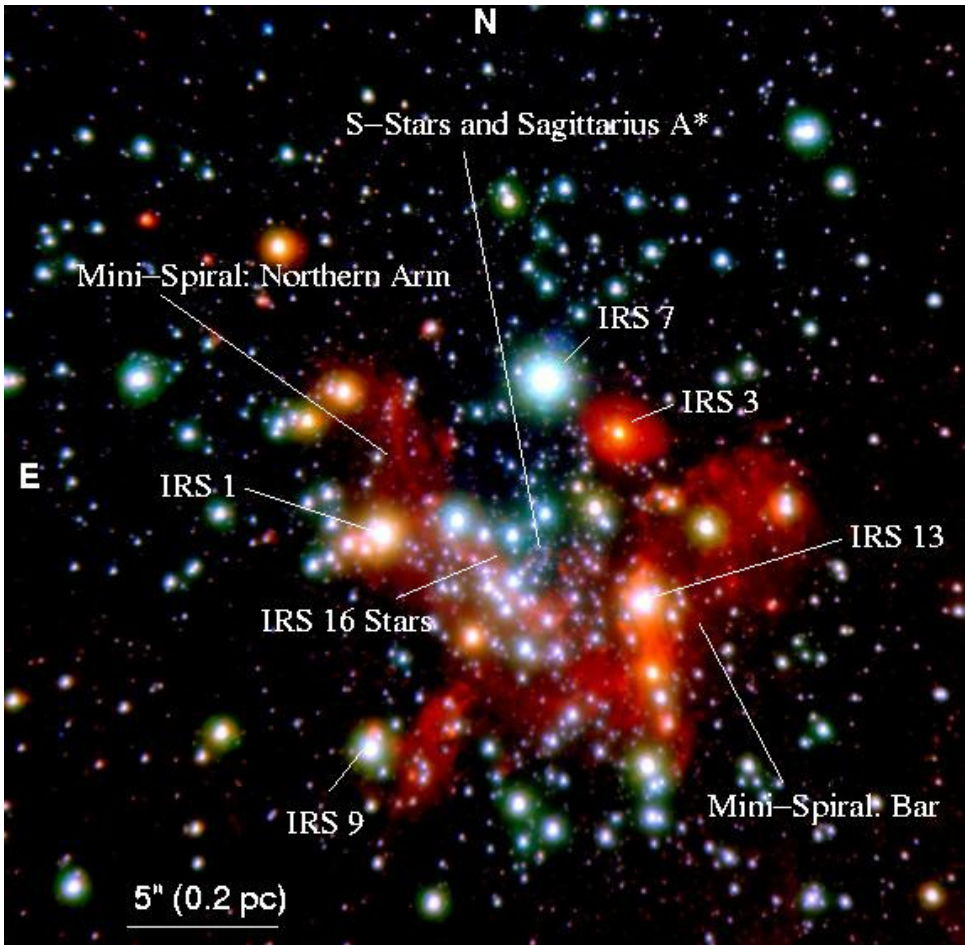


Figure 1.4: Composite image of H, K, and L' band (1.3, 2.2, and 4.1 μm) of the Galactic Center taken by NACO/Very Large Telescope (VLT). Image credit: University of Cologne.

velocities of a few thousand km s^{-1} (Eckart *et al.*, 1999; Ghez *et al.*, 2003; Eisenhauer *et al.*, 2005; Genzel *et al.*, 2010). The motion of the S-stars can trace the mass distribution in the central region. Eckart and Genzel (1996) presented for the first time the proper motions of these stars. The velocity dispersion of the central stars is dependent on their distance from Sgr A*, that can be compared to particles motion on Keplerian orbits around a point mass and in its potential field. Studying the S-stars by fitting Keplerian orbits to their motion (Schödel *et al.*, 2002, 2003; Ghez *et al.*, 2005a; Eisenhauer *et al.*, 2005), resulted in the strongest evidence so far for the compactness of the central dark mass.

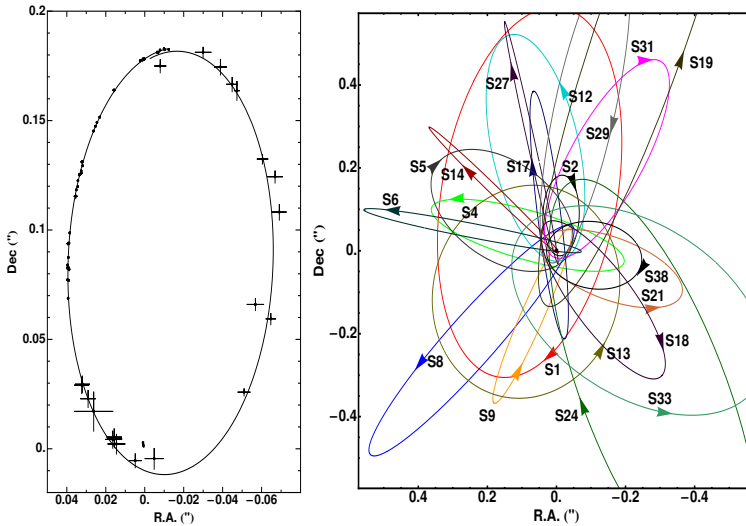


Figure 1.5: Left: orbital fit to astrometric positions of S2 for the observations between 1992 to 2008. Right: Stellar orbits around Sgr A* at the nuclear star cluster. Images courtesy: Gillessen *et al.* 2009.

1.2 Sagittarius A*

The massive dark mass at the center of the NSC, which is the best candidate for the closest black hole, is one of the most interesting objects at GC. For the first time Balick and Brown in 1974 detected this point source using 14-meter radio telescope at Huntresville and named it Sagittarius A* (Sgr A*). First high angular resolution observations using NIR adaptive optics (Eckart and Genzel, 1997; Schödel *et al.*, 2002; Ghez *et al.*, 2003) were mostly concentrated on estimating the central dark mass using the stellar orbits of the S-cluster. The orbital fits of the thirty S-stars at the center in NIR and the little proper motion of Sgr A*, measured by Very Long Baseline Interferometry (VLBI) observations (Backer and Sramek, 1999; Reid *et al.*, 1999) provided the most compelling evidence that Sgr A* is associated with a super-massive black hole of about four million solar masses (Schödel *et al.*, 2002; Eckart and Genzel, 1996, 1997; Ghez *et al.*, 2000; Eckart *et al.*, 2002; Eisenhauer *et al.*, 2003; Ghez *et al.*, 2005b, 2008; Gillessen *et al.*, 2009a). Gillessen *et al.* (2009b) had an update on this work when the star S2, which orbits Sgr A* with a period of about 15 years, completed one orbit between 1982 – 2008 and reported a mass of $4.4 \times 10^6 M_{\odot}$ (Fig. 1.5). Being a very bright and always visible radio source using radio interferometry enables us to do high resolution studies of Sgr A*. VLBI allows us also to investigate the source structure, though, the source size in the radio regime can be broadened through interstellar scattering. Sub-mm VLBI observations are very difficult because of deficient telescope

performance and weakened interferometry coherence. Another difficulty in using interferometers for GC observations is the fact that most of the radio telescopes are located in the northern hemisphere, while the GC is at a declination of -29° . With the available radio data, the intrinsic size of the source is derived by subtracting the interstellar scattering. The intrinsic size of Sgr A* at 3.5 mm is derived to be $13 R_s$ (Bower *et al.*, 2006), where R_s is the Schwarzschild radius, $R_s = 2GM/C^2$, and a black hole mass of $4 \times 10^6 M_\odot$ and a distance of 8 kpc to the GC have been considered. The very small size of Sgr A* provides further evidence for the black hole nature of this source.

1.3 Radiation mechanisms of Sgr A*

Sgr A* radiates below its Eddington limit with $L_{\text{Sgr A}^*} \sim 10^{-8.5} L_{\text{Edd}}$, in nearly all bands (Genzel *et al.*, 2010). The low luminosity of Sgr A* is due to its low accretion rate, which is lower than its Eddington accretion rate. Consequently, it is proposed to be inactive or a Low Luminosity Active Galactic Nucleus (LLAGN) (Contini, 2011; Eckart *et al.*, 2012b).

From the X-ray observations of the gas emission around Sgr A* the accretion rate is estimated to be $10^{-5} M_\odot \text{ yr}^{-1}$ (Baganoff *et al.*, 2003). It is so low that the standard accretion model (Shakura and Sunyaev, 1973) overestimates the Sgr A* luminosity. The low observed accretion rate of Sgr A* can be explained with a radiatively inefficient accretion flow (RIAF) model such as the Advection-Dominated Accretion Flow (ADAF) (Narayan *et al.*, 1995) or a short jet (Falcke and Markoff, 2000). All these models can fit the spectral energy distribution (SED) of Sgr A* in its steady state (see Fig. 1.6) over all observable frequencies.

In Fig. 1.6, the spectrum of Sgr A* is presented in the radio, NIR, and X-ray except in the optical and UV since extinction makes it un-detectable at these frequencies. The radio spectrum is described by synchrotron emission of thermal and non-thermal distributions of electrons. At the low frequencies (less than 10 GHz) the spectral index (α) of the spectrum is $0.1 - 0.3$ (the relation between the luminosity and the spectral index is presented as $L_\nu \propto \nu^\alpha$) which increases to 0.5 at higher frequencies (Falcke *et al.* 1998; Melia and Falcke 2001 and references therein). At lower frequencies, the emission radiates from an outer region which can be the halo around the black hole. The slope of the spectrum declines at the sub-mm regime and shows that the accretion region has changed from optically thick to optically thin ($\alpha < 0$). Since Sgr A* is highly variable in the NIR and X-ray domain (see Section 1.4), the spectral index changes with the flux density (Gillesen *et al.*, 2006; Hornstein *et al.*, 2006) and measuring the steady spectrum becomes impossible.

The X-ray emission is caused by thermal Bremsstrahlung and the second peak at high frequencies (UV, X-ray) is the result of the inverse Compton, up-scattering of the synchrotron radiation by the relativistic electrons (Genzel *et al.*, 2010). As mentioned before,

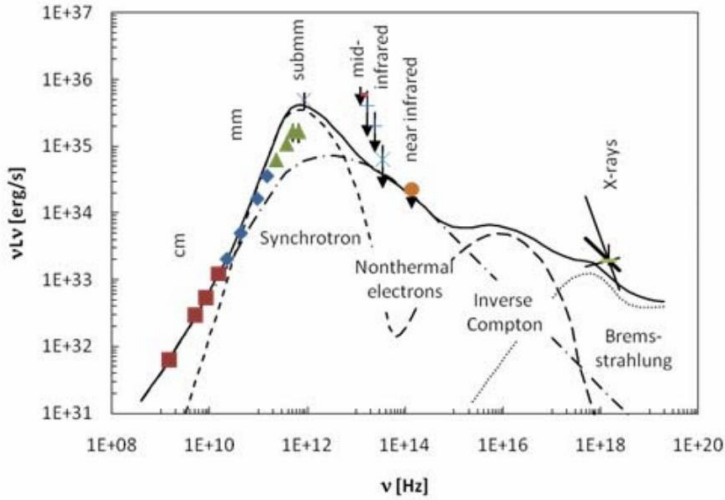


Figure 1.6: Spectral energy distribution of Sgr A* in its steady state. The dashed line at the radio frequencies represents the synchrotron emission from thermal electrons. It becomes flat at lower frequencies because of non-thermal electrons addition (dashed-dotted line). The synchrotron photons become up-scattered by thermal electrons and produce Inverse Compton radiation (long dashed line). The X-ray emission comes from Bremsstrahlung originating from the outlying part of the accretion stream (dotted line). Image credit: (Genzel et al., 2010) and references therein.

radiatively inefficient accretion flow model can describe the huge difference between the observed luminosity of Sgr A* and its Eddington luminosity.

Different RIAF models have been used to fit the observed SED. The ADAF model (Narayan and McClintock 2008 and references therein) includes a very hot, optically thin, geometrically thick accretion disk. In ADAF disks most of the energy is advected beyond the BH event horizon rather than being radiated, therefore they are much less luminous compared to the geometrically thin disks. Yuan et al. (2003) added non-thermal particles and an outflow to the initial ADAF. The nature of the outflow is still not clear, although according to theoretical studies it should exist. A non-thermal outflow which expands can be a jet. In the case of Sgr A*, a jet has not been detected yet - it may be hidden behind the scattering shield (Markoff et al., 2007) - or it is a non-collimated outflow. The structure of the radio source Sgr A* is consistent with a jet or an accretion disk based on the VLBA 7 mm observations (Bower et al., 2014). Observations in different wavelength regimes have not been able so far to confirm or reject the presence of a jet or an outflow originating from the Galaxy's central black hole. Broderick et al. (2009) showed that the observed SED of Sgr A* (Fig. 1.6) and the mm-VLBI size constraints indicate that this source has a horizon

without a solid surface.

1.4 Flaring activity of Sgr A*

Sgr A* is a highly variable source at all wavelengths. The source is always visible in the radio regime and can be seen continuously (Falcke *et al.*, 1998; Zhao *et al.*, 2001), while it is only visible in the NIR and X-ray bands, during its high activity states or so called flares (see Fig. 2.4 for NIR variability). The high confusion from the background in the NIR band (unresolved stars close to Sgr A*) and X-ray band (the diffuse background emission of the hot gas around Sgr A*) makes this source detectable only during the flare events (Sabha *et al.*, 2010). The cause of Sgr A* flares is not fully understood. The stellar wind from the stars orbiting this source supplies the accreting flow (Melia, 1992; Coker and Melia, 1997; Rockefeller *et al.*, 2004; Cuadra *et al.*, 2005, 2006, 2008). The sudden outbursts, or flares, might be the result of hypothetical acceleration or shocks (jets), or magnetic reconnection very close to the black hole (Markoff *et al.*, 2001; Liu and Melia, 2002; Liu *et al.*, 2004; Marrone *et al.*, 2008).

The X-ray flare activity occurs with the NIR flares simultaneously (Eckart *et al.*, 2004; Marrone *et al.*, 2008; Dodds-Eden *et al.*, 2009). Eckart *et al.* (2012a) reported synchrotron and synchrotron self-compton (SSC) mechanisms to be responsible for the simultaneous NIR and X-ray variability. In this model, the NIR radiation is dominated by a synchrotron spectrum that shows a transition from optically thick emission at a few hundred GHz to optically thin emission at one THz. The X-ray outbursts are connected to these NIR flares through the inverse Compton scattering of the synchrotron photons by the same population of the relativistic electrons that produce the synchrotron emission. We can presume that most of the X-ray flares are generated by SSC radiation instead of synchrotron radiation. Therefore, the number of X-ray outbursts is less than the NIR ones which can be seen in observations.

Furthermore, radio/sub-mm emission is also variable and its variability occurs later compared to NIR/X-ray variations. To be more precise, the time delay between the sub-mm and NIR flares is about 2 hours. This delay can be described by a model in which the emitting region expands and cools down adiabatically and consequently becomes transparent later at longer wavelengths (Yusef-Zadeh *et al.*, 2006b; Eckart *et al.*, 2008b).

In the NIR, two different scenarios have been proposed to statistically study the flaring activity of Sgr A*. The first one describes the bright flares as obvious flares on top of a quiescent state emission (Genzel *et al.*, 2003, 2010; Dodds-Eden *et al.*, 2011), while the other shows that they are the most luminous outbursts from a single state emission that contains the whole flux density values of Sgr A* (Witzel *et al.*, 2012). In some of the bright

flares, quasi-periodic substructures with about 20 minutes period have been detected and can be modelled as orbiting hot spots close to the last stable orbit of the BH (Genzel *et al.*, 2003; Meyer *et al.*, 2006a; Zamaninasab *et al.*, 2010). With the future NIR interferometer GRAVITY (Eisenhauer *et al.*, 2008), we will be able to measure the exact position of Sgr A* and detect the hot spot motion on its orbit (Zamaninasab *et al.*, 2010). In the case of dealing with a large data set, the quasi periodic oscillation (QPO) is not significant in comparison with a red noise model with a slope break around 100 minutes (Do *et al.*, 2009; Meyer *et al.*, 2009; Witzel *et al.*, 2012). I will discuss more about the NIR flares of Sgr A* in the next chapter.

In addition to the variable emission of Sgr A*, it is believed that it has been much more luminous some hundred years ago (Sunyaev *et al.*, 1993; Koyama *et al.*, 1996; Revnivtsev *et al.*, 2004; Terrier *et al.*, 2010; Capelli *et al.*, 2012). The scattered X-ray emission from the molecular cloud Sgr B2 is an evidence of Sgr A* past activity.

Recently, between 2013 to 2014, there was an increased flare luminosity of Sgr A* in the X-ray domain monitored by *XMM-Newton* and *Chandra* campaigns (Ponti *et al.*, 2015). In particular, an X-ray flare emission 100 times more luminous than the quiescent emission of Sgr A* was detected in April 2013 by *Swift* at the position of this source (Degenaar *et al.*, 2013). This high activity was, at the beginning, presumed to be the result of the interaction of a dusty object close to Sgr A* (DSO/G2) (see next Section) and the SMBH. However, *NuSTAR* showed that there was a magnetar activity very close to the position of Sgr A*, which produced the immense X-ray emission (Mori *et al.*, 2013; Kennea *et al.*, 2013). The magnetar faded away after 1.5 years from its discovery and made it possible for the observers to detect X-ray flare activities from Sgr A* with X-ray telescopes again (Haggard *et al.*, 2015). Starting in late summer 2014, there was an increase in the flaring rate of Sgr A*. Since the event is about six months after the peri-center passage of DSO/G2, it might be an indication of high accretion activity due to the DSO/G2 passage close to the black hole. On the other hand, the observed flare variation can be a random event, coming from the non-uniform time distribution of flares produced by a noise process, and was detected because of the increased monitoring frequency (Ponti *et al.*, 2015).

1.5 The Dusty S-cluster Object (DSO/G2) at the GC

Recently a fast moving infrared excess source called DSO/G2 was reported to be a gas cloud by its elongated Br γ line emission along a highly eccentric orbit approaching Sgr A* (Gillissen *et al.*, 2012). However, based on continuum imaging data from Very Large Telescope (VLT) and Keck telescopes, Eckart *et al.* (2014) obtained K_s -band identification and proper motion of the G2 or Dusty S-cluster Object (DSO), proposing that it is a dust-enshrouded star. In Valencia-S. *et al.* (2015) NIR (1.45-2.45 μm) observations of the DSO

during its approach to the black hole at the center of the Galaxy were reported. The observations were carried out with SINFONI at the VLT. They could detect spatially compact Bry line emission from DSO before and after its peri-bothron passage which was in agreement with the detection reported by [Witzel *et al.* \(2014\)](#) from L -band observations. These observational evidences suggest that the DSO is possibly associated with a young accreting stellar object on an elliptical orbit around Sgr A*. The observational data were also used to derive the orbit of this object and predict its periastron transition. Based on its orbital parameters, if the DSO is a dust-embedded star, its outer shell may very well be subject to tidal disruption ([Eckart *et al.*, 2013](#); [Witzel *et al.*, 2014](#); [Zajačec *et al.*, 2014](#)). Sgr A* and the DSO encounter likely leads to an increase of Sgr A* flare activity across the electromagnetic spectrum. Since the DSO discovery, many observation programs have intended to study the radiation from Sgr A* as the DSO feeds the accretion stream, to constrain the emission processes of the flares, and to study the properties of the DSO. In addition to the continuum and line emission studies of the DSO, polarimetry imaging of this source can help to further constrain its properties. This source, its characteristics, and the polarization study of it will be discussed in details in chapter 4.

1.6 Polarization at the GC

The polarization map of the central stellar cluster of the GC including Sgr A* has been obtained through high resolution observations in K_s - and L' -band, implementing the new polarimetric calibration procedure ([Buchholz *et al.*, 2011, 2013](#); [Witzel *et al.*, 2011](#); [Shahzamanian *et al.*, 2015](#)). In general, the effects that are responsible for producing NIR polarization in a GC source can be considered to be intrinsic to the source itself or foreground effects caused by grain alignment along the line of sight, i.e. dichroic extinction. Dichroic extinction can also have a significant role in polarization as a local effect for sources that are surrounded by an optically thick dust envelope ([Whitney and Wolff, 2002](#)).

The GC foreground polarization is 6.1% at 20° in K_s -band and 4.5% at 20° in L' -band, widely parallel to the Galactic plane ([Buchholz *et al.*, 2011](#)). Besides foreground polarization, sources that are in the Northern Arm and the bow-shock sources have intrinsic polarization in K_s -band as well as at longer wavelengths. The intrinsic polarization is the difference in polarization degree and angle from the homogeneous foreground polarization. The intrinsic polarization of the stellar sources can be produced by the following processes: emission from aligned dust grains, dichroic extinction, and scattering on spherical grains and/or magnetically aligned dust grains. It is still an open question which of these processes is the one responsible for producing the observed intrinsic polarization of GC sources.

The polarization data in K_s - and L' -band has helped to confirm the supposed nature of several bow-shock sources like IRS 1W, 5, 5NE, 10W, and 21. For instance, IRS 21 has

a K_s -band polarization of about 10-16% at 16° (Eckart *et al.*, 1995; Ott *et al.*, 1999) and it is suggested to be a bow shock created from a mass-losing Wolf-Rayet star (Tanner *et al.*, 2002). However, recently Yusef-Zadeh *et al.* (2015) proposed that IRS 21 is a stellar cluster including six radio sources.

In the case of Sgr A*, the observed time variable polarization is a clear indication for intrinsic emission mechanisms at work (such as synchrotron emission), which generates strongly polarized radiation.

I present the NIR polarimetry of Sgr A* and the DSO in this thesis. As a result, the discussion of NIR polarization will be deferred to the consecutive chapters. In the following, I will give a summary on the polarization of Sgr A* in particular at longer wavelengths.

Sgr A* does not show any linear polarization with upper limits of 0.1% - 2% between 1.4 and 112 GHz (Bower *et al.*, 2001). Faraday depolarization, in this case, should not play a role in depolarizing the emission, since it is generally generated in an ionized medium where the electromagnetic waves with positive and negative helicity have different refraction indices. Therefore, the source itself is not intrinsically linearly polarized at these frequencies. On the other hand, at higher frequencies, between 150 and 400 GHz, the degree of polarization for Sgr A* is 10% (Bower *et al.*, 2003). The difference of the polarization degree between high and low frequencies supports the idea, discussed before, that the mm/sub-mm to NIR emission arises from a compact emitting source orbiting very close to the SMBH, while the cm emission originates from a halo surrounding it (Meyer, 2008). Marrone *et al.* (2006, 2007) studied Sgr A* polarization at 230 and 345 GHz by using the polarimeter of the Submillimeter Array (SMA). They showed for the first time that the polarization changes over hour timescales, similar to the observed variability for the total intensity. They also detected for the first time the rotation measure, which is the position angle change of a linearly polarized light because of the Faraday rotation, with statistical significance through their observations. Considering the value of the rotation measure, the accretion rate is in the range of $2 \times 10^{-9} M_\odot \text{ yr}^{-1}$ to $2 \times 10^{-7} M_\odot \text{ yr}^{-1}$, if the magnetic field is ordered and close to equipartition. The estimated mean polarization angle is $167^\circ \pm 7^\circ$ that varies about 31° .

1.7 Outline of the dissertation

In this dissertation, I will present results from NIR polarimetry observations obtained from the VLT UT4. The information about NIR K_s observations, the data reduction process and the techniques used in this work are introduced in Chapter 2. The thesis consists of two main parts:

- Sgr A*: I will present the analysis of the most complete NIR $2.2 \mu m$ light curves of Sgr A* in polarimetry mode from 2004 to 2012 in Chapter 3. I will describe the polarized observations, data reduction and the photometry that lead to light curves. I explain the statistical analysis of the polarized emission from this source, along with a study of the statistical behavior of polarization degree and angle. I then discuss the implications of the results obtained for the polarization measurements.
- The Dusty S-cluster Object (DSO/G2) at the Galactic Center: In Chapter 4, I describe the analysis of the polarimetry of the DSO based on NIR K_s -band data. This chapter contains a description of the data reduction, obtained light curve, and polarimetry measurements of the DSO. I discuss the possible nature and properties of this source.

Chapter 5 contains a brief summary of results, conclusions and outlook. And at the end, the Appendix provides supplementary information.

OBSERVATION AND DATA REDUCTION

2.1 Observations



Figure 2.1: The four telescopes of the VLT in paranal, Chile. Image credit: ESO.

All the observations presented in this work are carried out by the Very Large Telescope (VLT) operated by European Southern Observatory (ESO) at Paranal, Chile. Sgr A* is a very faint source in the NIR and located in a very dense region, therefore high angular resolution is required. Furthermore, ground-based telescopes located at dry, high altitude sites are needed for observing in the NIR or IR in general, since there is less water vapor to absorb IR emission. Therefore, considering such limits, VLT, Keck and Subaru telescopes are ideally suitable for NIR observations of Sgr A*. The VLT includes four 8.2 meter telescopes (see Fig. 2.1). These telescopes can work together and combine the light and work as an interferometer (VLTI). For the purposes of this work one single telescope has been used.

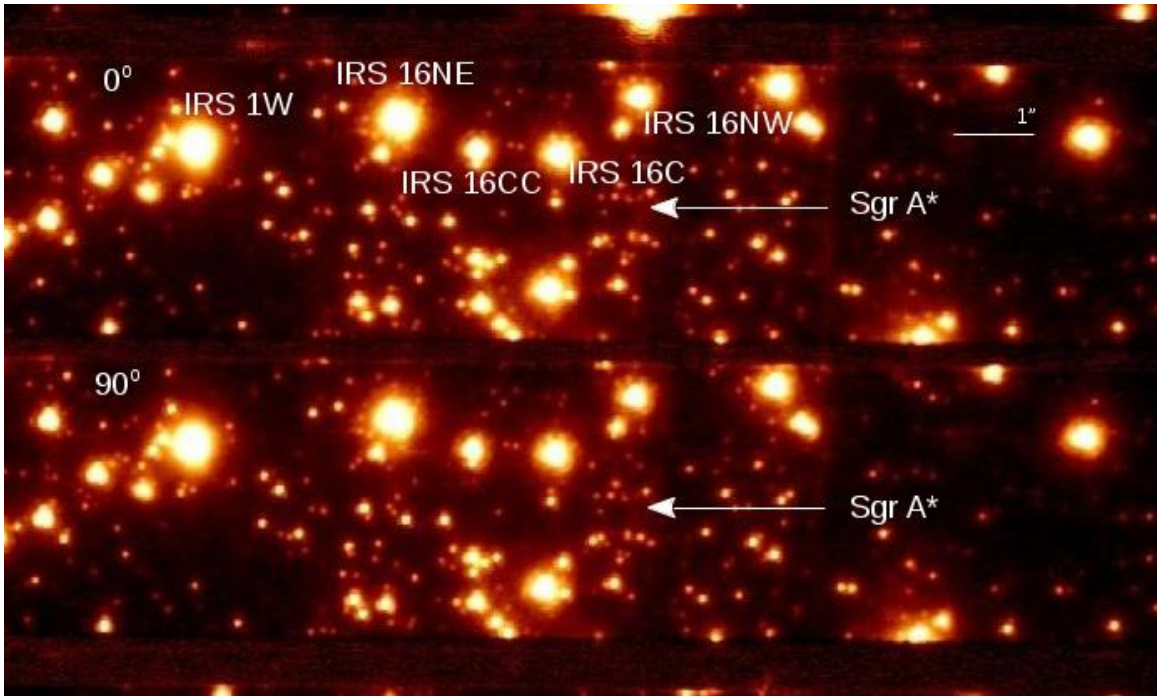


Figure 2.2: The arrangement of the Wollaston prism images on the NACO detector. The two central strips show the images in orthogonally polarized light. Another exposure with the retarder rotated by 45° provides a complementary pair of orthogonal measurements from which the full linear polarization information can be derived.

NACO instrument is installed at the Nasmyth focus of the Unit telescope 4, Yepun¹. NACO is a combination of the AO system NAOS (Nasmyth adaptive optics system) and the science camera CONICA (Coude near infrared camera). CONICA is equipped with a Wollaston prism that splits the light into two orthogonal linearly polarized beams. Simultaneous measurement of two orthogonal directions of electric field vector is possible through this prism. The Wollaston prism is coupled with a half-wave retarder plate that can turn fast, and therefore, makes it possible to change to different angles. This equipment is highly required for the polarization measurements of a source that varies fast with time (see Fig. 2.2).

¹In the time of doing the observations presented in this dissertation NACO was installed at UT4, while now it is operating at UT1.

2.2 Adaptive Optics

The image quality of the optical-infrared telescopes is degraded by instrumental effects of the telescope itself and the turbulence in the atmosphere. The angular resolution of the telescope in ideal conditions is:

$$\theta = 1.22 \frac{\lambda}{D} \quad (2.1)$$

where λ is the observing wavelength and D is the telescope diameter. Due to the diffraction of light on the telescope aperture, the image of a point source is an Airy function:

$$I(\theta) = I_0 \left(\frac{2J_1(\pi D \sin \theta / \lambda)}{\pi D \sin \theta / \lambda} \right)^2 \quad (2.2)$$

where I_0 is the maximum intensity of the diffraction pattern and J_1 is the order one Bessel function of the first kind. For getting higher quality images, different mechanical improvements have been used in the telescope structure. Degradation of the image in the telescope can be caused by the telescope structure deviation produced by heat, wind force, and gravity. Active Optics system can correct these small changing errors by monitoring the image of a star during the observations. The position of the telescope primary mirror is adjusted by the analysis of the image at low temporal frequency about 0.05 Hz. However, correcting the transient atmosphere turbulence is done by another system which is faster and called Adaptive Optics (AO).

The light coming through the AO is split by a dichroic mirror and travels to a wavefront sensor (WFS). The WFS measures the wavefront distortions and transfers the information to a deformable mirror and tip-tilt assembly. Real time corrections of the deformable mirror restore the wavefront flatness. The AO corrected image will be diffraction-limited. However, the resolution is affected by the atmospheric turbulence and cannot be better than ~ 0.7 arcsec in the NIR. For understanding the mechanism of atmosphere's turbulences, there is a simple model that considers the seeing cells with a diameter of r_0 , the Fried diameter (Fried, 1996), deforming flat wavefronts of an observational object. Moving of these cells leads the point spread function (PSF)² to be variable during the time. Also the finite size of the cells makes the PSF to be spatial variable. In reality, several layers of turbulence distort the incoming light and not just a single layer, but this simple model can help us to understand the AO imaging.

The simplest AO set up is tip-tilt correction, which corrects the image motion by using a fast moving tip-tilt mirror. In a more advanced AO system, multiple mirror segments can tip and tilt independently and work as the deformable mirror. These segments correct the phase errors of a few micrometers for the incoming wavefront. The corrections have to be done on time scales of a few 10 to 100 Hz. Fried (1996) showed that the angular diameter

²The point spread function is the response function of a telescope to a point source.

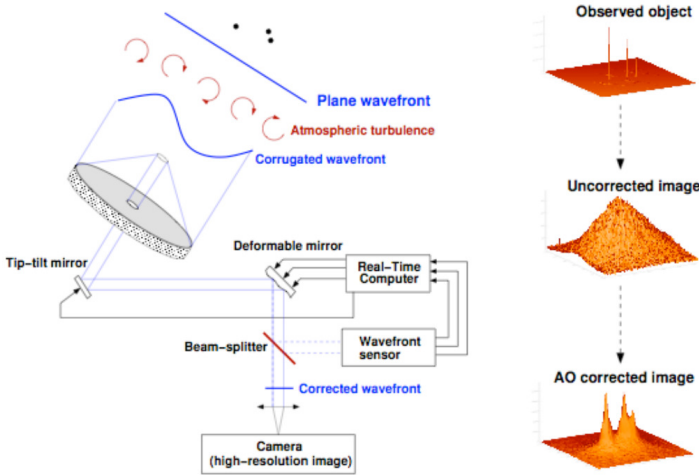


Figure 2.3: Schematic view of the Adaptive Optics system. Image credit: ESO NACO user manual.

of a seeing cloud ($\omega \approx \frac{\lambda}{r_0}$) has the below relation with the observed wavelength λ :

$$\omega \sim \lambda^{-1/5}. \quad (2.3)$$

As a result, in the NIR the angular diameter of a blurring cloud is less than the same in the optical and therefore the seeing in the NIR is better than the visible light. Current AO systems correct images at wavelengths longer than one micrometer since for shorter wavelengths, higher computational power is needed. Fig. 2.3 shows a schematic view of an AO loop. The WFS needs a bright and close star for guiding which is in the isoplanatic patch³. The isoplanatic patch angle in the NIR is in the order of $20''$ while in the optical is about $5''$. For GC observations, the bright supergiant IRS 7 which is located about $5.5''$ north of Sgr A* is a good candidate for guiding the AO loop in the IR. Since finding the proper guidance source is difficult, there is an alternative way for guiding called the laser guide star (LGS) technique. In this technique a bright point source which is an artificial guide star is created by a Sodium-laser that excites the Sodium atoms in the mesosphere at 90 km altitude.

The corrected PSF contains a diffraction-limited core and an extensive seeing wing. If the observing conditions are good and the guidance star is close and bright enough, the resulted PSF will be very close to the diffraction limit. In this situation, the Strehl ratio in

³The isoplanatic patch is the region on the sky where the seeing cells distribution over the aperture does not change drastically.

the K_s -band will be more than 30%. The Strehl ratio is a quality measurement of the PSF correction and is defined as the ratio between the intensity peaks of the corrected and the theoretical PSFs. In the case of bad conditions or at shorter wavelengths, the Strehl ratio is only a few percent.

2.3 Standard data reduction process

The NACO instrument produces 1024 by 1024 pixel images that can be affected by several problems caused by the detector itself and the wavelength regime (NIR). Therefore, in addition to the astronomical object observations, the thermal radiation of the telescope and the atmosphere, the dark current, the read-out noise, and the non-linear response function of the detector are monitored. In reality, the detector has inhomogeneities caused by the ageing or production procedure. Therefore, different regions of the detector can record a given photon flux as different number of counts. The detector's response function can be obtained if it is illuminated by the twilight sky (sky flat-field) or a lamp (lamp flat-field). In a lamp flat-field method several images are taken with a switched on/off lamp. These on and off images are subtracted and averaged. The observed image will be divided by these flat-fields to get the same detector response for the entire image. Here, the noise term is neglected.

Another step is to consider the thermal radiation of the atmosphere while dealing with the images. We should observe the sky without any apparent sources in it and not very far from the main object to subtract it from the observed image. In the Galactic Center, the region which has no sources is located 713'' west and 400'' north of IRS 7. The sky observations should be repeated several times, since the thermal emission changes with time. The number of sky exposures depends on the observing wavelength. In the K_s -band, small number of sky measurements are required considering the observation conditions. While, for the L' -band, the effect of the atmospheric emission is stronger and even small variations are important to be considered. Therefore, after each image taken of the object, one sky exposure is captured.

The following step is the correction for dead/hot pixels. These pixels either have a zero response function (dead) or a very high value compared to the pixels around them (hot). They should be detected and their values be replaced by the average value of the pixels around them.

After doing the above standard data reduction steps, the resulting image still suffers from degradation. In the next section, I will discuss these degradation factors.

2.4 Deconvolution

An image observed with a telescope is influenced by several degradation factors. One of them is the turbulence in the atmosphere which can be corrected by AO system. The image of a point source is a PSF. In an ideal case of having an aberration-free telescope without any atmospheric effect, the PSF would be an Airy pattern due to the diffraction of light on the telescope aperture. The PSF varies with time because of the atmospheric turbulence and the time variations of the instrument, also it is variable over the FOV.

The observed image $I(x, y)$ can be described by the convolution of the real object $O(x, y)$ with a $PSF(x, y)$, and additional function describing the detector read-out noise, anisoplanasy and other non-linear terms, $c(x, y)$:

$$I(x, y) = PSF(x, y) \odot O(x, y) + c(x, y) \quad (2.4)$$

where \odot is the convolution operator, which is the multiplication in Fourier space. If there is not any noise, the Fourier transform of the real object can be obtained by a division in Fourier space.

$$\hat{O}(u, v) = \frac{\hat{I}(u, v)}{P\hat{S}F(u, v)} \quad (2.5)$$

$\hat{O}(u, v)$, $\hat{I}(u, v)$, $P\hat{S}F(u, v)$ are the Fourier transforms of $O(x, y)$, $I(x, y)$, $PSF(x, y)$, with u and v as the spatial frequencies corresponding to the coordinates x and y . The process of determining the original object by knowing the observed image and the PSF is deconvolution.

However, there are some limitations such as the noise term $c(x, y)$ that cannot be neglected in real observations and the PSF determination that cannot be done with perfect accuracy. Therefore, different methods have been created to attain the object distribution. [Ott et al. \(1999\)](#) have shown in particular for the Galactic Center that deconvolution algorithms like Lucy, Clean and Wiener filtering work very well and reproduce the flux densities down to the detection limit. [Eckart et al. \(2005\)](#) studied the comparison of different deconvolution methods. In this dissertation, the Lucy-Richardson deconvolution method is used which is the most suitable one for the purposes of this work and I describe it here briefly (see below).

2.4.1 PSF estimation

It is necessary to estimate the PSF before doing the deconvolution process. PSF can be determined in the Galactic Center by extracting from individual point sources in the observed image with the software package StarFinder ([Diolaiti et al., 2000](#)). StarFinder is an IDL program to obtain high precision photometry and astrometry of point sources in crowded fields images.

StarFinder estimates an initial PSF by getting the median of several isolated and bright sources in the stellar field selected by the user. The PSF determination continues by spotting the stars in the field and considering them while repeating the PSF extraction. Through this procedure the contaminating sources near the position of the selected PSF stars would be subtracted resulting in an improvement of the final PSF quality.

2.4.2 Lucy-Richardson deconvolution

Using the Lucy-Richardson (LR) algorithm (Lucy, 1974; Richardson, 1972) allows us to separate the flux density contributions of very close sources. It is an iterative process based on the correction of observed probability distributions. The method includes the iteration of several steps as described in the following. Firstly, the current estimate of the object distribution $O_n(x, y)$ is convolved with the $PSF(x, y)$:

$$I_n(x, y) = O_n(x, y) \odot PSF(x, y) \quad (2.6)$$

Then the image obtained, $I_n(x, y)$, is compared with the observed image $I(x, y)$:

$$Q(x, y) = \frac{I(x, y)}{I_n(x, y)} \odot PSF(x, y) \quad (2.7)$$

The PSF acts as a low-pass filter that reduces the effect of high spatial frequencies on the result since these frequencies are strongly affected by noise. Lastly, multiplying the original object estimate with $Q(x, y)$ leads to a new estimate of the object distribution:

$$O_{n+1}(x, y) = O_n(x, y) \odot Q(x, y) \quad (2.8)$$

Because of the convolution with the PSF high spatial frequencies are suppressed, and therefore the noise amplification are avoided. Subsequently, details of the image related to high spatial frequencies can only be resolved after an adequate number of iterations. This is one of the disadvantages of this method that the computation requires high amount of time especially for a large number of images to be processed. One should be careful when choosing the number of iterations, since running a high number of iterations can end in resolving a diffuse background into point sources. Another disadvantage is that the emission of very faint sources and diffuse background close to bright sources can be added to the flux density of the bright star. This effect can be seen as dark areas around the bright sources that can be minimized by an accurate PSF estimation. Figure 2.4 shows the deconvolved images of the central region of the Galaxy while at the position of Sgr A* a clear flaring activity is noticeable.

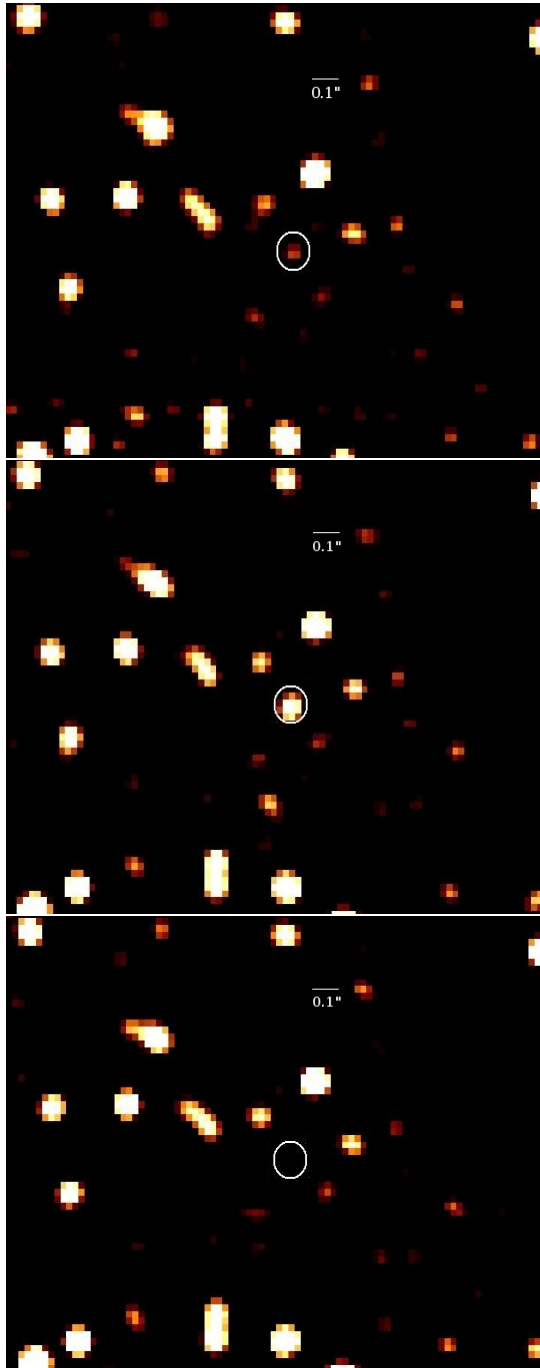


Figure 2.4: Central few arcseconds region of GC in K_s -band in 2012. From top to bottom: the time from the start of the observation is 0, 25 and 50 minutes. The position of Sgr A* is shown with a circle and it is in the flaring state. After the standard data reduction process, the images are deconvolved with LR algorithm.

K_s -BAND NEAR INFRARED POLARIMETRY OF SGR A*

3.1 Introduction

Sagittarius A* (Sgr A*) is a compact radio source located at the center of our galaxy (Eckart and Genzel, 1996, 1997; Eckart *et al.*, 2002; Schödel *et al.*, 2002; Eisenhauer *et al.*, 2003; Ghez *et al.*, 1998, 2000, 2005b, 2008; Gillessen *et al.*, 2009a). It is associated with a super-massive black hole with the mass of about $4 \times 10^6 M_\odot$ and is the best example of a low-luminosity galactic nucleus accessible for observations. Sgr A* is time variable in high spatial resolution observations in the near-infrared (NIR) and X-ray domain compared to a lower degree of variability in the radio to sub-mm regime. The NIR counterpart to Sgr A* shows short bursts of increased radiation that last about 100 minutes and can occur four to six times per day.

The nature of emission processes detected from Sgr A* can be revealed by analyzing the polarization of the electromagnetic radiation. Therefore, this source has been observed in the polarimetric imaging mode with NACO using its Wollaston prism since 2004 (Eckart *et al.*, 2006d; Meyer *et al.*, 2006b,a; Eckart *et al.*, 2008a; Zamaninasab *et al.*, 2010; Witzel *et al.*, 2012). Different research groups have conducted multi-wavelength observations to study the variable emission process from the radio to X-ray range and spectral energy distribution (SED) of Sgr A* (Baganoff *et al.*, 2001; Porquet *et al.*, 2003; Genzel *et al.*, 2003; Eckart *et al.*, 2004, 2006d,b,a, 2008a,b,c; Meyer *et al.*, 2006b,a, 2007; Yusef-Zadeh *et al.*, 2006b,a, 2007, 2008; Dodds-Eden *et al.*, 2009; Sabha *et al.*, 2010; Eckart *et al.*, 2012a). Hubble Space Telescope (HST) observations at $1.6 \mu m$ and $1.7 \mu m$ wavelengths (Yusef-Zadeh

et al., 2009) indicate that the activity of Sgr A* is, more than 40% of the time, above the noise level. The highly polarized NIR flux density excursions usually have X-ray counterparts, which suggests that the responsible radiation mechanism is inverse Compton emission or synchrotron-self-Compton (SSC) (Eckart *et al.*, 2004, 2006d,a; Yuan *et al.*, 2004; Liu *et al.*, 2006; Eckart *et al.*, 2012a). Several studies successfully model the observations by assuming the variability to be connected to the emission from single or multiple spots close to the last stable orbit of the black hole (Meyer *et al.*, 2006b,a, 2007; Zamaninasab *et al.*, 2008).

Zamaninasab *et al.* (2010) find a correlation between the modulations of the observed flux density light curves and changes in the polarization degree and position angle. They work with a model in which matter orbits the super-massive black hole with relativistic speed. This information can help us to constrain the spin of the black hole (assuming that the Kerr metric describes the gravitational field). However, it is still impossible to conclude based on the available data whether timescales is comparable to the orbital period near the inner edge of the accretion flow (especially, near the radius of the innermost stable orbit) play a role in the variability. The intrinsic emissivity of accretion disks and the effect of a magnetic field are energy dependent, although the geometrical effects of strong gravitational fields act on photons independently of their energy. Thus, the variation of the polarization angle and the polarization degree are expected to be energy dependent. The dependencies can be degenerate and together with the interdependencies of the observables require both time-resolved observations (e.g. Zamaninasab *et al.*, 2010) and a statistical analysis as we present here.

The time variable NIR emission from Sgr A* can be interpreted as a result of a single continuous power-law process with a break timescale between 500 and 700 minutes (Witzel *et al.*, 2012). This process presents prominent flux density excursions lasting for about 100 minutes. The excursions are called flares that occur as flaring activity. Eckart *et al.* (2012a) modelled the flaring activity based on multi-wavelength observations in 2009, as a signal from a synchrotron/synchrotron-self-Compton component.

The statistical properties of flaring activity of Sgr A* have been analyzed by several authors instead of focusing on investigating the individual flares. Do *et al.* (2009) do not identify quasi-periodic oscillations (QPOs) during studying 7 total flux density NIR light curves taken with Keck telescope. The QPOs can be linked to the orbital time of the matter in the inside part of an accretion disk, in contrast to the pure red noise. They also show that Sgr A* is continuously variable. Fluctuations in the accretion disk can explain the power-law distribution of the NIR variable emission (Chan *et al.*, 2009). However, the spectral energy distribution, the correlation between flux density variations and changes in the polarization degree, and the delayed sub-mm emission present that the emission originates from a compact flaring domain with a schwarzschild radius size. This compact region can

be an emitting hot spot(s) falling into the black hole (see e.g. Genzel *et al.*, 2003; Dovčiak *et al.*, 2004, 2008; Eckart *et al.*, 2006b; Gillessen *et al.*, 2006; Meyer *et al.*, 2006b; Hamaus *et al.*, 2009; Zamaninasab *et al.*, 2010) or a jet with blobs of ejected material (Markoff *et al.*, 2001). Doi (1978) and Pineault (1980) are among the first publications introducing the orbiting hot spots concept in relation to black hole accretion disks constructively. X-ray emission bursts of Cyg X-1 were described via this concept (Doi, 1978). It was also applied to analyze variability in total flux density and polarization properties of the super-massive black hole in AO 0235+164.

The NIR K_s -band total flux density variability of Sgr A* observed with VLT from 2004 to 2009 has been studied by Dodds-Eden *et al.* (2011). The authors explain the time variability of Sgr A* as a two state process, a quiescent state with a log-normal distribution for low flux density values (below 5 mJy) and a flaring state with a power-law distribution for high flux density values (above 5 mJy). The physical processes responsible for low and high fluxes from Sgr A* are claimed to be different based on their analysis. However, their conclusion for the low flux densities is biased by source crowding and the measurement uncertainties since it is based on data close to the detection limit. On the other hand, Witzel *et al.* (2012) describe the Sgr A* variability by a single power-law distribution for a larger data set between 2003 and early 2010. They interpret that there is not a second intrinsic state based on the flux density distribution (see Fig. 3.14). Modeling the data by a rigorous two state regime switching time series that additionally considered the timing properties information of Sgr A*, Meyer *et al.* (2014a) conclude the same result. These results truly present that the variability process can be explained as a single state, continuous red-noise process with a characteristic timescale of several hours, without any distinctive flux density in the range of reliably measurable flux densities. Another important aspect of the time variability is the analysis of the intrinsic polarization degree and polarization angle of the Sgr A* emission and their variations during the flaring event.

In this chapter I analyze the most comprehensive sample of NIR polarimetric light curves of Sgr A*. In Section 3.2 I provide details about the observations and data reduction. In Section 3.3, I present the statistical analysis of polarized flux densities, a comparison with total flux densities, and their distribution as provided by Witzel *et al.* (2012). In Section 3.4 I summarize the results and discuss their implications.

3.2 Observations and data reduction

All observations in this chapter have been carried out with the adaptive optics (AO) module NAOS and NIR camera CONICA (together NACO; Lenzen *et al.*, 2003; Rousset *et al.*, 2003; Brandner *et al.*, 2002) at the UT4 (Yepun) at the Very Large Telescope (VLT) of the European Southern Observatory (ESO) on Paranal, Chile. All K_s -band (2.2 μm) observational data of the central cluster of the Galactic Center (GC) with the camera S13 in 13 mas

pixel scale polarimetry from mid-2004 to mid-2012 that have flaring activity have been collected. The AO loop was locked in all the selected observations using the infrared wave-front sensor of NAOS on the NIR supergiant IRS7 with $K_s \sim 6.5 - 7.0$ mag, located $\sim 5.5''$ north from Sgr A*. NACO has a Wollaston prism and a half-wave retarder plate that allows us to measure simultaneously the two orthogonal directions of the electric field vector and a rapid change between different angles of the electric field vector.

I describe a short summary of the reduction steps in the following. I used the reduced data sets as presented in [Witzel *et al.* \(2012\)](#) for 2004 to 2009. An observational strategy and data reduction steps similar to [Witzel *et al.* \(2012\)](#) were applied on the 27 May 2011 and 17 May 2012 data sets which have not been published before. For the 27 May 2011 and 17 May 2012 nights, Sgr A* and a sufficient number of flux secondary density calibrators were in the central arcsecond. The AO correction of these nights was mostly stable and in good seeing conditions during the observing time. [Table 3.1](#) presents the observing dates, integration times, sampling rate, and mean flux densities of the data sets used for the analysis in this chapter.

Table 3.1: Observations Log. Credit: *Shahzamanian et al. (2015)*, reproduced with permission ©ESO.

Date	Start (UT time)	Stop (UT time)	Length (min)	Number of frames	Maximum flux density density (mJy)	Average sampling rate (min)	Integration time (sec)
2004-June-13	07:54:22.95	09:15:08.79	80.76	70	3.17	1.17	20
2005-July-30	02:07:36.13	06:21:40.41	254.07	187	8.94	1.36	30
2006-June-01	06:39:49.16	10:44:27.63	378.41	244	14.5	1.55	30
2007-May-15	05:29:55.42	08:31:48.45	181.88	116	16.7	1.58	40
2007-May-17	04:24:14.84	09:34:40.15	292.42	192	9.78	1.53	40
2008-May-25	06:05:20.32	10:35:38.65	270.31	250	10.25	1.085	40
2008-May-27	04:52:04.92	08:29:38.07	217.55	184	4.32	1.18	40
2008-May-30	08:24:33.51	09:45:25.69	80.87	40	12.39	1.023	40
2008-June-01	06:04:51.56	10:10:26.78	245.59	240	7.08	1.027	40
2008-June-03	08:37:23.56	09:58:58.85	81.59	80	10.02	1.032	40
2009-May-18	04:37:55.08	10:19:54.10	341.98	286	12.53	1.19	40
2011-May-27	04:49:39.82	10:27:25.65	337.77	334	7.55	1.2	45
2012-May-17	04:49:20.72	09:52:57.08	303.62	256	6.64	1.2	45

Table 3.2: The calibrators and their corresponding flux densities. Credit: [Witzel et al. \(2012\)](#).

Star	m_{K_s}	flux density [mJy]
S26	14.94	6.97
S27	15.41	4.41
S6	15.35	4.66
S7	14.92	6.92
S8	14.21	13.31
S35	13.20	33.74
S10	13.95	16.91
S65	13.58	23.78
S30	14.12	14.46
S98	15.27	5.01
S100	15.29	4.92
S84	14.66	8.79
S107	14.82	7.59

I implemented standard reduction steps to all the exposures (see Sect. 2.3). Lamp flat-fields have been used instead of sky flat-fields to avoid polarimetric effects produced by the sky. The four polarization channels (0° , 45° , 90° , 135°) of the individual data set were aligned since the exposures were dithered by using a cross-correlation method with sub-pixel accuracy (ESO Eclipse Jitter; [Devillard, 1999](#)). Using the isolated stars close to Sgr A*, the point spread functions (PSFs) were extracted from the images with the IDL-based StarFinder routine ([Diolaiti et al., 2000](#)).

The PSF fitting algorithm of StarFinder finds point sources in the image and measures the source flux densities and their positions by fitting a model PSF to all point sources, considering offsets as a result of background emission and gradients therein. I benefited from the LR algorithm to deconvolve the images (see Sect. 2.4.2 for details), instead of using the resulted values of StarFinder photometry. For large data sets without a consistent condition the PSF fitting statistics of StarFinder is questionable to be used. The off-apertures to measure the background are applied to monitor the effect of weak residuals emerging from a combination of a faint background mostly dominated by the superposition of extended seeing foots and the positivity constraint for the LR algorithm (see the following). The image restoration was done by convolving the deconvolved images with a Gaussian beam of a FWHM of about 60 mas, which corresponds to the diffraction limit at $2.2\mu m$.

3.2.1 Flux density calibration

The flux densities of Sgr A* and other compact sources in the image are obtained by aperture photometry using circular apertures of 40 mas radius. The flux density was calibrated through the known K_s -band flux densities of 13 S-cluster stars ([Schödel et al., 2010](#)). 6

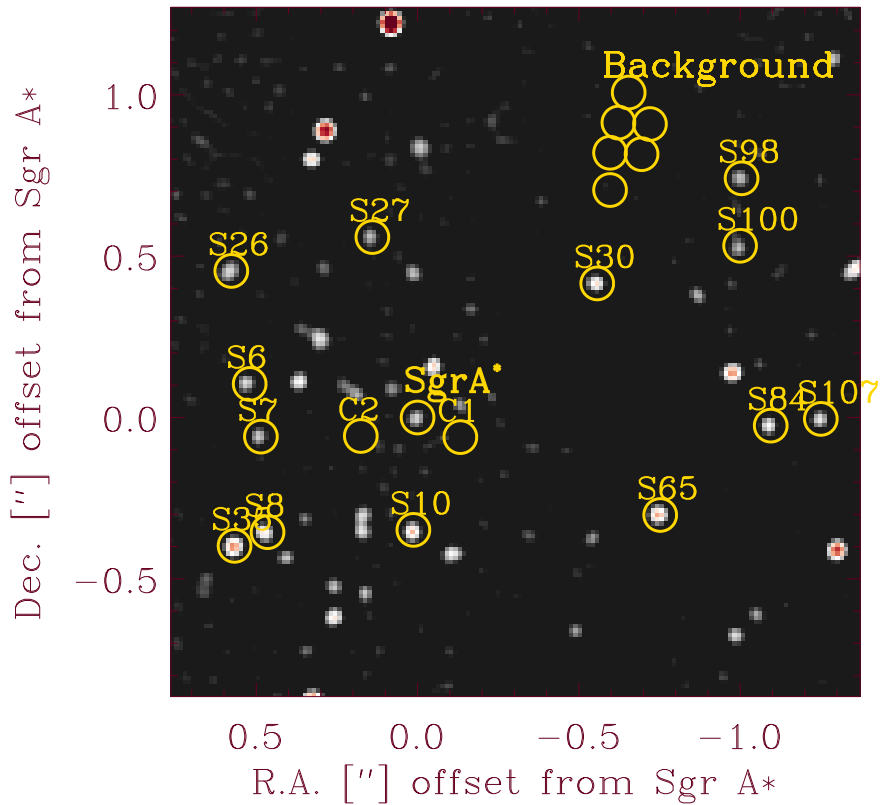


Figure 3.1: The image obtained by K_s-band deconvolved image of the Galactic Center on 17 May 2012. The image displays the positions of Sgr A*, calibration stars, and comparison apertures for background estimates marked by yellow circles. Credit: [Shahzamanian et al. \(2015\)](#), reproduced with permission ©ESO.

comparison stars and 8 background apertures, located at positions where no individual sources can be detected, are also considered. See Fig. 3.1 and Table 3.2 for more details on the apertures positions and the list of calibrators. I summed the photon counts in each aperture and then added the resulted values of two orthogonal polarimetry channels to obtain the total flux densities. The obtained values were cleaned up from the background contribution. I measured the flux densities of the calibrators close to Sgr A* and also at the position of Sgr A*, subsequently, corrected them for extinction adopting $A_{K_S} = 2.46$, derived for the innermost arcsecond by Schödel *et al.* (2010). I implement aperture photometry on all frames and obtain the light curves of Sgr A* for 27 May 2011 and 17 May 2012 data, as shown in Fig. 3.2.

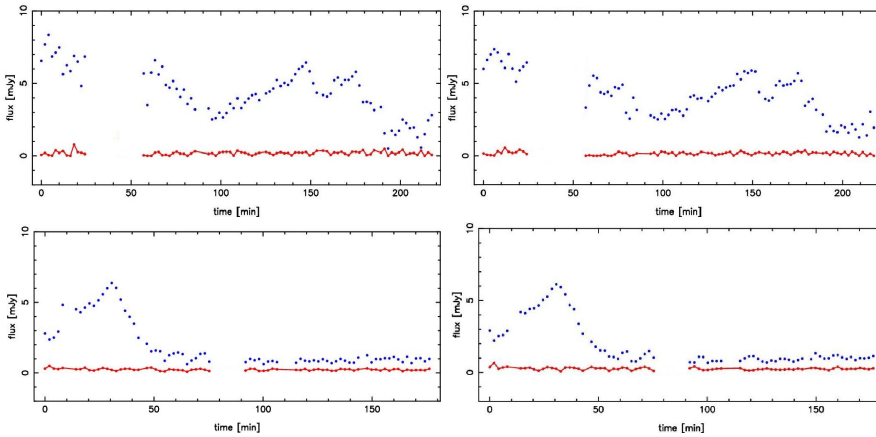


Figure 3.2: NIR K_S -band ($2.2 \mu\text{m}$) light curves of Sgr A* obtained by polarimetry mode on 27 May 2011 (top) and 17 May 2012 (bottom) generated by adding pairs of orthogonal polarization channels; left: $0^\circ, 90^\circ$ and right: $45^\circ, 135^\circ$. The blue dots represent Sgr A* flux density measured in mJy, and the red connected dots display the background flux densities. Credit: Shahzamanian *et al.* (2015), reproduced with permission ©ESO.

The gaps presented in the light curves are the result of sky measurements or AO re-configuration. For 27 May 2012 data, Sgr A* flux density changed between 5 and 10 mJy during the whole observing run. For 17 May 2012 data, the flux density of Sgr A* increased to about 7 mJy during the first 50 minutes of the observation and then decreased again.

A K_S -band deconvolved image of the Galactic Center on 17 May 2012 is presented in Fig. 3.1. The image is captured with the ordinary beam of the Wollaston prism. The positions of calibration stars, comparison apertures for background estimates, and Sgr A* are shown. See also Fig. 1 from 30 September 2004 by Witzel *et al.* (2012) for comparison. Source labeling is done using the nomenclature by Gillessen *et al.* (2009a).

I calculated the flux density of Sgr A* from the obtained flux densities in the four dif-

ferent polarization channels and corrected for possible background contributions. The measured flux density distributions of several calibration stars close to Sgr A* fitted by Gaussian functions are shown in the top plot of Fig. 3.3. The observational uncertainties produce the scatter of the flux densities around the mean value and can be obtained from the fits.

The bottom plot of Fig. 3.3 presents the relation of the standard deviations (σ) of the Gaussians fitted to the distributions and the mean flux density. A second degree polynomial is the best function that describes the dependency of σ values with the flux densities up to 33 mJy.

Using a second degree polynomial enables us to estimate the quality of the data and compares it to the previous studies (Witzel *et al.*, 2012; Do *et al.*, 2009) who applied a similar method, though it is a prior unphysical. I have added to the plot the measured flux densities and scatter of the two background apertures (C1 and C2 in Fig. 3.1) and included them in the fit. The uncertainties are ~ 0.25 mJy up to 10 mJy total flux density and are mostly produced by a combination of imperfectly subtracted PSF seeing halos of surrounding, brighter stars, a change in the AO performance, and differential tilt jitter. For understanding the instrumental effect on flux density statistics, statistics of these effects is important to be considered. The halo noise effect (Fritz *et al.*, 2010) is studied by analyzing the control apertures (C-apertures) close to the Sgr A* position. Their average flux density is not equal to zero, and their obtained flux density values are comparable to the total flux density distribution of the stars with flux values less than 10 mJy. The obtained relation agrees well with that found by Witzel *et al.* (2012) using a larger sample of total flux density measurements presented in their Fig. 7, within the uncertainties and for a total flux density value below 10 mJy. Polarization data tends to be observationally biased towards higher Strehl values compared to AO imaging in standard observer mode, i.e. without selecting preferred atmospheric conditions. Therefore, our data follows 20% to 25% narrower flux density distributions at higher flux densities around 30 mJy. Fig. 3.3 shows that statements on the source intrinsic total or polarized flux density of Sgr A* can only be convincing if the total flux density is significantly larger than the limit of ~ 0.25 mJy.

3.2.2 Polarimetry

I can derive the polarization degree and angle from the obtained normalized stokes parameters using non-normalized analog-to-digital converter (ADC) values from the detector (see details in Witzel *et al.* 2011),

$$F = f_0 + f_{90} = f_{45} + f_{135} \quad (3.1)$$

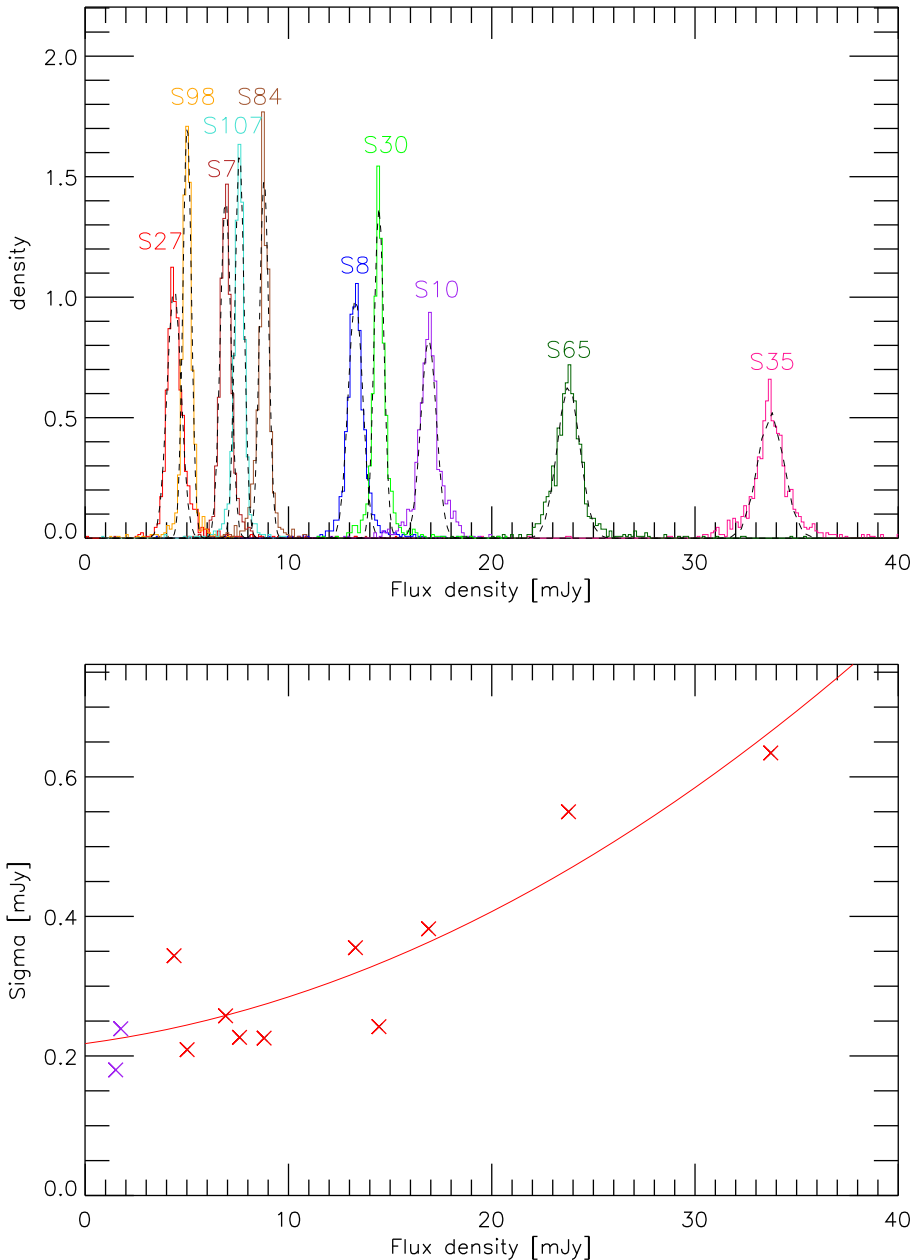


Figure 3.3: Top: Normalized flux density distributions of 10 flux calibrators of Sgr A*. The Gaussian fits to the distributions are presented in dashed lines. Bottom: flux densities' standard deviation of calibration stars as a function of their flux densities. The polynomial fit, shown in the red line, to the estimated σ values of the calibrators presented in the upper panel (red crosses). The measured error values (reported by [Witzel et al. 2012](#)) at the position of the comparison apertures for the background emission close to Sgr A* are presented by purple x symbols (see [Fig.3.1](#)). Credit: [Shahzamanian et al. \(2015\)](#), reproduced with permission ©ESO.

$$Q = \frac{f_0 - f_{90}}{f_0 + f_{90}} \quad (3.2)$$

$$U = \frac{f_{45} - f_{135}}{f_{45} + f_{135}} \quad (3.3)$$

$$p = \sqrt{Q^2 + U^2} \quad (3.4)$$

$$\phi = \frac{1}{2} \arctan\left(\frac{U}{Q}\right), \quad (3.5)$$

where f_0 , f_{45} , f_{90} , and f_{135} are the flux densities of four polarimetric channels with f_0 , f_{90} and f_{45} , f_{135} being pairs of orthogonally polarized channels. The total flux density is represented by the variable F and Q and U are the normalized Stokes parameters. The circular polarization in normalized Stokes V is assigned to zero since the information on circular polarization is not available with NACO (see [Witzel et al., 2011](#)) for a detailed discussion). The polarization degree is presented by the quantity p and the polarization angle is shown by ϕ which is measured from the north to the east and samples a range between 0° and 180° . The polarized flux is computed as the product of polarization degree and the total flux density. Uncertainties for F , Q , U and the obtained p and ϕ were calculated from the flux density uncertainties. A careful calibration is needed since NACO is a Nasmyth focus camera-system and instrumental effects can affect the results. [Witzel et al. \(2011\)](#) applied the Stokes/Mueller formalism to derive the instrumental polarization. Their analytical model uses Mueller matrices to the obtained normalized Stokes parameters to get the intrinsic normalized Stokes parameters. I applied their model to decrease the systematical uncertainties of polarization angles and degrees created by instrumental polarization to about $\sim 1\%$ and $\sim 5^\circ$, respectively. For the stars in the innermost arcsecond to Sgr A*, foreground polarization has been obtained (see e.g. [Buchholz et al., 2013](#)), however, its value for the exact line of sight towards Sgr A* itself is unknown. It is not possible to certainly disentangle line of sight effects from the foreground polarization produced by the stars close to Sgr A* with the current instrumentation.

Confusion with stellar sources can occur in estimating the flux density of Sgr A*, since the Galactic center region is very crowded ([Sabha et al., 2012](#)). This confusion needs to be removed in order to be able to compare the polarized flux densities of different years without offsets. Therefore, the minimum flux density of four polarization channels is subtracted from the flux densities of the corresponding channels for each data set and then the polarization degrees and polarized flux densities of our data sample are estimated. Here the polarized flux density contributions of confusing stars are assumed to be on the

same level as the foreground polarization. Thus, it is conservative to subtract the minimum of all four polarization channels in each epoch. Moreover, to compare the polarized flux density distribution with the total flux density distribution in Witzel *et al.* (2011) subtracting the faint stellar contribution was needed. The mentioned change in the flux densities did not prominently change the polarization degree value.

3.3 Data analysis

I present in Fig. 3.4 the light curves that represent all NIR K_s -band flaring activities observed by NACO in polarization mode. Strong flare events usually last for about 100 minutes. When bright flare activities occur, the variations in total flux density, polarization degree, and polarization angle are more prominent. It is interesting to investigate if there are preferred values or ranges of values for the polarization degree and angle that are independent of the flare flux density, although the flare events are different in terms of the maximum flux density. I determine the flux density uncertainties for our statistical analysis through the relation presented in Fig. 3.3. I apply the results of our analysis presented in the following for obtaining the uncertainties of the polarization degree and angle.

3.3.1 Statistical behavior of polarization measurements

We wanted to know the expected statistical behavior of polarization measurements to adequately present and interpret the data. Several authors have studied the polarization statistics, e.g. Serkowski (1958, 1962); Vinokur (1965); Simmons and Stewart (1985); Naghizadeh-Khouei and Clarke (1993); Clarke (2010). The polarization degree p is a positive quantity from Eq. 3.4 that takes values between zero and one (or equivalently 0% – 100%). The value of p is biased by the uncertainties in Q and U , which in our case are the result of observational noise in the polarization channels. This result is an overestimation of p at low signal-to-noise ratio (S/N) measurements. Polarimetric observations need a higher S/N compared to photometric measurements. The S/N of the total intensity is related to the first order of the polarized intensity like $(S/N)_{polarized\ intensity} \approx p \times (S/N)_{total\ intensity}$, where the polarization degree is mostly smaller than one. Therefore, in case of having high $(S/N)_{total\ intensity}$ weak polarization signal can be detected (Trippe, 2014).

In the presence of random noise except for large S/N , the polarization degree distribution does not follow a Gaussian distribution. I estimated that total flux density measurements of stars around Sgr A* are, in very good approximation, Gaussian distributed (see Sect. 3.2.1). As a result, the noise in the polarization channels must have the same distribution. U and Q follow Cauchy distributions that, at medium S/N , can be estimated by normal distributions around the intrinsic values U_0 and Q_0 . Considering that U and Q are independent variables with associated variances of σ_0^2 , the polarization-degree distri-

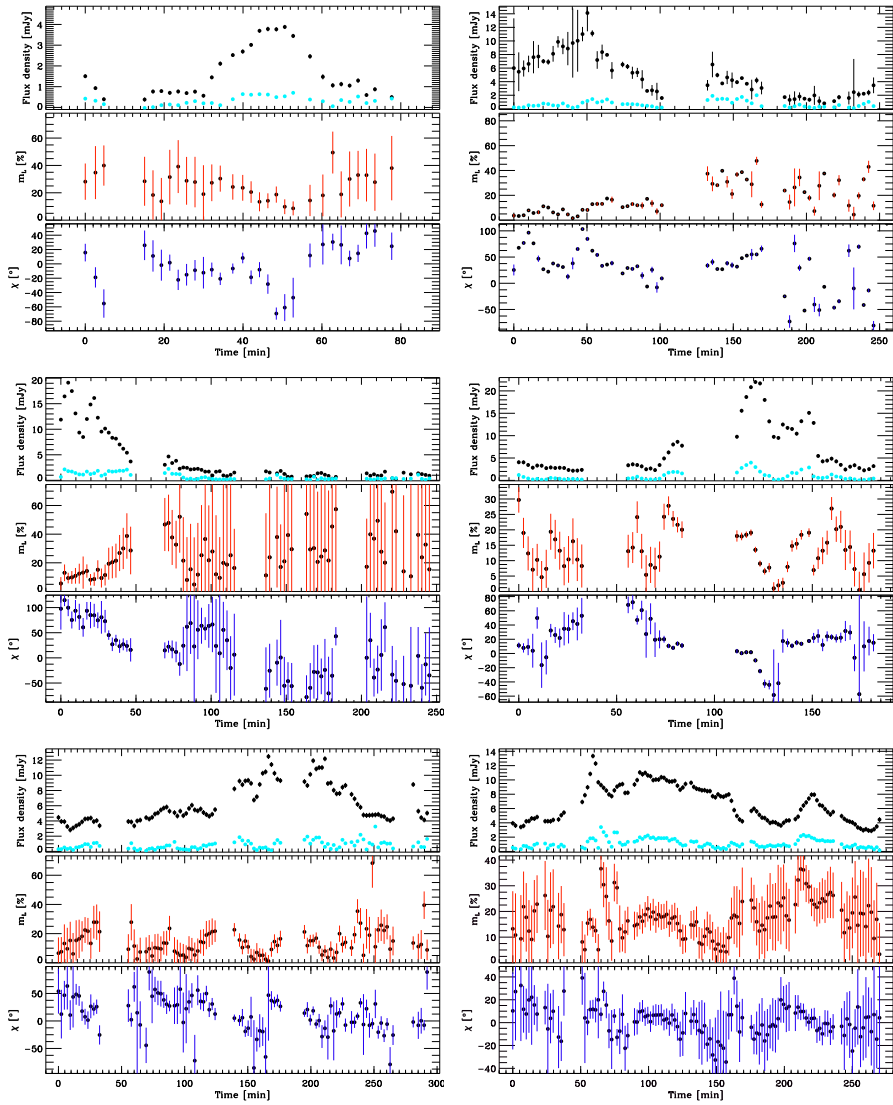


Figure 3.4: Flares observed in NIR K_s -band polarimetry mode of Sgr A*. The date of these observations are 2004 June 13, 2005 July 30, 2006 June 1, 2007 May 15, 2007 May 17, 2008 May 25, 2008 May 27, 2008 May 30, 2008 June 1, 2008 June 3, 2009 May 18, 2011 May 27, 2012 May 17 (the order of the images starts from top left to bottom right). In each panel: Top: total flux density is shown in black, and polarized flux density is presented in cyan. Middle: The degree of linear polarization is shown in red; Bottom: The polarization angle is presented here as blue. Credit: [Shahzamanian et al. \(2015\)](#), reproduced with permission ©ESO.

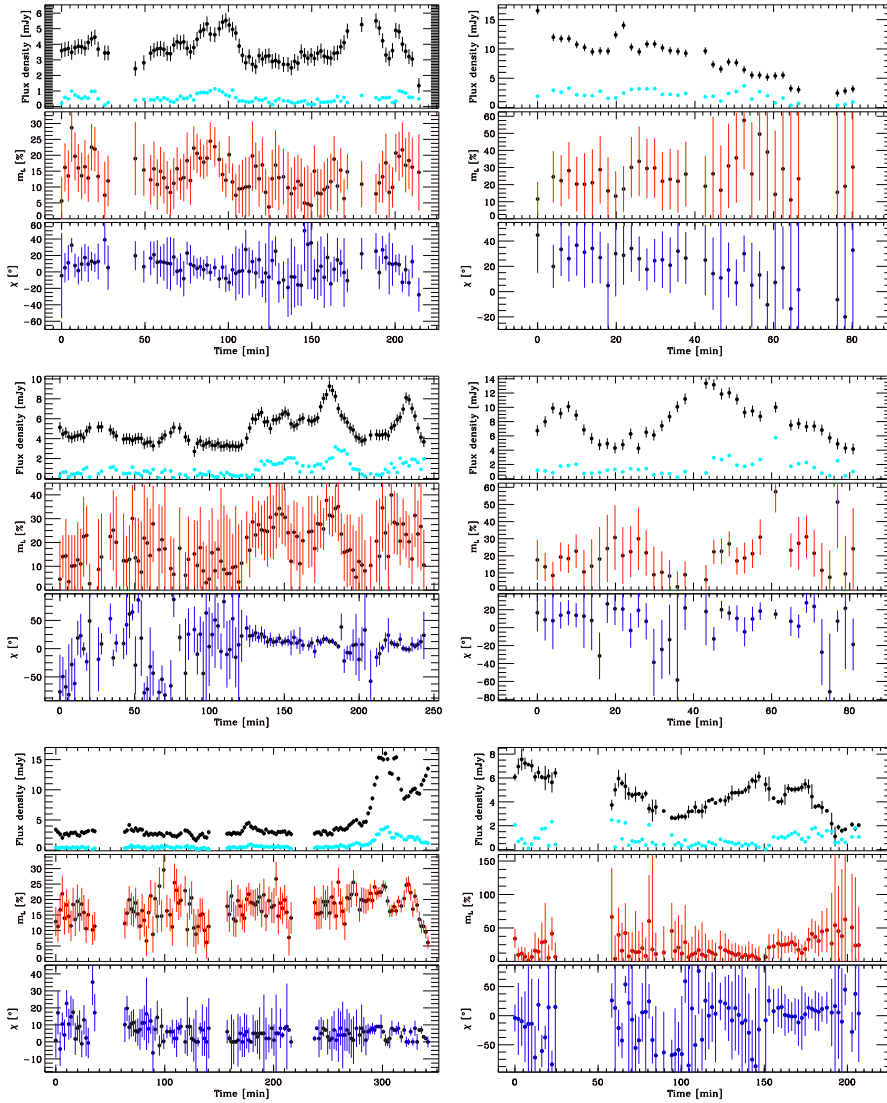


Figure 3.4: Continued.

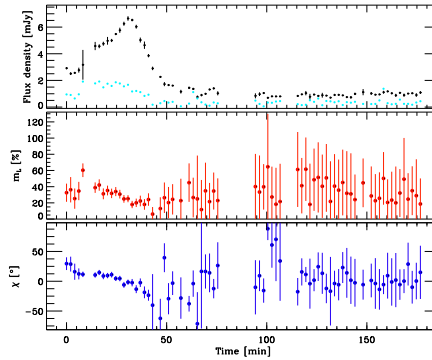


Figure 3.4: *Continued.*

bution $F(p; p_0, \sigma_0)$ for a specific value of the intrinsic polarization degree $p_0 = (U_0^2 + Q_0^2)^{1/2}$ can be defined by a Rice distribution,

$$F(p; p_0, \sigma_0) = \frac{p}{\sigma_0^2} J_0 \left(i \frac{p p_0}{\sigma_0^2} \right) \exp \left(-\frac{p^2 + p_0^2}{2\sigma_0^2} \right), \quad (3.6)$$

where $J_0(ix)$ is the zero-order Bessel function of the imaginary argument (Serkowski, 1958; Vinokur, 1965). The bias on the observed value of p for different $(S/N)_{\text{polarization degree}}$ defined as $P_0 = p_0/\sigma_0$ is analyzed in Simmons and Stewart (1985) (see their Fig. 1). The peak of the $F(p; p_0, \sigma_0)$ distribution is the most probable observed value which is always larger than p_0 for low S/N , and approaches the intrinsic value p_0 with increasing S/N . At low S/N , the polarization angle follows a multi-modal distribution with a spread covering the whole range of possible values of ϕ . At medium S/N and under the same previous assumptions, for a particular intrinsic polarization angle ϕ_0 the probability distribution $F(\phi; \phi_0, P_0)$ is symmetric around its most probable value, and depends on the $(S/N)_{\text{polarization degree}}$. It can be shown as

$$F(\phi; \phi_0, P_0) = \left\{ \frac{1}{\pi} + \frac{\eta_0}{\sqrt{\pi}} e^{\eta_0^2} [1 + \text{erf}(\eta_0)] \right\} \exp \left(-\frac{P_0^2}{2} \right), \quad (3.7)$$

with $\eta_0 = (P_0/\sqrt{2}) \cos(\phi - \phi_0)$, and “erf” the Gaussian error function (Vinokur, 1965; Naghizadeh-Khousi and Clarke, 1993). For high S/N , the distribution tends toward a Gaussian distribution with standard deviation $\sigma_\phi = 28.65^\circ (\sigma_p/p) = \sigma_p/(2p)$ (radians),

where the polarization degree dispersion is $\sigma_p = \sigma_0$ (Serkowski, 1958, 1962). Several methods to remove the bias in the observed p measurements for a source with a constant polarization state have been proposed (Simmons and Stewart, 1985; Stewart, 1991). However, whether this condition is fulfilled in the case of Sgr A* is not known. Moreover, the variability of its intrinsic polarization degree and angle is predicted with some scenarios. Thus, without any priori assumption on the polarization properties of Sgr A*, it is needed to follow the propagation of the uncertainties from the observables estimated quantities i.e. flux densities in the polarization channels, to the obtained polarization properties p and ϕ . We performed Monte Carlo simulations of the observational noise and the measured quantities, and applied them to statistically estimate the obtained polarization degree and angle distributions and their uncertainties. The primary parameters of the simulation are the total flux density F_0 and its uncertainty σ_F , and the intrinsic polarization degree p_0 and angle ϕ_0 . We calculated the corresponding polarization-channel flux densities $f_0, f_{90}, f_{45},$ and f_{135} , for each set of initial parameters from Eqs. (1)-(5). The relation between the total flux densities and their uncertainties presented in Sect. 3.2.1 is considered to associate an uncertainty with the total flux density measured in each polarization channel f_X . Under the assumption that the distributions of F are in a very good approximation Gaussian, and that the noise in each part of orthogonal polarization channels is about the same, we express the standard deviation of the Gaussian function that defines the distribution of each f_X as $\sigma_{f_X} = \sigma_F / \sqrt{2}$, i.e. $\sigma_{f_0} = \sigma_{f_{90}} = \sigma_{f_{45}} = \sigma_{f_{135}} = \sigma_F / \sqrt{2}$. We draw from the f_X distributions, 10^4 retrads of polarization-channel fluxes and apply them to measure $U, Q, p,$ and ϕ , as it is done with real data. It is possible to establish the most probable observed values of p and ϕ from the simulations, as well as the ranges in which certain percentages of the values are included. Intrinsic total flux densities are considered in the range from 0.8 mJy , which is the photometry detection limit (Witzel *et al.*, 2012), to 15.0 mJy , which is approximately the maximum value in our data set. The initial values for the polarization degree (the amplitude of the intrinsic polarization, p_0) are fixed to a range from 5% to 70%, while ϕ_0 is set to a preferred polarization angle of 13° , based on the following data analysis.

The resulting distributions of $U, Q, p,$ and ϕ for two different initial total flux density values, one with medium S/N and the other with high S/N , are shown in Figs. 3.5 and 3.6 as an example. The distributions in the plots correlate to the values that would be measured for a source whose intrinsic total flux density, polarization degree, and polarization angle are the initial values given at beginning of the simulation. The limits of the intervals containing 68%, 95% and 99% of all values are used as our effective $1\sigma, 2\sigma$ and 3σ error intervals. Asymmetric errors for p in the form $p_{-\sigma p}^{+\sigma p^2}$ are given. It is clear from these two examples that the most probable value of p is larger than its true value p_0 , but for higher S/N it becomes closer to p_0 .

Furthermore, a Rice function is fitted to the p distribution and the σ value of Rice distribution is obtained. The simulated polarization degree values for different initial flux

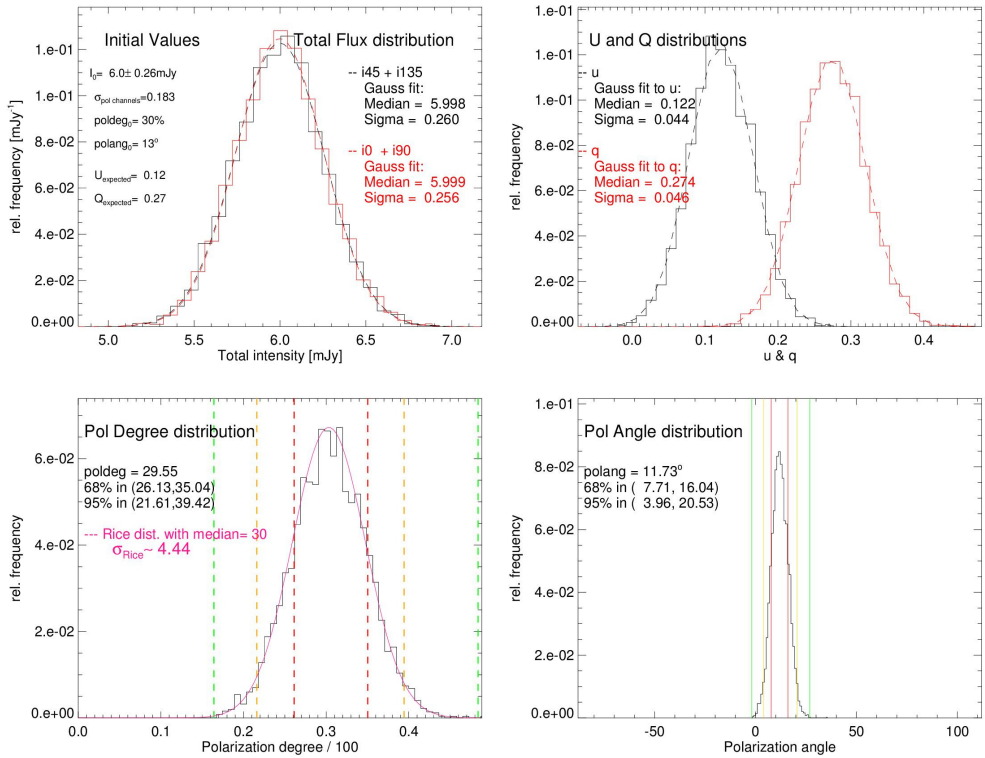


Figure 3.5: The polarization degree and angle generated by simulation for the high flux densities. Initial values for simulation: total flux density= 6 mJy, polarization degree= 30% and polarization angle= 13° . Credit: *Shahzamanian et al. (2015)*, reproduced with permission ©ESO.

density and polarization degree values are presented in Table 3.3. We have analyzed the confidence intervals and obtained σ values for polarization angle only if the (S/N) is larger than 4.5, since for the lower (S/N), the ϕ distribution has a non-Gaussian shape. The simulated polarization angle values for different initial flux density and polarization degree values are shown in Table 3.4.

The relation between the simulated values of the total flux density and the polarization degree are shown in Fig. 3.7. The contours presented in the figure are related to 1σ , 2σ and 3σ values that enclose 68%, 95%, and 99% of points in the distribution, i.e. if these quantities are measured more than 1000 times then, the central contour would contain the 68% of measured values that are closest to the intrinsic value.

For interpretation in the upcoming section, the following results of the expected sta-

Table 3.3: Recovered polarization degrees obtained from simulation for the combination of different sets of intrinsic total flux density F' and polarization degree p' as initial values. In cases which both the upper and lower uncertainty are less than or equal to half of the actual value are shown in the boldface. Credit: [Shahzamanian et al. \(2015\)](#), reproduced with permission ©ESO.

p' [%]	F' [mJy]								
	0.8	1	1.3	1.5	2	3	4	6	10
5	27^{+22}_{-17}	24^{+16}_{-15}	19^{+12}_{-11}	15^{+12}_{-8}	12^{+9}_{-6}	9^{+6}_{-5}	8^{+4}_{-5}	6^{+3}_{-4}	5^{+3}_{-2}
10	28^{+23}_{-18}	22^{+18}_{-13}	18^{+14}_{-10}	16^{+12}_{-9}	14^{+9}_{-8}	12^{+7}_{-6}	12^{+5}_{-5}	10^{+4}_{-3}	10^{+3}_{-3}
20	30^{+26}_{-18}	22^{+24}_{-11}	24^{+15}_{-13}	24^{+13}_{-13}	21^{+10}_{-9}	22^{+6}_{-8}	21^{+6}_{-6}	21^{+4}_{-5}	20^{+3}_{-3}
30	33^{+30}_{-19}	34^{+22}_{-18}	34^{+17}_{-16}	32^{+15}_{-13}	31^{+12}_{-10}	31^{+7}_{-8}	31^{+6}_{-6}	30^{+4}_{-4}	30^{+3}_{-3}
40	40^{+33}_{-20}	40^{+26}_{-19}	42^{+18}_{-17}	44^{+14}_{-16}	41^{+12}_{-11}	41^{+7}_{-8}	40^{+6}_{-6}	40^{+4}_{-4}	41^{+3}_{-3}
50	56^{+32}_{-25}	49^{+29}_{-29}	49^{+21}_{-16}	52^{+21}_{-16}	50^{+13}_{-15}	49^{+10}_{-9}	51^{+9}_{-6}	50^{+4}_{-6}	50^{+3}_{-3}
60	61^{+34}_{-28}	60^{+27}_{-22}	61^{+20}_{-16}	60^{+17}_{-15}	61^{+13}_{-12}	60^{+9}_{-7}	60^{+6}_{-6}	60^{+4}_{-4}	60^{+3}_{-3}
70	73^{+33}_{-30}	63^{+31}_{-26}	71^{+20}_{-19}	69^{+23}_{-18}	70^{+16}_{-15}	70^{+11}_{-10}	70^{+8}_{-8}	69^{+6}_{-5}	70^{+4}_{-4}

Table 3.4: Recovered polarization angles obtained from simulation for different sets of intrinsic total flux density F' and polarization degree p' as initial values. Credit: [Shahzamanian et al. \(2015\)](#), reproduced with permission ©ESO.

p' [%]	F' [mJy]								
	0.8	1	1.3	1.5	2	3	4	6	10
5	4^{+61}_{-47}	5^{+63}_{-42}	9^{+60}_{-48}	7^{+53}_{-46}	8^{+49}_{-38}	8^{+42}_{-34}	13^{+32}_{-35}	8^{+24}_{-26}	13^{+16}_{-18}
10	0^{+58}_{-38}	5^{+53}_{-40}	9^{+43}_{-39}	9^{+40}_{-36}	10^{+33}_{-30}	13^{+21}_{-24}	14^{+15}_{-19}	10^{+13}_{-12}	13^{+8}_{-9}
20	5^{+46}_{-26}	10^{+35}_{-27}	11^{+27}_{-23}	11^{+24}_{-21}	12^{+17}_{-17}	12^{+11}_{-11}	12^{+8}_{-9}	12^{+6}_{-6}	12^{+4}_{-4}
30	8^{+31}_{-22}	11^{+24}_{-20}	10^{+20}_{-15}	12^{+14}_{-16}	12^{+11}_{-11}	11^{+8}_{-6}	12^{+6}_{-6}	12^{+5}_{-3}	12^{+3}_{-3}
40	10^{+27}_{-17}	10^{+19}_{-15}	11^{+13}_{-13}	11^{+11}_{-11}	11^{+9}_{-8}	11^{+7}_{-5}	12^{+5}_{-4}	11^{+3}_{-3}	12^{+2}_{-2}
50	6^{+18}_{-9}	10^{+13}_{-10}	11^{+12}_{-10}	11^{+12}_{-9}	12^{+9}_{-7}	11^{+6}_{-5}	12^{+4}_{-4}	12^{+3}_{-3}	12^{+2}_{-2}
60	9^{+17}_{-12}	9^{+13}_{-10}	12^{+9}_{-9}	12^{+8}_{-8}	12^{+6}_{-6}	12^{+4}_{-4}	12^{+3}_{-3}	12^{+2}_{-2}	12^{+1}_{-1}
70	6^{+16}_{-8}	9^{+9}_{-8}	11^{+9}_{-8}	11^{+9}_{-7}	13^{+6}_{-7}	11^{+5}_{-4}	12^{+3}_{-3}	13^{+2}_{-2}	12^{+2}_{-2}

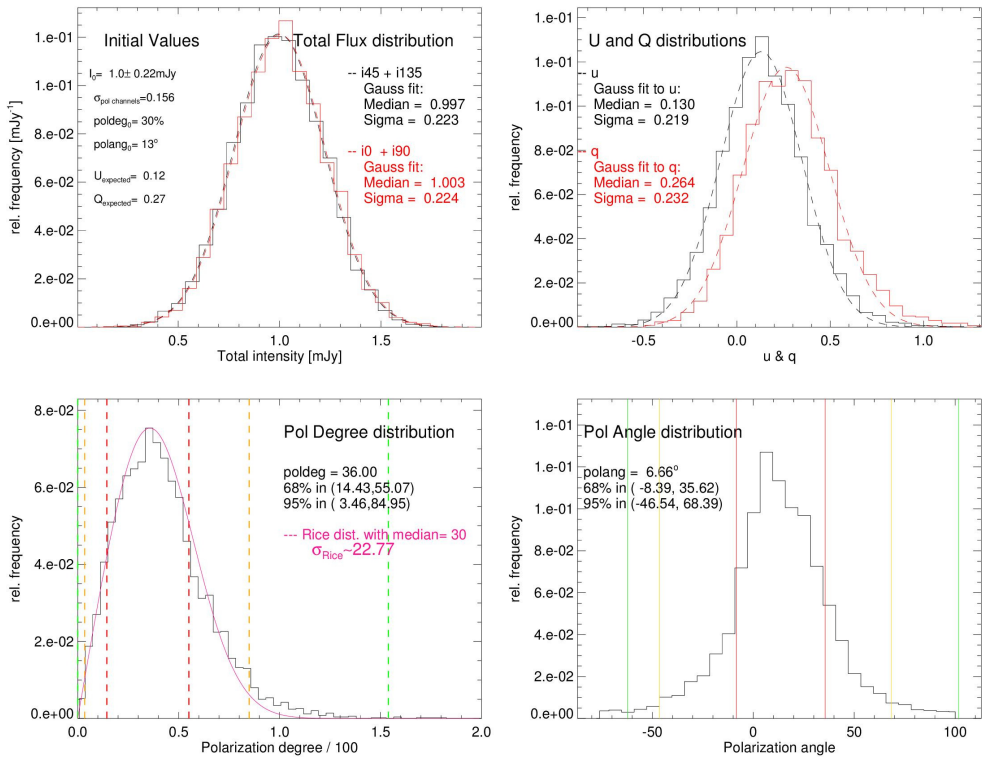


Figure 3.6: The polarization degree and angle generated by simulation for the low flux densities. Initial values for simulation: total flux density= 1 mJy, polarization degree= 30% and polarization angle= 13° . Credit: *Shahzamanian et al. (2015)*, reproduced with permission ©ESO.

tistical properties will be used:

One can notice from Fig. 3.5 and Table 3.3 that the recovered degree of polarization for our NIR data including strong flare flux densities, is Gaussian distributed around a very well central value close to the intrinsic degree with a $\sim 5\%$ uncertainty. Therefore, if the intrinsic polarization degree is centered around a fixed expectation value the statistical properties of bright flare samples will be comparable to those of the total flux density measurements as shown by *Witzel et al. (2012)*.

Figure 3.5 and Table 3.3 show that for weak intrinsic flux densities the recovered degree of polarization is not any more Gaussian distributed. The intrinsic polarization degree is specially not well recovered for moderate or weaker intrinsic values and the uncertainties are very large, such that unrealistic polarization degrees of above 100% can be measured.

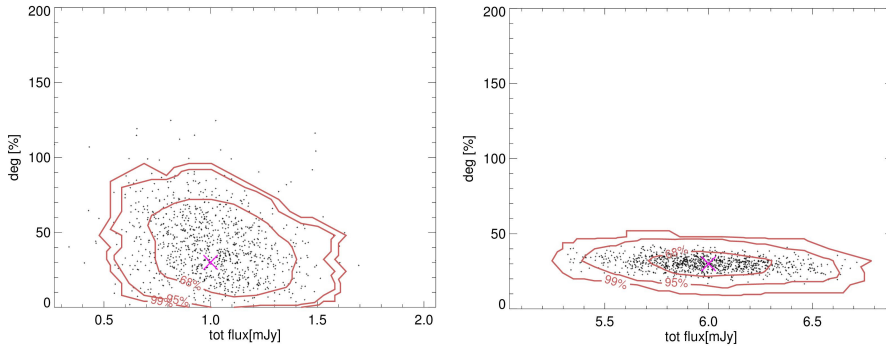


Figure 3.7: The correlation between the total flux density and polarization degree, obtained from our simulations, for initial values of: Left: total flux density = 1 mJy, polarization degree = 30%, polarization angle = 13° , Right: total flux density = 6 mJy, polarization degree = 30%, polarization angle = 13° . Credit: [Shahzamanian et al. \(2015\)](#), reproduced with permission ©ESO.

For intrinsically strongly polarized weak flares the intrinsic polarization degrees are statistically recovered, but the asymmetric uncertainties remain very large. Therefore, the total statistical behavior of observed polarization data can be considered to be consisted of the properties of subsamples of different flare flux densities and polarization degrees.

3.3.2 Polarization degree and polarization angle

Following the results of our statistical analysis presented in Section 3.3.1 I present the distribution of K_s -band polarization degrees of Sgr A* (top) and the distribution of their uncertainties (bottom) in Fig. 3.8. The only data points shown in these figures are the ones for which - based on our simulations - both the upper and lower uncertainty of the recovered polarization degree are smaller than half of the actual recovered value. In the following these values are referred as the significant measurements i.e. successful retrievals of the intrinsic polarization degree (and angle; see below).

The distribution of polarization degrees is peaked close to $\sim 20\%$. Since it is strongly affected by systematic effects with uncertainties ranging from 10% to 50% (see section 3.3.1), it does not show the shape of a Gaussian.

The polarization degree follows a Gaussian distribution if it had a single preferred value around which the realized and/or observed values then scatter. This is not the case for the data set presented here. Having a Gaussian distribution presents that all degrees up to the largest expected values for synchrotron emission are recognized by the responsible

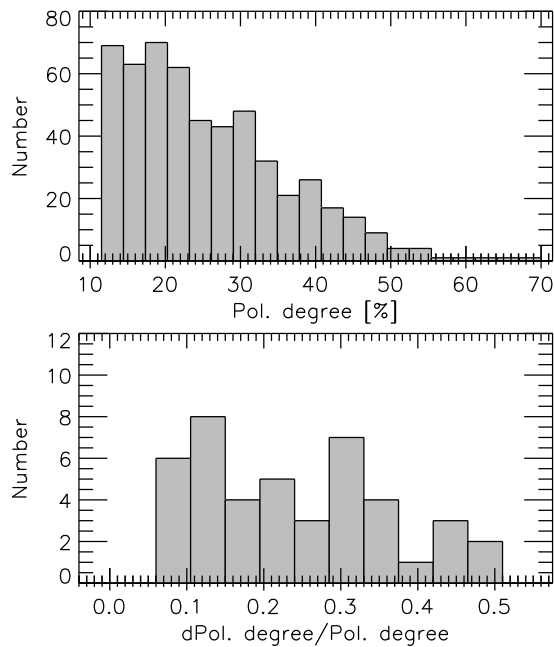


Figure 3.8: Top: K_s -band polarization degrees of Sgr A* distribution of our data set taking into account the significant data points (based on Table 3.3). Bottom: The relative uncertainties of the polarization degrees distribution. Credit: [Shahzamanian et al. \(2015\)](#), reproduced with permission ©ESO.

emission process. As discussed later the reason is an underlying well-defined range of polarization degrees and limitations in the calculating process for weak flare flux densities.

The distribution of significant K_s -band polarization angles of Sgr A* and their uncertainties is shown in Fig. 3.9 as determined for the corresponding flare flux densities following the statistical analysis shown in Section 3.3.1. The corresponding uncertainties in the recovered polarization angle for table entries with significant polarization degrees are below $\pm 20^\circ$ i.e. below about $1/3$ of a radian. The distribution of polarization angles peaks at 13° . The preferred polarization angle obtained from the distribution is $13^\circ \pm 15^\circ$ and the overall width of the distribution is on the order of 30° . Figure .1 presents the distribution of polarization angle and degree for the entire data set.

Since the uncertainty of $\Delta\phi=15^\circ$ in polarization angle is reflected in the width of the distribution of uncertainties derived from our simulations Fig. 3.8 (bottom), the data shown on the top parts of Figs. 3.8 and 3.9 are consistent. This indicates that the uncertainty in angle is dominated by the measurement error, and the physical variabilities

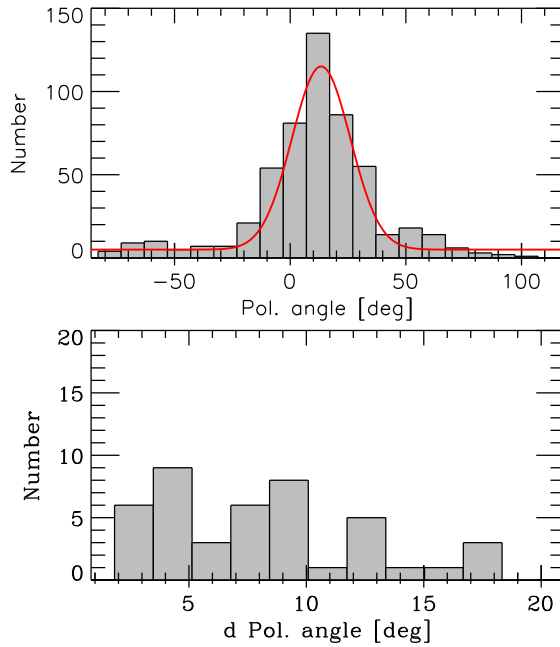


Figure 3.9: Top: The significant K_s -band polarization angles of Sgr A* distribution. The red line displays the fitted Gaussian. Bottom: Shows the absolute errors of the polarization angles distribution. Credit: [Shahzamanian et al. \(2015\)](#), reproduced with permission ©ESO.

of the angle is probably much smaller. The combined uncertainty of recording the data and retrieving the polarization information out of it is the measurement error. Figure 3.9, bottom shows that an upper limit for the uncertainties in polarization angles is $\Delta\phi=20^\circ$. This value $\Delta\phi$ indicates a corresponding expected relative uncertainty of the polarization degree of about $\frac{\Delta p}{p} \sim \tan(15^\circ)=0.36$ (i.e. 36%, see Fig. 3.10 for description). This is similar to the approximate center value of 0.3 (i.e. 30%) found for the slightly skewed distribution of relative uncertainties of the polarization degree (Fig. 3.8, bottom) for the entire set of significant data as obtained from the simulations. Since the uncertainty in angle only accounts for the lower portion of the distribution of relative uncertainties in polarization degree, this shows that intrinsic fluctuations of that quantity dominate the polarization degree. The intrinsic variability of the relative $2 \mu\text{m}$ NIR polarization degree for Sgr A* is on the order of about 30%, under the assumption that the measurement and intrinsic uncertainty add quadratically.

I showed for all data with significant polarization degrees the average elevation of Sgr A* in the sky for each polarization measurement (Fig. 3.11, top) and the average of flux densities versus the polarization angles binned in 15° intervals (Fig. 3.11, bottom),

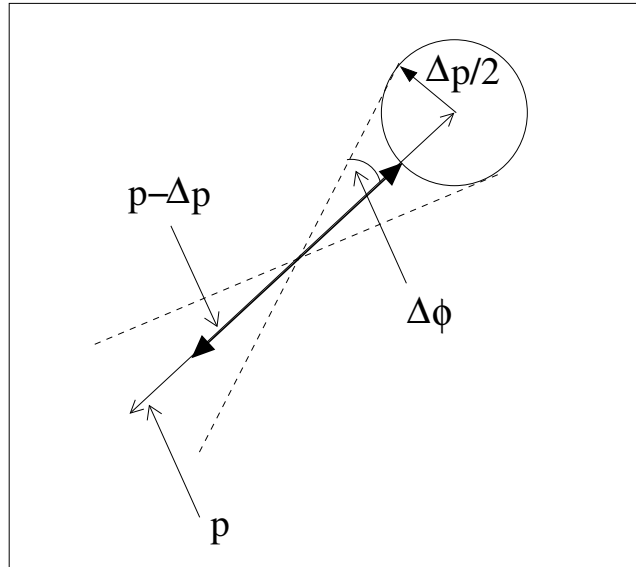


Figure 3.10: Illustration of $\Delta p \sim p \tan(\Delta\phi)$ between the mean uncertainty of the polarization angle $\Delta\phi$ and the polarization degree Δp . The sky-projected of polarization degree p and polarization angle ϕ are presented here. Credit: *Shahzamanian et al. (2015)*, reproduced with permission ©ESO.

in order to analyze if the distribution of polarization angles of Sgr A* is affected by the strength of the flare and the position of this source in the sky. Figure .2 shows the corresponding plots for all data. A significant correction due to instrumental polarization needs to be applied in the region located at about ± 0.5 hours with respect to the meridian (see Fig. 9 in *Witzel et al., 2011*). It is related to an elevation of higher than about 80° . Most of the measurements were done at elevations below 75° based on the distribution of data in Fig. 3.11 (top), thus the correction for instrumental polarization is very small. For polarization angles close to the preferred angle of 13° the corresponding mean flux density is within about 1σ from the mean flux density values of all 15° intervals (see the distribution of data in Fig. 3.11 (bottom)). Therefore, the flux density values that are related to polarization angles around the preferred value are not exceptionally high or low. In summary, it can be excluded that the preferred polarization angle of about 13° is related to flux density excursions of particular brightness or to a particular location in the sky and instrumental orientation. Hence, I come to conclusion that the preferred polarization angle is a source intrinsic property.

The variable polarization of Sgr A* is source intrinsic, except for measuring effect. The stable foreground polarization in the central arcsecond is only on the order of 5% at 27 de-

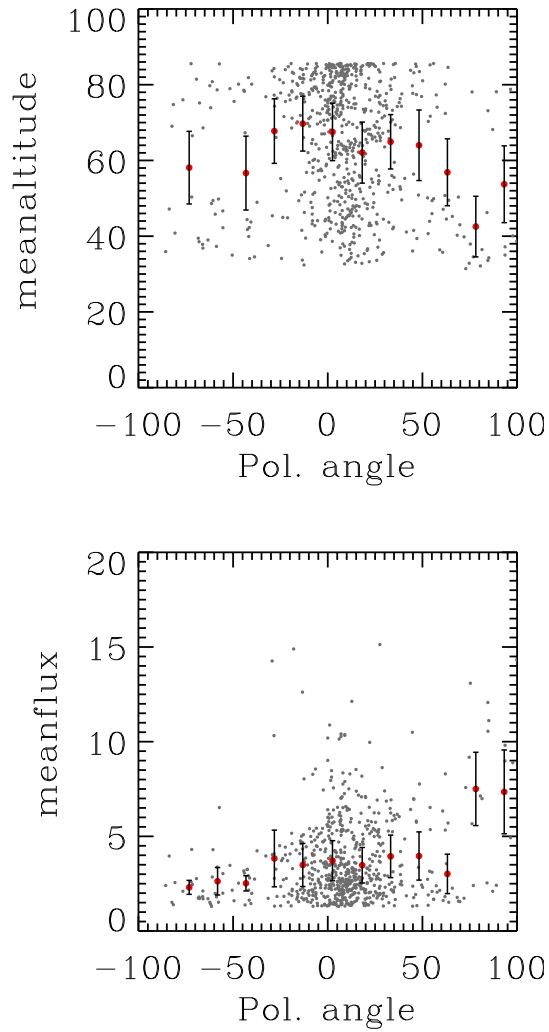


Figure 3.11: Top: The relation between elevation of Sgr A* and polarization angle; Bottom: The relation between total flux density and polarization angle; The bin width in polarization angle is 15° . The black dots show the values for individual measurements. The mean values per bin are shown as red dots with error bars. Credit: *Shahzamanian et al. (2015)*, reproduced with permission ©ESO.

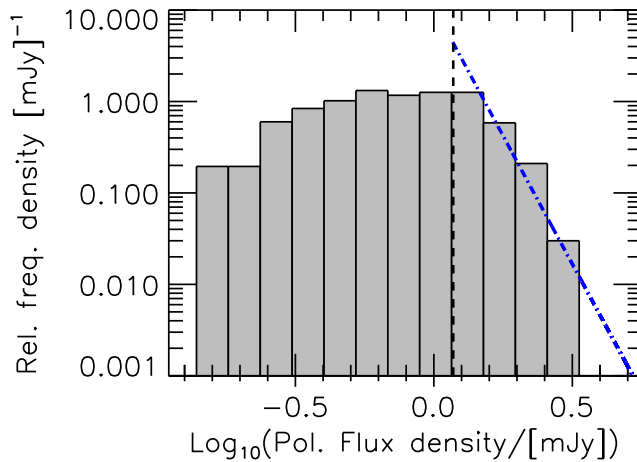


Figure 3.12: The polarized flux density's histogram for all significant data. Note that the logarithmic scale is used. The thick black dashed line displays the position in which the power-law starts to fit to the histogram. Credit: *Shahzamanian et al. (2015)*, reproduced with permission ©ESO.

grees (*Witzel et al., 2011*) which agrees well with the value obtained for the over all central stellar cluster of 4% at 25 degrees (*Knacke and Capps, 1977*). With the exception for individual dusty sources, these values show slow variations as a function of position due to the combination of foreground and the overall distribution of gas and dust in that region (*Buchholz et al., 2013, 2011*). The polarization degree during flares of Sgr A* is variable to a degree and much stronger than that of the background that shows it is clearly source intrinsic.

3.3.3 Analysis of the polarized flux density distribution

The histogram of polarized flux density distribution of Sgr A* in its linear form (Fig. .3, left) and double logarithmic representation (see Fig. .3, right) is produced for the entire data and for the fraction of the data which is significant, based on our simulation, showed in Fig. 3.12. The distribution is normalized by the bin size and the total number of points. In order to better display the distribution of values the logarithmic histogram is used. In the following to formally describe and physically explain the measured polarized flux density distribution shown in Fig. 3.12 two different approaches are presented.

3.3.3.1 Best fits of the polarized flux density distribution and the goodness of fit

I determine the best fits to the data by using the maximum-likelihood method (see Section .2) which is maximizing the likelihood or log-likelihood functions.

$$L(\theta) = \prod_{i=1}^N P(X_i, \theta) \quad , \quad (3.8)$$

$$l(\theta) = \sum_{i=1}^N \ln P(X_i, \theta) \quad , \quad (3.9)$$

$L(\theta)$ and $l(\theta)$ are the likelihood and the log-likelihood function, respectively. $P(X_i, \theta)$ is the probability density function (PDF) for our data set $X_i = f_{p,1}, \dots, f_{p,N}$, where f_p stands for the polarized flux density, and θ for a vector of free parameters. I consider the significant polarized flux density values according to our simulation and obtain the best fit parameters, $\hat{\theta}$, by maximizing $l(\theta)$. Our data set of $N = 1019$ is fitted for three different models with distinct free parameters (see Table 3.5). I apply different theoretical PDFs to check which one is better describing our data:

$$P_{\log n}(f_p) = \frac{1}{f_p \times \sqrt{2\pi}\sigma} \exp \left[-\frac{(\ln f_p - \mu)^2}{2\sigma^2} \right] \quad , \quad (3.10)$$

$$P_{plaw}(f_p) = \begin{cases} 0 & \text{if } f_p \leq f_{p_0} + f_{p,min} \\ \frac{\alpha-1}{f_{p,min}} \cdot \left(\frac{f_p - f_{p_0}}{f_{p,min}} \right)^{-\alpha} & \text{if } f_p > f_{p_0} + f_{p,min} \end{cases} \quad , \quad (3.11)$$

$$P_{s.f}(f_p) = \begin{cases} nP_{\log n}(f_p) & \text{if } f_p \leq f_{p_0} + f_{p,min} \\ P_{plaw}(f_p) & \text{if } f_p > f_{p_0} + f_{p,min} \end{cases} \quad , \quad (3.12)$$

$P_{\log n}(f_p)$, $P_{plaw}(f_p)$ and $P_{s.f}(f_p)$ show lognormal, power-law, and step function PDFs respectively. α is the power-law slope and $f_{p,min}$ represents the lowest value to which the distribution of the data follows a power-law. f_{p_0} is a polarized flux density offset due to the remained faint stellar contamination. $(\alpha - 1)f_{p,min}^{\alpha-1}$ is the normalization factor that makes the power-law normalizable. In the case of the power-law model, the maximum likelihood estimator (MLE) for the parameter α is obtained by setting $\partial l / \partial \alpha = 0$.

$$\hat{\alpha}_{MLE} = 1 + n \left[\sum_{i=1}^N \ln \frac{f_{p,i}}{f_{p,min}} \right]^{-1} \quad , \quad (3.13)$$

where $f_{p,i}$, $i=1, \dots, n$, are the observed values of f_p such that $f_{p,i} \geq f_{p,min} + f_{p_0}$. For acquiring f_{p_0} and $f_{p,min}$ estimators, I choose f_{p_0} and $f_{p,min}$ in a way that the probability distribution of the measured data and the power-law model with α as the maximum likelihood

estimator, become as similar as possible (Clauset *et al.*, 2007). The similarity can be calculated through Kolmogorov-Smirnov (KS) test (Press *et al.*, 1992). The KS statistics (D) measures the difference between the model and data by calculating the maximum difference between the cumulative distribution functions (CDFs) of the observed data and the model:

$$D = \max_{f_p \geq f_{p,min} + f_{p_0}} |C_m(f_p) - C_o(f_p)| \quad . \quad (3.14)$$

$C_o(f_p)$ is the CDF for the data with observed values above $f_{p,min}$, and $C_m(f_p)$ is the CDF for the best fit power-law model and is calculated as below:

$$C_m(f_p) = \int_{f_{p_0} + f_{p,min}}^{f_p} P_{plaw}(f_p) df_p = \begin{cases} 1 & \text{if } f_p \leq f_{p_0} + f_{p,min} \\ -\left(\frac{f_p - f_{p_0}}{f_{p,min}}\right)^{1-\alpha} & \text{if } f_p > f_{p_0} + f_{p,min} \end{cases} \quad . \quad (3.15)$$

The f_{p_0} and $f_{p,min}$ estimators are determined by minimizing D. After estimating the MLE for each model and obtaining the fit parameters, I check which one of the models can describe the data best. There are many ways to do this test, the one that I use here is the reduced chi-square test. Table 3.5 and Fig. 3.13 show the best fit results and comparison between the data and different best fit models. The errors are determined by using the bootstrap method (Wall and Jenkins, 2012) (see Sec. .3).

In order to include the uncertainty of the photometry in investigating the measured polarized flux distribution, I convolved the power-law distribution with a Gaussian distribution with a sigma of the observational error:

$$P_{plaw+error}(f_p) = \int P_{plaw}(f'_p) \frac{1}{\sqrt{2\pi}\sigma} \exp\left[-\frac{(f_p - f'_p)^2}{2\sigma^2}\right] df'_p \quad (3.16)$$

where $P_{plaw}(f'_p)$ is the intrinsic polarized flux density distribution without observational errors. σ is constant about 0.25 mJy for our data sample up to 10 mJy (see Fig. 3.3). For higher polarized flux densities, the histogram becomes incomplete and the statistical errors have less effect compared to the time correlation bias (Witzel *et al.*, 2012). By convolving the power-law and considering the errors slope of it changes a little and χ^2/dof for the best fit changes from 1.13 to 0.68. Based on Table 3.5, the power-law (Eq. 3.11) is the best fit to our distribution.

3.3.3.2 The polarized flux density distribution for bright flare fluxes

I present the histogram of polarized flux density in Fig. 3.12. Our simulations have shown that the polarization degree can be recovered with a small uncertainty only for bright flare

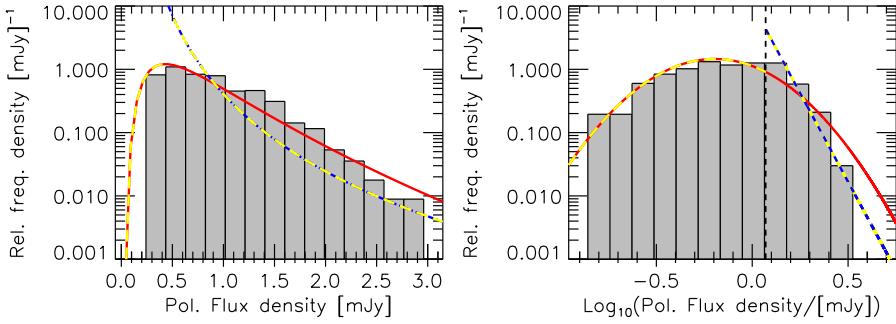


Figure 3.13: Left: The distribution of the polarized flux density. Different colors indicate fitted PDFs to the distribution. Red shows lognormal (Eq. 3.10), blue displays powerlaw (Eq. 3.11), and yellow shows the step function (Eq. 3.12). Right: Same as left but in the log-log space. Credit: *Shahzamanian et al. (2015)*, reproduced with permission ©ESO.

Table 3.5: The parameters obtained from the best fit to the polarized flux density distribution. Credit: *Shahzamanian et al. (2015)*, reproduced with permission ©ESO.

model	α	$f_{p,min}$	f_{p_0}	μ	σ	χ^2/dof
plaw	4 ± 0.14	0.5 ± 0.27	0.02	-	-	1.13
logn	-	-	-	-0.45 ± 0.14	0.63 ± 0.1	0.19
s.f: logn+plaw	4 ± 0.09	0.5 ± 0.13	0.02	-0.45 ± 0.01	0.63 ± 0.03	1.16

fluxes. Therefore, the properties of the polarized flux density (i.e. the product of the polarization degree and the total flux density) distribution can be obtained best for high polarized flare flux densities. I show a power-law fit to the data at high flux densities as a dot-dashed blue line. The slope α is fitted to a value of 4.00 ± 0.15 for high flare flux densities, which is very close to the value of 4.21 ± 0.05 measured for the total flux densities by *Witzel et al. (2012)* (see Fig. 3.14). The simulations predicted behavior (see Fig. 3.5 and Table 3.3).

Recovering this exponent for the polarized flare flux density distribution shows that the intrinsic polarization degree has not been strongly variable over the time interval from 2004 to 2012 and is centered around a fixed expected value (see section 3.3.1).

3.3.3.3 A heuristic analytic explanation of the polarized flux density distribution

The behavior of the entire sample of flares with significant polarized fluxes and polarization degrees is predicted by the simulations (see Figs. 3.5 – 3.7, and Tables 3.3 and 3.4 in section 3.3.1). I present here the heuristic model which is helpful for understanding the fact that the relative frequency density of measured polarized flux densities is much

broader in comparison to the relative frequency density of total flux density measurements as presented by [Witzel et al. \(2012\)](#) which was found to be consistent with a single-state emission process.

In the following $D(F_{K,pol})$ is called the relative frequency density of measured polarized flux densities as shown in Fig. 3.12. It can be compared to the distribution shown for the total fluxes for a large sample of light curves by [Witzel et al. \(2012\)](#) (see Fig. 3 therein) though the polarized flares have the limited number. I now consider that total flux density distribution has a similar shape for each randomly picked subset of K_s -band flux densities, and for all flux densities all polarization degrees are possible. This assumption will be commented later since is not fully justified. First, values belonging to total flux densities S_K are picked that can be attributed to a polarization degree bin p_i of width δp from $p_i - \delta p/2$ to $p_i + \delta p/2$ and the polarized flux densities would be $F_K \cdot p_i$. I measure the weights $w_i(p_i)$ for individual polarization states from the distribution shown in Fig. 3.8 (top). I express the polarized flux density distribution $D(F_{K,pol})$ as a product distribution that is a probability distribution constructed as the distribution of the product of (assumed to be) independent random variables $D(F_K)$ and p_i that have known distributions.

The corresponding polarized flux density distribution $D(F_{K,pol_i})$ by using the weights $w_i(p_i)$ for each polarization state can be written as

$$D(F_{K,pol_i}) = w_i(p_i) \cdot D(F_K \cdot p_i) \quad . \quad (3.17)$$

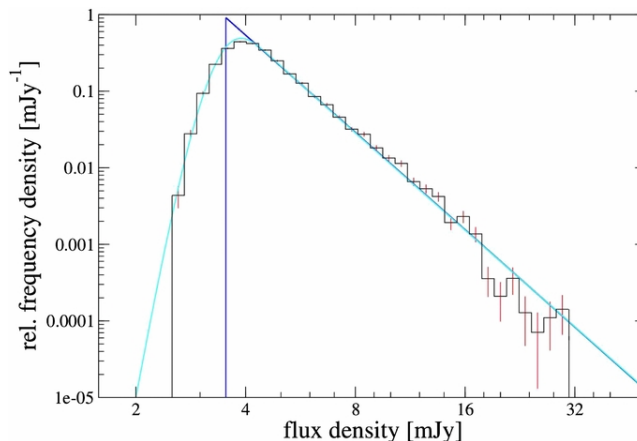


Figure 3.14: Histogram of flux density of Sgr A* obtained from [Witzel et al. \(2012\)](#). The best power-law fit is presented with the blue line and cyan line shows the power law convolved with a Gaussian distribution with 0.32 mJy sigma. Credit: [Shahzamanian et al. \(2015\)](#), reproduced with permission ©ESO.

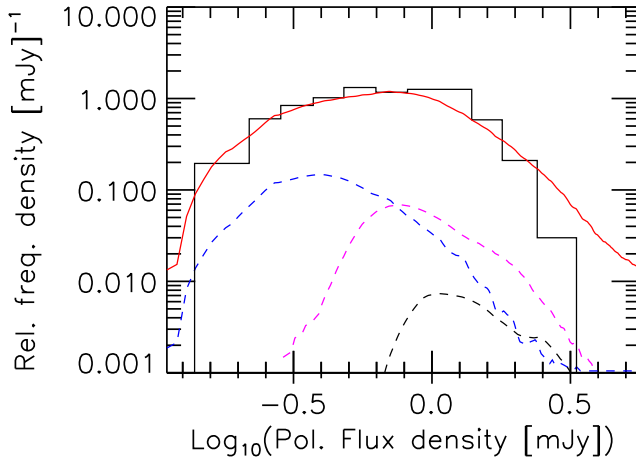


Figure 3.15: Calculated, from the light curves, relative number frequency of polarized flux density (Fig.3.12) and from our heuristic modeling (straight red). The contributions from flux densities with polarization degrees of $\leq 30\%$ (blue), $\geq 60\%$ (black) and in between (magenta) is shown in dashed curves. Credit: [Shahzamanian et al. \(2015\)](#), reproduced with permission ©ESO.

The polarized flux density distribution $D(F_{K,pol})$ can then be considered as a product distribution by summing over all N bins containing all polarization degrees p_i :

$$D(F_{K,pol}) = \sum_{i=1}^N D(F_{K,pol_i}) = \sum_{i=1}^N w_i \cdot D(F_K \cdot p_i) \quad . \quad (3.18)$$

The result of this modeling approach is shown in Fig. 3.15. In this figure the measured (as in Fig. 3.12) and modeled relative number frequency of polarized flux density are plotted and the combined contribution from different polarization states are shown. Due to the deficiency of bright flares with high polarization states the steep drops towards higher polarized flux densities. Undersampling of the brightest flares affects also this region. Our primary assumption that for all flux densities all polarization degrees are possible is not fulfilled in this region. Measured polarization degrees below 30% for flux densities above 5 mJy. Therefore, in this domain the number of flare events with high polarized flux densities is overestimated. Except this lack, however, the measured data is closely described by the model which implies that the broader distribution as formally analyzed in section 3.3.3 can indeed be described by combination of an intrinsic relative frequency total flux density histogram applied to the individual polarization states.

3.3.4 Relation between total flux density and polarization degree

I plot the K_s -band polarization degrees versus total flux densities in Fig. 3.16 (top) considering all the observed total flux densities for different epochs and their calculated polarization degrees. In this figure the data that result in significant measurements of polarization degrees are considered i.e. the data that correspond to positions shown in non-boldface in Table 3.3 are excluded. Fig. 4 shows the same plot for the entire data set. There is a clear trend in both plots that lower polarization degrees have higher flux densities for which the simulations show that the polarization data can be recovered very well, and polarization degrees are higher for lower total flux densities.

In order to analyze if this trend is due to small-number statistics, I perform a bootstrap test. I fit a line to the significant data points (see bold face positions in Table 3.3) by minimizing the least square and find a slope of $-21.7 \pm 1.25\% (\log_{10}(F/[mJy]))^{-1}$ and an intercept on the polarization degree axis of $34.3 \pm 0.74\%$. The uncertainties are obtained by bootstrap method (see Sect. .3) for 10^4 times (Wall and Jenkins, 2012). I find the Pearson's correlation coefficient value, which measures how linearly dependent the parameters are, to be -0.43 for the anti-correlated data. The correlation coefficient for the original data could have been obtained by chance. Therefore, for measuring the strength of its value and its significance, I shuffle the data 10^4 times and calculate the correlation coefficient each time for the resulted uncorrelated data sets. Then, I calculate the mean and standard deviation (σ) for the distribution of correlation coefficient values and check if the probability of the correlation coefficient of the original data was by chance or not. With a mean value of -10^{-5} the correlation coefficient distribution is almost zero and the standard deviation is 0.042. Therefore, I find that the Pearson's correlation coefficient for this data has a $\sim 10\sigma$ offset from the mean value of 0.0 that one finds for uncorrelated data sets. The resulting correlation is represented by the dashed line in Fig.3.16 (top).

The boundary condition of detecting significant polarized flux density indicates that the lower left, approximately triangular, region of any flux-polarization plot remains empty. The detection limit is on the order of 0.3 mJy for polarized flux density. In the systematic offset of 5% in the diagram the systematic uncertainty in the degree of polarization of about 5% is reflected. The polarization degrees measured at low total flux densities show a much asymmetric, stronger, scatter than those obtained at higher total flux densities as I have shown in Table 3.3. This is the reason why the extension of the point cloud toward high values of p decreases with increasing total flux density. Therefore, the asymmetrically distributed uncertainties that dominate the measurements at low flux density levels most likely cause the apparent correlation.

The results of the simulation already imply the apparent correlation (see Figs. 3.5, 3.6 and Table 3.3). For intrinsic polarization degrees and total flux densities an apparent negative correlation between polarization degree and total flux density is shown in Table 3.3

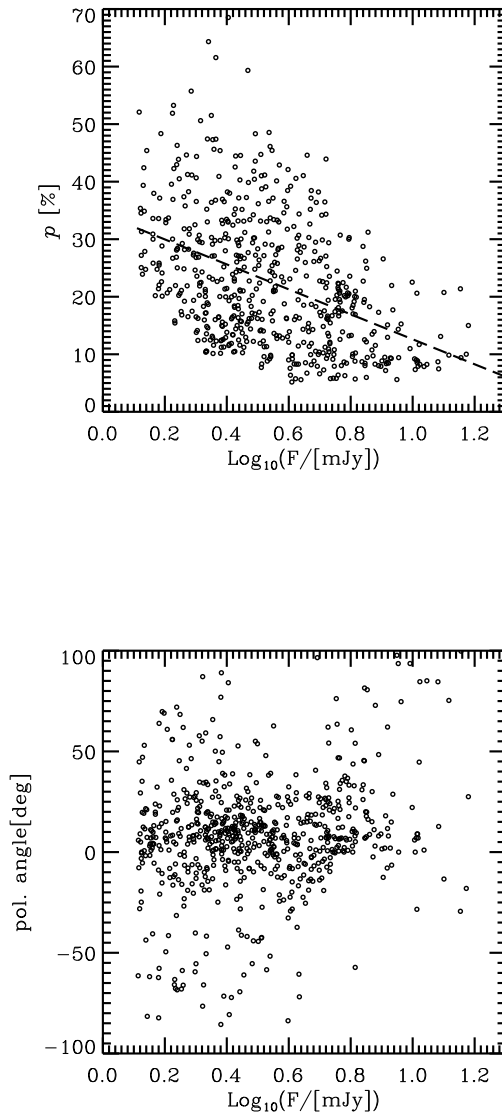


Figure 3.16: Top: The correlation between total flux density and polarization degree only for the significant data (based on Table 3.3). The best fitted linear line is shown in dashed line. Bottom: The correlation between total flux density and polarization angle just for the significant data. Credit: [Shahzamanian et al. \(2015\)](#), reproduced with permission ©ESO.

which also encloses the dashed line shown in Fig. 3.16 (top). Furthermore, I present for all the data with significant polarization degrees the angle as a function of total flux density. As it is shown in this figure, there is no correlation between total flux density and polarization angle. The same plot for the whole data set is presented in Fig. 4.

3.4 Discussion

3.4.1 Mechanisms that contribute to the polarization

Polarimetric observations can help to discriminate between source geometry and different radiation mechanisms. In case of active galactic nuclei, polarization over the range of spectral bands has been frequently used to constrain the magnetic field in their accretion disks (Silant'ev *et al.*, 2009) or to determine the structure of scattering regions (see e.g. Goosmann and Gaskell, 2007). We can use preferred direction of polarization to suppress or support the interpretation in terms of the synchrotron mechanism, which is thought to produce a particularly high polarization degree. Scattering off material close to the axis of symmetry or (as in the case of synchrotron emission) the intrinsic emission mechanism can produce polarization perpendicular to the axis. Optical and UV observations are often discussed in this context, however, these are not particularly useful for Sgr A* and therefore the study of the infrared polarization properties is important.

The strong polarization and rapid variability indicate that the emission from Sgr A* is dominated by synchrotron emission. The linear polarization degree and angle are linked to the magnetic field structure and source geometry. Therefore the polarization measurement can be used to evaluate the importance of various emission mechanisms. In case of Sgr A* the situation is complex, since neither is it clear if it has a permanent accretion disk nor is it clear if it has a permanent jet.

These phenomena can happen as transients and come along with properties for the expected polarization degree and angle of the possible mechanisms. The extraction of energy from a Kerr black hole can be permitted by the Blandford-Znajek process (Blandford and Znajek, 1977). It causes a strong poloidal field, but needs an accretion disk to be present. Based on model calculations accretion disks may be dominated by ordered toroidal magnetic fields where the \vec{E} -vector of the polarized radiation may be perpendicular to the equatorial plane (Broderick and Loeb, 2006; Falcke and Markoff, 2000; Goldston *et al.*, 2005). However, in these systems magnetic field configurations can also be very turbulent (Shakura and Sunyaev, 1973; Balbus and Hawley, 1991). Field structure of hot spots within the disk is mostly vertical poloidal field structure (Eckart *et al.*, 2006c) and the spots may be coupled with reconnection events from magnetically affected accretion disks (Dexter *et al.*, 2014). The polarization vector in jet components can be perpendicular or parallel to the jet direction (Pollack *et al.*, 2003; Gabuzda *et al.*, 2000). It should be also

mentioned in this context that Antonucci (1982) found that radio galaxies frequently show a similar parallel alignment of the polarization and radio axis, but there is also a subclass presenting a perpendicular direction.

However, characteristic polarization pattern can also be disturbed by some mechanisms. The polarization angle can be dependent on projection effects (e.g. in the case of an inclined toroidal field) and can also be rotated in the strong gravitational field of the super-massive black hole if the line of sight to the radiating region passes close to it. As a result of this lensing effect depolarization may occur especially if complete or partial Einstein rings are formed. A complex source structure may also lead to depolarization. The polarization angles vary across the source and average out in larger beams in both cases. Strong depolarization due to Thompson scattering or Faraday effect at NIR wavelengths can be neglected. In future obtaining structural information at a higher angular resolution is necessary to combine the information on polarization and source structure to get definitive conclusions on the importance of various mechanisms. As a consequence of the situation described above and with the current angular resolution one may expect that - within some uncertainties - the polarization angle of the emerging emission is either perpendicular or parallel to the emitting source structure.

3.4.2 Variable polarized flux density

I obtain for the whole data variations in flare flux density of $>15\text{mJy}$ and a large variation in polarization degree of - in part - larger than 50%.

However, given the measured flux density (and its error) in orthogonal polarized channels simulations of the resulting observed polarization parameters show that, at low flux densities a significant part of the variation in polarization degree is the result of measurement uncertainties. The uncertainty in recovering the intrinsic degree of polarization for flux density levels above 5 mJy is only on the order of 5% based on the simulations presented in Section 3.3.1. At this flux density level, this value is noticeably smaller than the measured variation in degree of polarization at high flux densities of up to 30%. This shows an intrinsic variation of the polarization state of Sgr A* during flare activities.

The defined range of polarization of 10-30% is lower than the maximum polarization degree of about 70% that can be measured for synchrotron radiation in tangled magnetic fields or a broad distribution of electron pitch angles with respect to the field lines (Moffet, 1975; Ginzburg and Syrovatskii, 1965). Since the polarization is spatially variable across the source and averaged in the observers beam the high values of polarization degree are rarely observed. Therefore, I can conclude that depolarization caused by a complex source structure is at work.

The power-law slope of ~ 4 of the number density of the polarized flux density for high flux densities is very close to the slope in number density distribution of the total flux densities obtained by [Witzel *et al.* \(2012\)](#). This clearly shows that there is a preferred value or range of intrinsic polarization degrees.

Obtaining this slope was unpredictable since it is coupled to the previously unknown fact that the range of polarization degrees is limited to a small and well defined interval. The slope of the power-law flux density distribution implies a nonlinear statistical variability behavior of Sgr A* as presented in [Witzel *et al.* \(2012\)](#). This behavior is characterized by a linear rms-flux relation for the flux density range up to 12 mJy on a timescale of 24 minutes and a dominant timescale in that variability at about 150 minutes ([Meyer *et al.*, 2009](#)).

The slope in the number density of the polarized flux density would have been affected if the variation of the range of polarization degrees was not small over the past years (2004-2012). Together with the result from comparing the distributions of polarization degrees and their relative uncertainties this is a clear evidence of intrinsic variability in the polarization degree. In agreement with this, in section 3.3.2 I derived for the entire set of significant polarization degrees its intrinsic relative variability must be on the order of 30%.

Therefore, the distribution of polarized flux density as described formally in Section 3.3.3 can be considered as being consisted of the contributions of populations of flare events with variable flux densities and intrinsic polarization degrees that change over a narrow range between about 10% and 30% but a nearly constant polarization angle. A well defined preferred polarization angle and a preferred range in polarization degree during a time interval of 8 years (2004-2012) strengthen the assumption of a rather stable geometry for the Sgr A* system, i.e. a rather stable jet/wind and/or disk orientation.

Moreover, a comparison of the simulations presented in section 3.3.1 to the observed data indicates that the observed anti-correlation between total flux density and polarization degree is most likely dominated by an observational effect as a result of asymmetrically distributed uncertainties in resolving of the polarization degree for small flare flux densities (near our acceptance flux density and below). As a result, it is impossible to realize whether the polarization state of Sgr A* is intrinsically varying at flux densities below 2 mJy, with the current instrumentation. The brighter flux density flares are systematically less polarized than the lower flux densities based on the observed apparent anti-correlation between polarization degree and total flux density. Based on the results of [Zamaninasab *et al.* \(2010\)](#) such a behavior may be expected that the polarized flares compared to the randomly polarized red noise show a signature of emitting matter orbiting around the central black hole. A bright geometrically depolarized emission during a flare

Table 3.6: Comparing the polarization estimations of Sgr A* determined in this chapter with the reported values in the literature. Credit: *Shahzamanian et al. (2015)*, reproduced with permission ©ESO.

obs.date	degree		angle		degree		angle	
	Eckart+04		Zamaninasab+10		This work			
13 June 2004	~20%	-20°-+70°	~20%	-20°-+70°	10%-30%	-60°-+40°		
30 July 2005	12%-25%	40°-+80°	12%-25%	~40°	5%-20%	10°-+100°		
15 May 2007	-		20%±20%	-50°-+50°	5%-20%	-50°-+20°		
17 May 2007	-		20%±10%	-30°-+20°	5%-20%	-50°-+50°		

event is caused due to the formation of partial Einstein rings and mild relativistic boosting during the approach of an emitting source component. In other publications (see e.g. *Eckart et al., 2006b*; *Meyer et al., 2006b*; *Trippe et al., 2007*), polarization modifications caused by decreasing or increasing the flux densities have been presented.

A comparison of polarization degree and angle between this work and former NIR polarization studies of Sgr A* is shown in Table 3.6. It ensures that the results presented in this work are consistent with those of previous publications despite of different methods of obtaining the polarization information. The agreement is satisfactory as shown in Fig. 3.16 and expected from the findings in Section 3.3.3.3, despite the strong source variability and different ways of deriving the observables (see *Witzel et al., 2011*, for details).

3.4.3 The preferred polarization angle

I present that the polarized flux density distribution is coupled to the total flux density distribution obtained by *Witzel et al. (2012)* and there is a preferred polarization angle of $13^\circ \pm 15^\circ$ (see Fig. 3.17). It is shown by the simulations presented in Section 3.3.1 that even at high flux density levels (e.g. ≥ 5 mJy) the uncertainty in the polarization angle is dominated by the statistical uncertainty (10° to 15°) in recovering a value that is considered to be constant. Therefore, it can be concluded that the intrinsic variation of the polarization angle is smaller than the currently obtained variability and probably on the order of 10° .

However, It can be now said in the discussion in section 3.4.2: In general the variations are smaller if corrected for obtained uncertainties. From Fig. 3.16 (bottom) which shows the relation of polarization angle and flux density and the uncertainties expected for the angle, I find that there are variations of the polarization angle in the range of 30° to 100° , for flare fluxes higher than 6mJy (about 13 % of the time; see Fig. 3 in *Witzel et al. (2012)*), while the uncertainties are less than about 10° (see Tables 3.3 and 3.4). Therefore, there

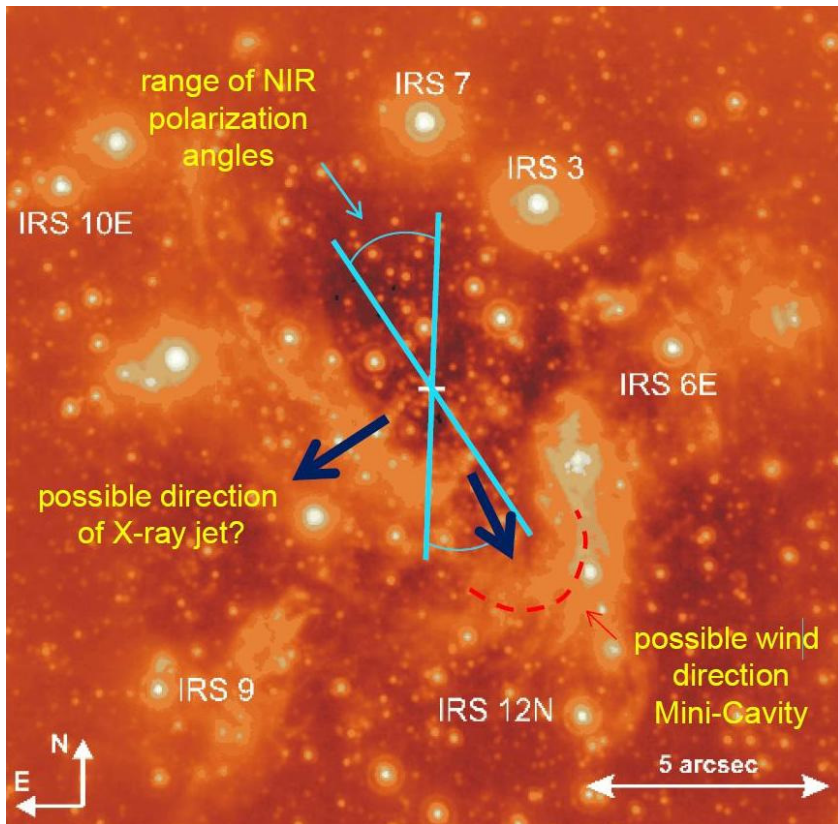


Figure 3.17: Direction of intrinsic polarization angle of Sgr A* in the Galactic Center. The range in which the NIR polarization angle varies are shown in cyan lines. The radio to X-ray domain imaging and spectroscopy observations are presented, the dark blue arrows show a) the direction of wind responsible for the formation of the mini-cavity and b) a jet perpendicular to it. Credit: *Shahzamanian et al. (2015)*, reproduced with permission ©ESO.

is a combined behavior with a preferred polarization angle of about 13° at which the flare flux densities are above 2 mJy for about 30% of the observing time and clear excursions that cover a much larger range than expected from observational/statistical uncertainties, that certainly shows the source intrinsic nature of the measured polarization of Sgr A*.

The preferred NIR polarization angle may also be linked to the orientation of the Sgr A* system and to polarization properties in the radio cm- to mm-domain. The linear polarization of Sgr A* in the radio cm-regime is very small, however, the source has a fractional circular polarization of around 0.4% (Bower *et al.*, 1999a,b). Towards short mm-domain the circular polarization decreases (Bower *et al.*, 2003), where Macquart *et al.* (2006) report in the mm-wavelength a small percent of variable linear polarization from Sgr A*. The degree and angle of polarization in the sub-mm are likely linked to the general orientation of the source or the magnetic field structure. One may expect a link between the preferred NIR polarization angle and the NIR/radio structure of Sgr A*, as in particular the NIR flare emission very likely comes from optically thin synchrotron radiation (Eckart *et al.*, 2012a). Interstellar scattering is small at millimeter domain and allows insight to the intrinsic source structure of Sgr A*. An intrinsic major axis position angle of the structure of $95^\circ \pm 10^\circ$ (3σ) is reported (Bower *et al.*, 2014). This angle of the radio structure is orthogonal to the preferred infrared polarization angle within the uncertainties. It is currently uncertain how the intrinsic polarization angle of Sgr A* can be related to external structures.

Eckart *et al.* (2006b,a) report an elongated NIR feature, an elongated X-ray feature (see also Morris *et al.*, 2004) and a more extended elongated structure called LF, XF, and EF in Figure 9 by Eckart *et al.* (2006b), in a range of position angles between 120° and 130° . These features may be linked with a jet phenomenon. In this case the preferred NIR polarization angle may be associated with the jet components at the foot point or close to the jet as for jet components the polarization may be perpendicular or along the jet direction.

It is also likely that the NIR emission originates in hot spots on an accretion disk in which the E-vector is mostly perpendicular to the equatorial plane like a sunspot geometry. Yuan *et al.* (2009) present such a magneto-hydrodynamical model for the formation of episodic fast outflow. A jet or wind perpendicular to the intrinsic radio structure of the disk along the position angle of the NIR polarization, may be derived by acceleration of coronal plasma due to reconnection. At a position angle of about 193° (i.e. $13^\circ + 180^\circ$), the mini-cavity (presented as a dashed line in Fig. 3.17) that may be due to the interaction of a nuclear wind from Sgr A* is located. Additional observational support for the presence of a fast wind from Sgr A* under that position angle is the cometary tails of sources X3 and X7 reported by Mužić *et al.* (2010). I will conclude and summarize the main results of the NIR polarimetry of Sgr A* in Chapter 5.

NEAR INFRARED POLARIZED OBSERVATIONS OF THE DUSTY S-CLUSTER OBJECT (DSO/G2) AT THE GALACTIC CENTER

4.1 Introduction

The main goal of Galactic Center observations has been set on studying an infrared (IR) excess source since 2012, which was detected by [Gillessen *et al.* \(2012\)](#) as a fast moving object approaching the position of the central super-massive black hole (SMBH) of our Galaxy, Sagittarius A* (see Fig. 4.1). It has been interpreted as a combination of core-less gas cloud and dust called G2 ([Gillessen *et al.*, 2012, 2013](#); [Pfuhl *et al.*, 2015](#)) and also Dusty S-cluster Object, shortly DSO ([Eckart *et al.*, 2013](#)). This source passed its closest approach to the SMBH in May 2014 and moves on a highly eccentric orbit. Given its eccentricity, it has been suspected that it can produce extraordinary accretion events on to the galaxy's central black hole (e.g. [Shcherbakov, 2014](#); [Abarca *et al.*, 2014](#); [Scoville and Burkert, 2013](#); [Sądowski *et al.*, 2013](#)).

If DSO/G2 is a pure gas cloud of a few Earth masses ([Gillessen *et al.*, 2012](#)) it should have been formed recently (1990-2000) therefore it should have been observed during the total time of its existence. As a result, the pure gas scenario seems unlikely and several authors have introduced scenarios suggesting the presence of a central star for this source (e.g. [Murray-Clay and Loeb, 2012](#); [Eckart *et al.*, 2013](#); [Scoville and Burkert, 2013](#); [Ballone](#)

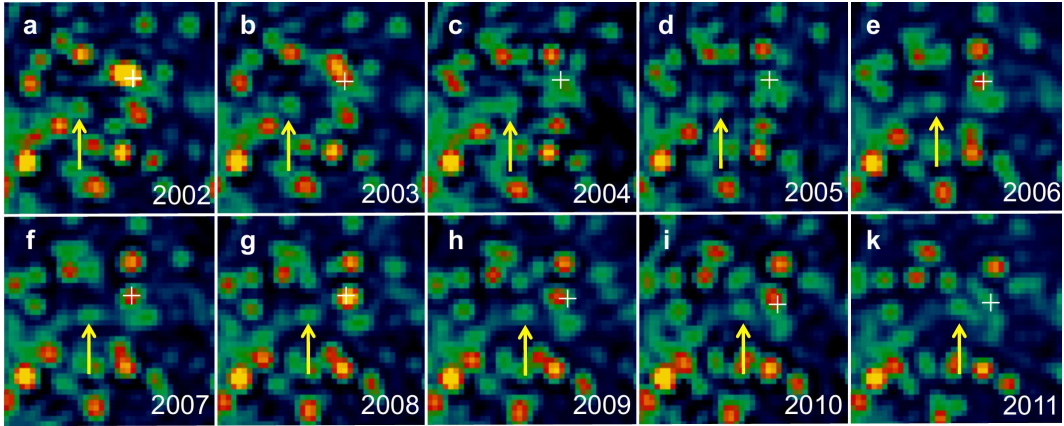


Figure 4.1: The GC central arcsecond which is centered on the G2/DSO (marked by the yellow arrows) after deconvolution in L -band images. The position of Sgr A* is displayed by the white cross. North is up and East is left. Image credit: Gillessen et al. (2012).

et al., 2013; Phifer et al., 2013; Zajaček et al., 2014; Witzel et al., 2014; Valencia-S. et al., 2015). Considering the stellar nature, DSO/G2 did not need a recent formation and will not be disrupted when reaching its closest point to the SMBH. One possibility is that it was formed in the stellar cluster - possibly within the disk of young stars at a distance of few arcseconds from the Galactic Center. After forming there it may have moved on its current remarkably eccentric orbit by gravitational interaction with massive stars (Murray-Clay and Loeb, 2012; Scoville and Burkert, 2013). Using hydrodynamical simulations, Jalali et al. (2014) showed that young stars could form within small molecular clumps very close to SMBHs on eccentric orbits around the black hole. They showed that for such orbital configurations, the orbital (geometrical) compression and gravitational potential of the SMBH increase the density of cold gas clumps to reach the suitable threshold values for star formation.

The idea of the compactness of DSO/G2 is supported by the L -band observations of this source close to the peribothron, which means the source cannot follow a pure gas model (Ghez et al., 2014; Witzel et al., 2014). Eckart et al. (2013) revealed the first K_s -band identification of DSO/G2 from the VLT continuum imaging data with the magnitude of ~ 18.9 . They used the M -band measurement by Gillessen et al. (2012) to get the spectral decomposition of this source that leads to an upper limit of $\sim 30 L_{\odot}$ on its luminosity. The H , K_s , and L -band continuum measurements can be linked either by an unusually warm dust component at a temperature of 550-650 K or a stellar source enshrouded in the dust at a temperature of ~ 450 K (see Fig. 4.2). The $H - K_s > 2.3$ color limit strengthens the scenario that the DSO/G2 is a dust-enshrouded star rather than a core-less cloud of gas

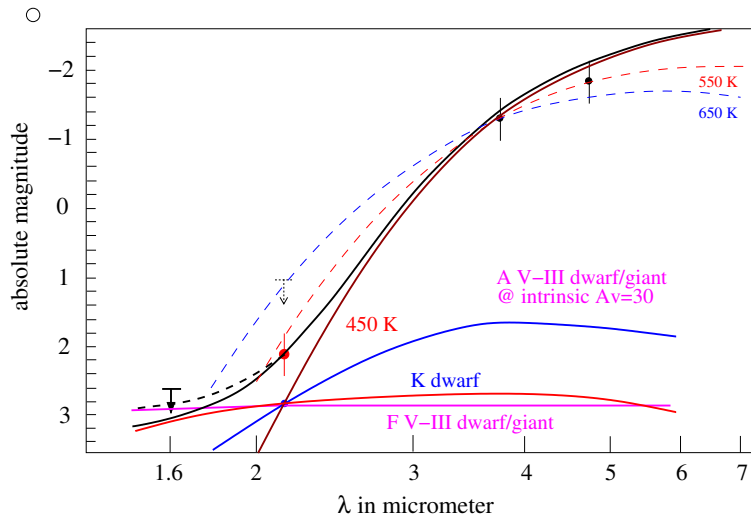


Figure 4.2: The decomposition of DSO spectrum. The points represent the L -, K_s , and H -band magnitudes estimated by Eckart et al. (2013) and the M -band estimation by Gillessen et al. (2012). A warm dust with temperatures of 550 K and 650 K can explain the measurements (red and blue dashed curves). Different stellar types (solid blue, red, and magenta lines) embedded in the 450 K dust shell (solid brown line) can create the black line that fits all the measurements in different NIR bands. Image credit: Eckart et al. (2013).

and dust (Eckart et al., 2013). I will refer to this source as DSO in the henceforth.

The mass of this object is less than the typical mass of S-cluster stars ($20M_{\odot}$) but more than what was presumed for a pure gas source. Valencia-S. et al. (2015) report NIR observations of the DSO during its approach to the SMBH at the Galactic Center from February to September 2014, that were carried out with SINFONI at the ESO Very Large Telescope (VLT). They detect spatially compact Bry line emission from this source before and after its peribothron passage (see Fig. 4.3) and also an increase in Bry line width which can show that the DSO is a young accreting star with a dust shell. The orbital parameters of this object were obtained using the observational data. Comparable to the previous estimates (e.g. Meyer et al., 2014b), Valencia-S. et al. (2015) estimate an ellipticity $e = 0.976$ and a peribothron distance of about 163 ± 16 AU with a half-axis length of about 33 mpc. When the DSO reaches the peribothron, velocity dispersion increases in the accretion flow toward the central star as a result of tidal stretching and disruption of the envelope (Eckart et al., 2013; Zajaček et al., 2014). Witzel et al. (2014) shows that the L -band emission of the DSO compared to its Bry emission obtained by Pfuhl et al. (2015) is more compact. This presents that the L -band emission comes from an optically thick dust envelope around a central star while the Bry emission originates from the hot

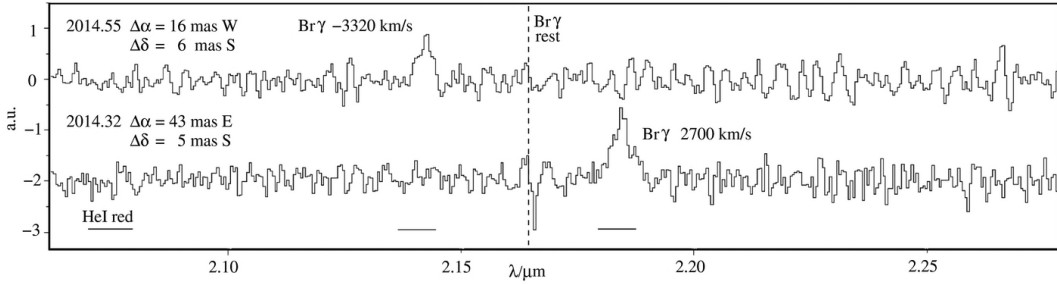


Figure 4.3: Bottom: the pre-pericenter redshifted $\text{Br}\gamma$ emission as a single peak in the NIR spectrum.; Top: the post-pericenter blueshifted emission of $\text{Br}\gamma$ emission as a single peak in the NIR spectrum. Image credit: Valencia-S. et al. (2015).

gas, which is externally heated by ionized photons of the stars close to the DSO. However, Valencia-S. et al. (2015) do not detect significantly tidally stretched and extended $\text{Br}\gamma$ emission.

The DSO is not the only infrared excess source in the S-cluster of the GC, see Fig. 4.4 that presents more dusty sources in this region (Eckart et al., 2013; Meyer et al., 2014b). These sources might be dust enshrouded pre-main sequence stars that if they move through the medium with a supersonic speed, bow shock structures can be created. One of these bow shocks shown in the figure is the X7 source (Mužić et al., 2010).

Imaging polarimetry is a strong technique for analyzing dusty regions such as coreless dusty objects and/or circumstellar dusty environments. The analysis of polarization allows us to estimate the dust properties and the object geometries quantitatively. Intrinsic polarization of stars can be produced only if the system is not symmetric. When the radiation field of the star is not spherical due to a geometric distortion, e.g. when the star develops a bow shock, or if its photosphere surface brightness is not uniform, i.e. influenced by the presence of bright spots, the asymmetry can occur. Therefore, supplementary to considering the line emissions and continuum from the DSO, analyzing the light's polarization can be very helpful in determining the properties and nature of this source. The DSO polarization should be only dependent on the local magnetic field if the object is just a dust blob and the dust grains orientation is influenced by the magnetic field. On the other hand, if the object is a low-luminosity bow shock, the polarization is obtained by the bow-shock morphology. If the medium is homogeneous, the E-vectors are predicted to be perpendicular to the direction of motion. If the DSO's dust shell is a disk, then the measured polarization depends on the disk inclination.

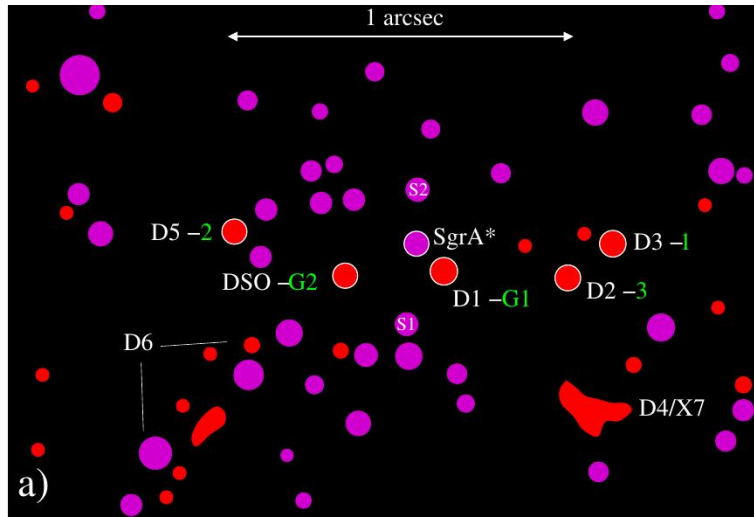


Figure 4.4: The GC central arcseconds and its Infrared excess sources positions obtained from K_s - and L-band observations, reported by Eckart et al. (2013) in white color with the exception of Sgr A* and by Meyer et al. (2014b) in green color. Image credit: Eckart et al. (2015)

In this chapter I analyze the NIR polarimetric imaging data taken with NACO at the ESO VLT using its Wollaston prism to analyze the polarization properties of the DSO. In Section 4.2, I begin with the description about the observations details, then explain the data reduction and finding the position of the DSO in the images. In Section 4.3, I discuss the results of the applied flux density calibration method: lightcurves, polarimetry measurements, and their statistical analysis. I summarize and discuss the implications of my results in Section 4.4.

4.2 Observations and data reduction

The NIR observations have been carried out at the ESO VLT on Paranal, Chile. The data were obtained using NACO, its Wollaston prism, and the half-wave retarder plate. The AO loop was locked on IRS7 located $\sim 5.5''$ north from Sgr A*, using the NIR wavefront sensor. We collected all K_s -band data of the GC taken with the S13 camera in 13 mas pixel scale polarimetry mode from 2004 to 2012. I used the reduced data sets as presented in Table 3.1 of Sect. 3.2 of the previous chapter.

The PSF varies during the observations because of the weather condition changes. Therefore, based on the PSF obtained from the stars in the field of view at the observing time, the quality of each epoch was determined. From the combination of the best quality

Table 4.1: Galactic Center Observations Log. Credit: *Shahzamanian et al. (2016)*, reproduced with permission ©ESO.

Date (DD.MM.YYYY)	Start time (UT)	Stop time (UT)	Number of frames	Integration time (sec)
25.05.2008	06:05:20.32	10:35:38.65	250	40
27.05.2008	04:52:04.92	08:29:38.07	184	40
30.05.2008	08:24:33.51	09:45:25.69	80	40
01.06.2008	06:04:51.56	10:10:26.78	240	40
03.06.2008	08:37:23.56	09:58:58.85	80	40
18.05.2009	04:37:55.08	10:19:54.10	286	40
27.05.2011	04:49:39.82	10:27:25.65	334	45
17.05.2012	04:49:20.72	09:52:57.08	256	45

exposures (with seeing $< 2''$) of each observing night, I produced a data cube. I got the median of the spatial pixels of the combined cube images in order to obtain a final image with longer integration time on the source and higher signal-to-noise-ratio (S/N). As a result, I cannot analyze the flux density and polarimetry variability on shorter time scales. I co-added all the observing nights in 2008, since the position of the DSO should not change much within a few months. Table 4.1 presents observation dates, number of exposures, and integration times of the data sets used for this study before their combination. The Lucy-Richardson deconvolution algorithm was applied on the obtained image of each year created from the data cube, for the purpose of aperture photometry. From the isolated stars close to the DSO position, the PSF was extracted using the IDL-based StarFinder routine (*Diolaiti et al., 2000*). The resulting median cubes of the four polarized channels of the individual observing years were aligned by performing the cross-correlation algorithm. The image was restored by convolution of the deconvolved image with a Gaussian beam with a FWHM of about 60 mas. Figure 4.5 shows the resulting images in 2008, 2009, 2011, and 2012 for the 90-degree channel. The DSO was clearly detected in its continuum emission in all channels of all the years.

4.2.1 Position of the DSO

I obtained the position of the DSO in individual observing years based on the Bry traced orbit from *Meyer et al. (2014b)* and *Valencia-S. et al. (2015)*. This source was confused with S63 between the years 2004 and 2007 and could not be determined from the background. It begins to be distinguished and resolved from stellar confusion from 2008. I used the data set shown in Table 4.1 to study the flux density and polarimetry of DSO.

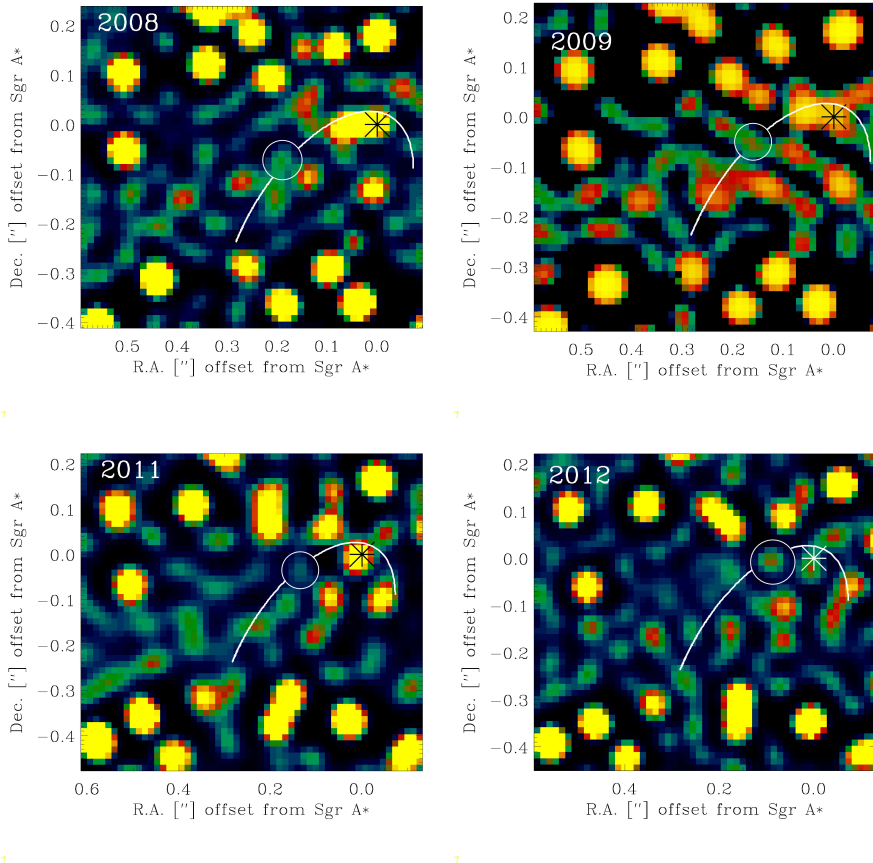


Figure 4.5: The deconvolved median images of K_s -band of the GC central arcsecond in polarimetry mode (90° polarization channel) of years 2008, 2009, 2011, and 2012 from top left to bottom right. The DSO location is presented by a circle on its orbit. The asterisk shows the position of Sgr A*. In all the images north is up and east is to the left. Credit: *Shahzamanian et al. (2016)*, reproduced with permission ©ESO.

4.3 Results

4.3.1 Lightcurves

I measured the flux density of the DSO by aperture photometry using 30 mas radius circular apertures in each observing year. The flux density calibration of the DSO was done similarly to that of Sgr A* discussed in details in Sect. 3.2.1. I used the same flux density calibrators, since the position of the DSO is very close to the Sgr A* position. The photon counts in each aperture of the DSO and the calibrators close to it were added and then the resulting values of two orthogonal polarimetry channels were also added to obtain the total flux densities. Then the obtained flux densities were corrected for the background contribution and the extinction (see Sec. 3.2.1).

Subsequently, I obtained the light curve for the years 2008, 2009, 2011, and 2012, as shown in Fig. 4.6. Uncertainties of the obtained DSO flux densities were measured by estimating the observational noise in ten apertures located in the background close to the position of the DSO. The DSO does not present any intrinsic flux density variability in the K_s -band based on our data set. This can be because of either an irregular variability or a period of variability not matching the time resolution of our data. However, any conclusion on the flux density variability and the effect of stellar contribution on the flux density measurement, considering the limited data sample, cannot be made at this point.

4.3.2 Polarimetry

We derive the linear polarization degree p and angle ϕ of the DSO by obtaining normalized Stokes parameters (I , Q , U , V) from the observed flux densities of this source in orthogonally polarized channels (see Equations 3.1 to 3.5 in Chapter 3). It is not possible to estimate circular polarization in normalized Stokes V since NACO is not equipped with a quarter-wave plate. The circular polarization of stellar sources in the GC is very small (Bailey *et al.*, 1984), therefore we presumed that it can be neglected and set to 0. However, circular polarization may be produced by multiple scattering in the case of dusty sources that have a high dust density.

Witzel *et al.* (2011) obtained a model to correct the instrumental polarization induced in the measured polarization. The model multiplies a combination of Mueller matrices for different elements of the telescope with the derived Stokes vectors. I implemented their model to correct for the instrumental polarization effects, where the measured polarization parameters can be estimated with an accuracy of $\sim 5^\circ$ in polarization angle and $\sim 1\%$ in polarization degree (Witzel *et al.*, 2011). The results of polarimetry measurements for our data set are presented in Table 4.2. Based on the measured values of p and ϕ for different years, the DSO is polarized ($p > 20\%$) with a polarization angle that varies as it moves along its orbit.

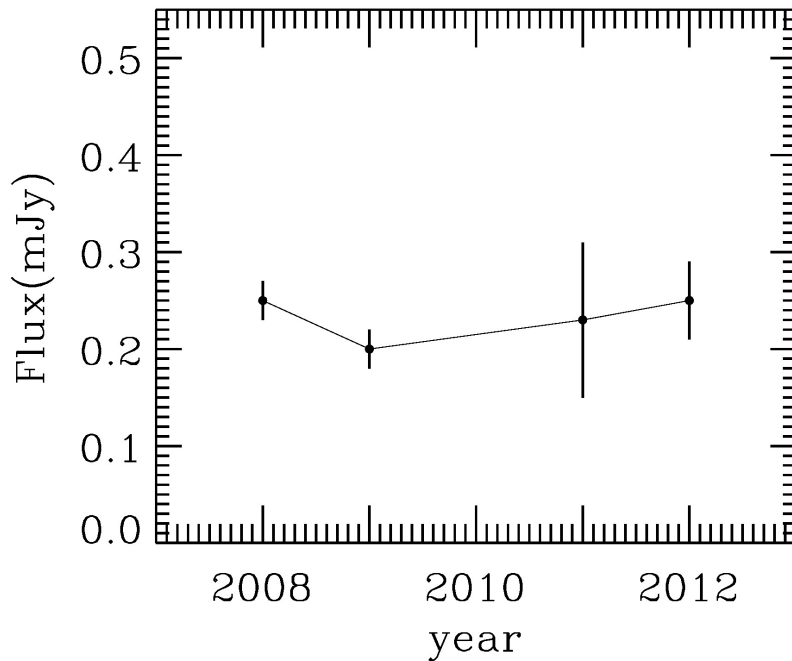


Figure 4.6: NIR K_s -band light curve of the DSO obtained in polarimetry mode in years of 2008, 2009, 2011, and 2012. Credit: *Shahzamanian et al. (2016)*, reproduced with permission ©ESO.

Figure 4.7 shows a schematic illustration of the DSO polarization angle change when the source moves on an eccentric orbit around the position of Sgr A* before it approaches the peribothron. Standard error propagation for estimating the polarization uncertainties cannot be applied here since the errors on Q and U , compared to the measured values, are not small. Moreover, even if the flux density values in different polarimetry channels are large, Q and U can be close to zero. Also, the polarization degree and angle are mostly not Gaussian distributions.

It is important to note that only when the S/N is high, the measured (or observed) polarization degree and angle of any astrophysical object are good estimations of the source intrinsic properties. It is possible to obtain polarization degrees that are unphysically

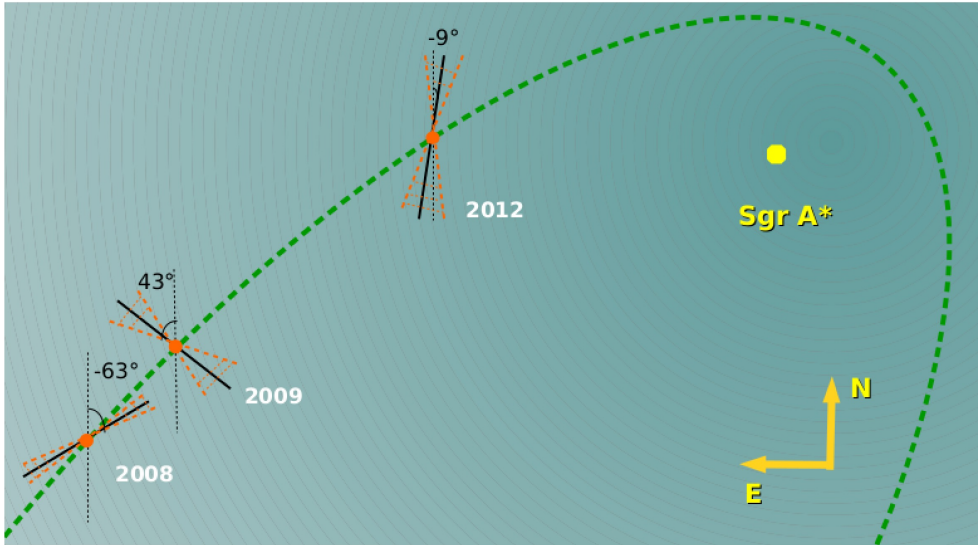


Figure 4.7: Sketch illustrating the DSO polarization angle variation while it moves on the eccentric orbit around the position of Sgr A* during three years. The range of possible values of the polarization angle (see Table 3) are shown in orange shaded area. Credit: *Shahzamanian et al. (2016)*, reproduced with permission ©ESO.

higher than 100% because of the observational uncertainties, since the polarization degree is a positive defined quantity that at low S/N becomes biased to higher values (than the intrinsic p of the source). The yearly stacked images in 2008, 2009, and 2012 have a medium S/N of $\sim 6 - 10$ and in 2011 a low $S/N \sim 2.5$. The distribution of the observed polarization degree can be described by a Rice function (*Serkowski, 1958; Vinokur, 1965*) in the first three cases; while this function cannot properly model the high skewness of the polarization degree distribution in the latter (*Simmons and Stewart, 1985*). The observed polarization-angle distribution depends on the intrinsic polarization degree and flux-density S/N . We considered as null hypothesis that the source is intrinsically not polarized, to calculate the significance of the obtained DSO polarization. Therefore, the

Table 4.2: Polarimetry estimation of the DSO. Credit: *Shahzamanian et al. (2016)*, reproduced with permission ©ESO.

Observing year	p	ϕ
2008	30.14%	-62.87°
2009	32.6%	42.92°
2011	29.9%	18.125°
2012	37.64%	-9.67°

observed polarization degree p_{obs} and angle ϕ_{obs} are only produced by the observational uncertainties. We estimated f_0 , f_{90} , f_{45} , and f_{135} for this test from the observed total flux density I_{obs} considering $p = 0\%$ and $\phi = 0^\circ$ presuming the intrinsic flux density to be the same as the observed $I = I_{obs}$. To simulate the effect of noise in the polarization channels, we added random noise from a normal distribution with $\sigma(f_X) = 0.7\sigma(I)$, where $\sigma(I)$ is the uncertainty of the observed total flux density.

Using Eqs. (1)-(6), we used Monte Carlo method for such a set-up to estimate 10 000 times the observed polarization degree and angle. Figure 4.8 shows the p_{obs} distributions for the observations in 2008, 2009, 2011, and 2012. These distributions show the probability to obtain a certain polarization degree considering the null hypothesis. The most probable observed polarization-degree in 2008, where S/N is high, is $\sim 9\%$ with 68/100 of the possible measurements (see Fig. 4.8). As a result, estimating the polarization degree of DSO larger than 30% when the source is intrinsically unpolarized has the probability of less than 1/100 cases. Measuring $p_{obs} \geq 35\%$ in years 2009 and 2012 when the source is not intrinsically polarized is probable in $\sim 10/100$ cases. In 2011, the p_{obs} distribution is broadened by the low S/N , therefore, the intrinsic polarization degree cannot be obtained in this data set. In all of the null hypothesis tests, since the intrinsic polarization degree was set to zero, the observed polarization angle ϕ_{obs} can be any value between -90° and 90° .

The polarization degree of the DSO is statistically significant in 2008 with significance level of 0.99, and in 2009 and 2012 with significance level of 0.9. Therefore, we detect the DSO polarization to be intrinsic in 2008, 2009, and 2012.

4.4 Discussion

The DSO is an intrinsically polarized source, since its measured polarization degree is significantly higher than the foreground polarization (6.1% in K_s -band) in different observing years. The most probable processes to produce the intrinsic polarization are (Mie-)scattering on dust grains in the dusty stellar envelopes and emission/absorption from elongated grains that are aligned magnetically. Emission and absorption processes in the NIR can happen at the same time and cancel each other. When scattering on the spherical dust grains occurs, the part of light which is scattered perpendicular to the direction of incident light which creates linear polarization and the part of the light which is scattered forward is not polarized. If a central star is enshrouded in an isotropic shell of spherical grains, the overall polarization is zero since the polarization vectors produced by the scattered light are tangential to concentric circles about the central star.

Polarization patterns can be more complicated for more complicated geometries such as YSOs that have dusty disks around the central source (see e.g. Murakawa, 2010),

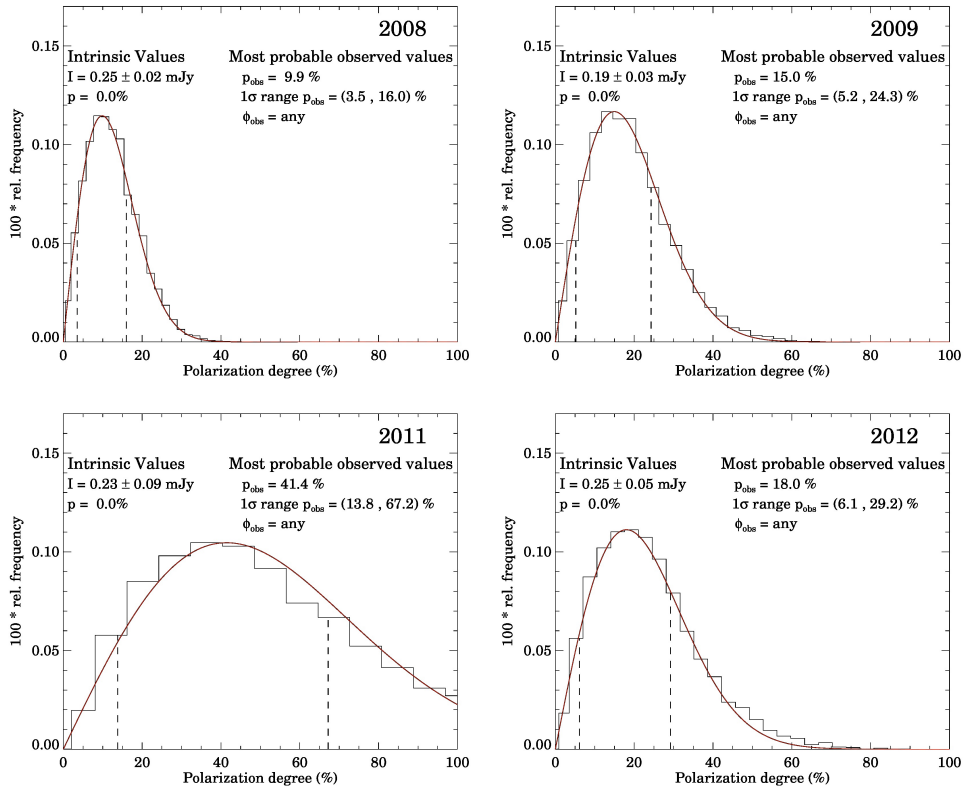


Figure 4.8: Distribution of polarization degree obtained during 2008, 2009, 2011, and 2012 with taking into account the null hypothesis ($p = 0\%$, $\phi = 0^\circ$), the observed flux density I , and its uncertainty. The mode of each distributions is the most probable observed polarization degree, p_{obs} . The 68% of the most probable observed values, $1\sigma p_{\text{obs}}$ is displayed with vertical dashed lines. The best-fit Rice function is shown in the line. Credit: [Shahzamanian et al. \(2016\)](#), reproduced with permission ©ESO.

and bow shock sources. Scattering can also happen on elongated and non-spherical dust grains and has been modeled (see e.g. [Whitney and Wolff, 2002](#)). All in all, polarization produced by light scattering depends on the source viewing angle and its geometry. Since the measured polarization degree of the DSO that I obtain is high ($p > 30\%$), it can be caused by non-spherical geometry, e.g. a bow shock. In general, if the DSO is moving through the hot, X-ray emitting region of interstellar medium with a supersonic velocity, a bow shock can form. Collisional ionization and high densities in the shocked layer of the stellar wind can generate its observed emission lines ([Scoville and Burkert, 2013](#)). The varying polarization angle obtained during the years can be explained from the combination of the source motion and the interaction with the surrounding medium, i.e. the direction of polarization vector changes from its expected direction, perpendicular to the direction of motion, due to its passage in an inhomogeneous medium. A density profile of the central region based on X-ray data suggested in [Shcherbakov and Baganoff \(2010\)](#) can indicate that the particle density increases within several arcseconds from the BH, which may cause the variation of the polarization angle in our data.

[Scoville and Burkert \(2013\)](#) suggest that the DSO is a T Tauri star that was formed in the young stellar ring and then inserted to its current orbit. They propose that a very dense bow shock is produced for the T Tauri star wind and model it numerically. [Valencia-S. et al. \(2015\)](#) also discuss that the bright observed Br γ emission of the DSO with large line width is the result of infalling material shaping a disk around the central star which can be a T Tauri star with the age of $\sim 10^5$ yrs. T Tauris generally show an intrinsic polarization, and scattering by dust grains in circumstellar shells is one of the main origins of their polarization (see e.g. [Yudin and Evans, 1998](#)). They show variations in polarization degree and angle in polarimetric images ([Appenzeller and Mundt, 1989](#)). Since the circumstellar magnetic fields of many T Tauri stars are globally ordered and powerful, these stars have magnetospheric accretion flows which are large-scale accretion flows ([Symington et al., 2005](#)).

Some of the circumstellar disks of the low mass stars have bow-shock appearance like the proplyds (protoplanetary disks) of the Orion Nebula Cluster ([O'dell and Wen, 1994](#); [Johnstone et al., 1998](#); [Störzer and Hollenbach, 1999](#)). The disk parameters of the proplyds can be constrained by NIR polarimetry even if the disk structure itself is not resolvable ([Rost et al., 2008](#)). I cannot spatially resolve a bow-shock structure or a disk since with the current angular resolution of 8 m class telescopes in K_s -band, the source appears as a point source. It might be similar to the bow-shock sources within the inner $5''$ at the GC, X3 and X7 ([Mužić et al., 2010](#)). Furthermore, it is not possible to calculate the polarization in individual regions as the source is not extended unlike IRS8 which is studied in [Rauch et al. \(2013\)](#).

Assuming DSO has a bow-shock structure, a comprehensive model of bow shock polarization using our results can enable us to analyze the influence of different polarization scenarios (emission, scattering, and dichroic extinction) that play a role in intrinsic polarization of a bow shock.

I will summarize the main results of the NIR polarimetry of the DSO in Chapter 5 and a complete analysis of the DSO polarization is presented in [Shahzamanian *et al.* \(2016\)](#).

SUMMARY AND CONCLUSION

In this thesis I first analyze the NIR polarization of Sgr A* at the center of the Milky Way, to constrain its properties. The polarized NIR light curves are obtained with NACO at the ESO VLT. Both the strong variability in the NIR and the steep spectral index (Bremer *et al.*, 2011, and references therein) show that we most probably deal with optically thin synchrotron radiation (Eckart *et al.*, 2012a). Thus, we can interpret all properties obtained based on the observation of variable polarized NIR radiation as source intrinsic properties.

The main results of the K_s -band NIR polarimetry of Sgr A* can be summarized in the following points:

- The expected uncertainties of the polarization angle and degree of Sgr A* are estimated for the measured range of flux densities. Based on these expectation, Sgr A* presents intrinsic variability in polarization angle and degree for flux densities >2 mJy. The polarization angle and degree are dominated by measuring uncertainties for low flare fluxes.
- I obtain a range of polarization degrees of 10-30%, for flare flux densities above 5 mJy. If optically thin synchrotron radiation causes the variable polarized flux density of Sgr A*, this may show depolarization because of a spatially unresolved complex source

structure.

- I find that for low flux densities the angle is affected by measurement uncertainties, while for high flux density values the angle is intrinsically variable. There is a preferred variable polarization angle of $13^\circ \pm 15^\circ$. I measure the intrinsic variability of Sgr A* on the order of 10° after correcting for the measuring uncertainties. The angle may be related to the corresponding orientation of a temporary accretion disk or jet/wind directions.

- Polarized flux density distribution is the combination of the flare activity populations with different flux densities, but a nearly constant polarization angle and a defined range of polarization degrees that vary between 10% to 30%. I find a power-law slope of ~ 4 for the polarized flux density distribution which is very close to the slope in distribution of the total flux densities found by [Witzel *et al.* \(2012\)](#).

The number density power-law slope of 4 and the well defined preferred ranges in polarization degree and angle indicate that over the past 8 years the accretion process and geometry of Sgr A* system have been rather stable. Further progress in estimating in particular the faint polarization states of Sgr A* in the NIR will need higher angular resolution with telescopes like the European Extremely Large Telescope (E-ELT) or NIR interferometers like GRAVITY at the VLTI, to better distinguish Sgr A* against background contamination. It is also interesting to assess the apparent stability of the underlying geometrical structure of the Sgr A* system by testing the well defined NIR polarization properties of it, and study the variations of this stability to understand the interaction of SBMH at center of Milky Way with its immediate environment.

In the second part of the thesis, I present the analysis of the NIR polarized observations of a Dusty S-cluster Object (DSO/G2) on an eccentric orbit around Sgr A*. The polarized data set includes the polarization information of the DSO before its pericenter passage (May 2014). The source does not show a flux density variability during the observation years, between 2008 to 2012, and its polarization degree is mainly above 20%, which is larger than the foreground polarization. The polarization angle changes as it approaches the position of Sgr A*. The polarization measurements of the DSO are significant based on our significance analysis and can be interpreted as source intrinsic properties. One of the scenarios put forward to explain the nature of the DSO is that the source develops a bow-shock structure when passing through the ambient medium ([Scoville and Burkert, 2013](#)). The obtained polarization properties of the DSO in this work can be caused by the non-spherical geometry of a bow shock. The varying polar-

ization angle can be due to the source movement in an inhomogeneous ambient medium.

The stable accretion flow onto Sgr A* can be effected by the close fly-by of the DSO, or similar dusty sources, depending on the nature of these objects. However, the DSO remained compact and its orbit Keplerian, after the pericenter passage of it (Witzel *et al.*, 2014; Valencia-S. *et al.*, 2015; Pfuhl *et al.*, 2015). Therefore, it did not lose a huge amount of angular momentum and energy during its closest approach to Sgr A* and encountered weak interactions with the SMBH (Park *et al.*, 2015). However, it may take them several years to interact and to see a variation in the activity of Sgr A* (Burkert *et al.*, 2012; Schartmann *et al.*, 2012), either in the appearing of jets (Yuan and Narayan, 2014) or as an increase in the accretion flow rate. All in all, variability and polarization measurements of Sgr A* are required to be continued as they are the optimal tools to investigate any variation in the apparently stable system due to the DSO fly-by. Moreover, future NIR polarized observations of the DSO, i.e. after the pericenter passage, allow us to better constrain the structure and polarization of the source.

A.1 Polarized flux density statistics

Here we provide additional plots similar to the ones shown in Sect. 3.3, showing the principal results from the analysis of Sgr A* observations taken in the polarization mode (NACO), but using the entire data set without limitation to the only significant values. Comparison between the figures in Sect. 3.3 and those shown here allows the reader to get an impression of the effect of selecting the most significant values for the analysis presented.

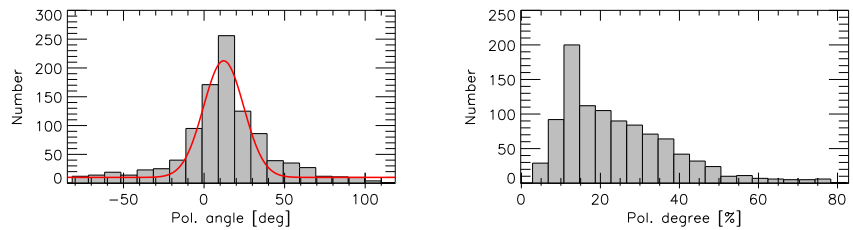


Figure A.1: Left: Distribution of K_s -band polarization angles of Sgr A* for the entire data set. The red line shows the fit with a Gaussian distribution. Right: Distribution of K_s -band polarization degrees of Sgr A* for the entire data set. Credit: *Shahzamanian et al. (2015)*, reproduced with permission ©ESO.

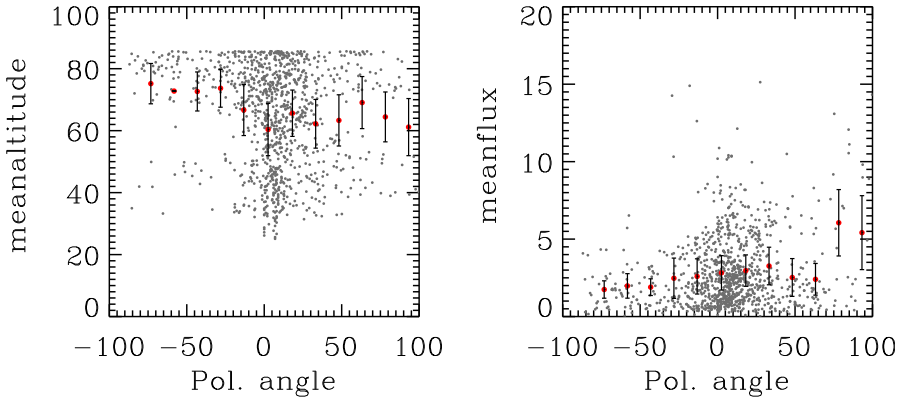


Figure A.2: Left: Altitude (elevation) of Sgr A* as a function of polarization angle as derived from all data; Right: Total flux density as a function of polarization angle; The bin width in polarization angle is 15° . The values for individual measurements are shown as black dots. The mean values per bin are shown as red dots with error bars indicating the standard deviation, if the number of data points per bin is larger than 2. Credit: [Shahzamanian et al. \(2015\)](#), reproduced with permission ©ESO.

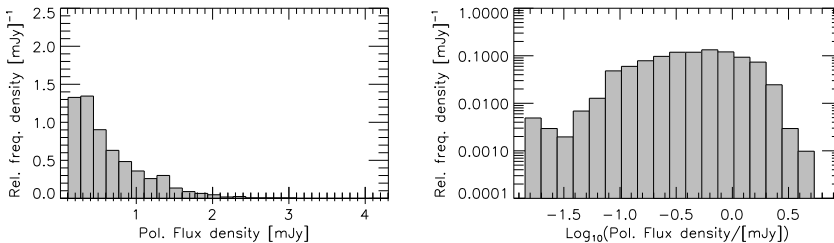


Figure A.3: Left: Distribution of the polarized flux density for the whole data set after correction for stellar contamination. Right: the same plot in logarithmic scale. Credit: [Shahzamanian et al. \(2015\)](#), reproduced with permission ©ESO.

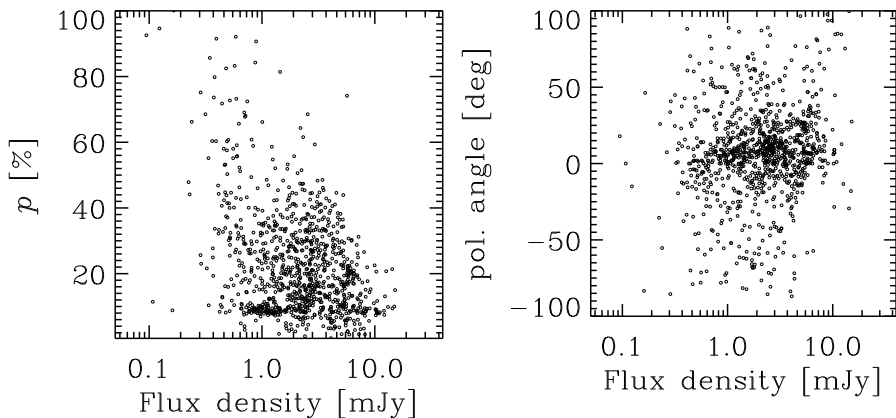


Figure A.4: Left: Total flux density and degree of polarization relation for the entire data after correction for the stellar contamination. Right: Total flux density and angle of polarization relation for the entire data after correction for the stellar contamination. Credit: [Shahzamanian et al. \(2015\)](#), reproduced with permission ©ESO.

A.2 Maximum Likelihood Estimation

Maximum likelihood method uses the probability density function likelihood, which is a function of the data given values of the model parameters. For describing this function and the method I use the notification of [Wall and Jenkins \(2012\)](#). The likelihood L for a probability density $f(X; \theta)$ with parameter θ and random variables X_1, X_2, \dots, X_n is a product of densities estimated at all the variables:

$$L(\theta) = \prod_{i=1}^N f(X_i; \theta) . \quad (\text{A.1})$$

. It is usually more convenient numerically to work with loglikelihood l rather than likelihood L ,

$$l(\theta) = \sum_{i=1}^N \ln f(X_i; \theta), \quad (\text{A.2})$$

The peak value of likelihood is the best estimate for θ . Formally, The maximum likelihood estimator of θ can be found by maximizing the $l(\theta)$ for all variations of θ .

A.3 Bootstrap

I describe here the bootstrap method that I have used in this dissertation for obtaining the uncertainty on the determined values of parameters from the fitting process. This method was presented by [Efron \(1982\)](#) for the first time. By considering all our data points, I estimate the parameters values of our models or fittings. In order to obtain the error on the estimated parameters, we should do the following. First we assign a label to each data point: a_1, a_2, \dots, a_N , i.e. N is the number of the data points. Then we add a Gaussian random-number generator, with the mean value of zero and the width of average error of all the data points, to all the data points and we calculate the parameter values again. Subsequently, we repeat the steps mentioned for a large number of time. The uncertainty of the estimated parameter value is the standard deviation of the obtained parameter distribution.

BIBLIOGRAPHY

- Abarca, D., Sądowski, A., and Sironi, L. (2014). Simulating the effect of the Sgr A* accretion flow on the appearance of G2 after pericentre. *MNRAS*, **440**, 1125–1137.
- Antonucci, R. R. J. (1982). Optical polarization position angle versus radio source axis in radio galaxies. *Nature*, **299**, 605.
- Appenzeller, I. and Mundt, R. (1989). T Tauri stars. *A&A Rev.*, **1**, 291–334.
- Backer, D. C. and Sramek, R. A. (1999). Proper Motion of the Compact, Nonthermal Radio Source in the Galactic Center, Sagittarius A*. *ApJ*, **524**, 805–815.
- Baganoff, F. K., Bautz, M. W., Brandt, W. N., Chartas, G., Feigelson, E. D., Garmire, G. P., Maeda, Y., Morris, M., Ricker, G. R., Townsley, L. K., and Walter, F. (2001). Rapid X-ray flaring from the direction of the supermassive black hole at the Galactic Centre. *Nature*, **413**, 45–48.
- Baganoff, F. K., Maeda, Y., Morris, M., Bautz, M. W., Brandt, W. N., Cui, W., Doty, J. P., Feigelson, E. D., Garmire, G. P., Pravdo, S. H., Ricker, G. R., and Townsley, L. K. (2003). Chandra X-Ray Spectroscopic Imaging of Sagittarius A* and the Central Parsec of the Galaxy. *ApJ*, **591**, 891–915.
- Bailey, J., Hough, J. H., and Axon, D. J. (1984). Imaging and polarimetry of the galactic centre in the near-infrared. *MNRAS*, **208**, 661–671.
- Balbus, S. A. and Hawley, J. F. (1991). A powerful local shear instability in weakly magnetized disks. I - Linear analysis. II - Nonlinear evolution. *ApJ*, **376**, 214–233.
- Ballone, A., Schartmann, M., Burkert, A., Gillessen, S., Genzel, R., Fritz, T. K., Eisenhauer, F., Pfuhl, O., and Ott, T. (2013). Hydrodynamical Simulations of a Compact Source Scenario for the Galactic Center Cloud G2. *ApJ*, **776**, 13.
- Blandford, R. D. and Znajek, R. L. (1977). Electromagnetic extraction of energy from Kerr black holes. *MNRAS*, **179**, 433–456.

- Bower, G. C., Falcke, H., and Backer, D. C. (1999a). Detection of Circular Polarization in the Galactic Center Black Hole Candidate Sagittarius A*. *ApJ*, **523**, L29–L32.
- Bower, G. C., Backer, D. C., Zhao, J.-H., Goss, M., and Falcke, H. (1999b). The Linear Polarization of Sagittarius A*. I. VLA Spectropolarimetry at 4.8 and 8.4 GHz. *ApJ*, **521**, 582–586.
- Bower, G. C., Wright, M. C. H., Falcke, H., and Backer, D. C. (2001). BIMA Observations of Linear Polarization in Sagittarius A* at 112 GHz. *ApJ*, **555**, L103–L106.
- Bower, G. C., Wright, M. C. H., Falcke, H., and Backer, D. C. (2003). Interferometric Detection of Linear Polarization from Sagittarius A* at 230 GHz. *ApJ*, **588**, 331–337.
- Bower, G. C., Goss, W. M., Falcke, H., Backer, D. C., and Lithwick, Y. (2006). The Intrinsic Size of Sagittarius A* from 0.35 to 6 cm. *ApJ*, **648**, L127–L130.
- Bower, G. C., Markoff, S., Brunthaler, A., Law, C., Falcke, H., Maitra, D., Clavel, M., Goldwurm, A., Morris, M. R., Witzel, G., Meyer, L., and Ghez, A. M. (2014). The Intrinsic Two-dimensional Size of Sagittarius A*. *ApJ*, **790**, 1.
- Brandner, W., Rousset, G., Lenzen, R., Hubin, N., Lacombe, F., Hofmann, R., Moorwood, A., Lagrange, A.-M., Gendron, E., Hartung, M., Puget, P., Ageorges, N., Biereichel, P., Bouy, H., Charton, J., Dumont, G., Fusco, T., Jung, Y., Lehnert, M., Lizon, J.-L., Monnet, G., Mouillet, D., Moutou, C., Rabaud, D., Röhrle, C., Skole, S., Spyromilio, J., Storz, C., Tacconi-Garman, L., and Zins, G. (2002). NAOS+CONICA at YEPUN: first VLT adaptive optics system sees first light. *The Messenger*, **107**, 1–6.
- Bremer, M., Witzel, G., Eckart, A., Zamaninasab, M., Buchholz, R. M., Schödel, R., Straubmeier, C., García-Marín, M., and Duschl, W. (2011). The near-infrared spectral index of Sagittarius A* derived from Ks- and H-band flare statistics. *A&A*, **532**, A26.
- Broderick, A. E. and Loeb, A. (2006). Imaging optically-thin hotspots near the black hole horizon of Sgr A* at radio and near-infrared wavelengths. *MNRAS*, **367**, 905–916.
- Broderick, A. E., Loeb, A., and Narayan, R. (2009). The Event Horizon of Sagittarius A*. *ApJ*, **701**, 1357–1366.
- Buchholz, R. M., Witzel, G., Schödel, R., Eckart, A., Bremer, M., and Mužić, K. (2011). Adaptive-optics assisted near-infrared polarization measurements of sources in the Galactic center. *A&A*, **534**, A117.
- Buchholz, R. M., Witzel, G., Schödel, R., and Eckart, A. (2013). Ks- and Lp-band polarimetry on stellar and bow-shock sources in the Galactic center. *A&A*, **557**, A82.
- Burkert, A., Schartmann, M., Alig, C., Gillessen, S., Genzel, R., Fritz, T. K., and Eisenhauer, F. (2012). Physics of the Galactic Center Cloud G2, on Its Way toward the Supermassive Black Hole. *ApJ*, **750**, 58.

- Capelli, R., Warwick, R. S., Porquet, D., Gillessen, S., and Predehl, P. (2012). The X-ray lightcurve of Sagittarius A* over the past 150 years inferred from Fe-K α line reverberation in Galactic centre molecular clouds. *A&A*, **545**, A35.
- Chan, C.-k., Liu, S., Fryer, C. L., Psaltis, D., Özel, E., Rockefeller, G., and Melia, F. (2009). MHD Simulations of Accretion onto Sgr A*: Quiescent Fluctuations, Outbursts, and Quasiperiodicity. *ApJ*, **701**, 521–534.
- Christopher, M. H., Scoville, N. Z., Stolovy, S. R., and Yun, M. S. (2005). HCN and HCO⁺ Observations of the Galactic Circumnuclear Disk. *ApJ*, **622**, 346–365.
- Clarke, D. (2010). *Stellar Polarimetry*.
- Clauset, A., Rohilla Shalizi, C., and Newman, M. E. J. (2007). Power-law distributions in empirical data. *ArXiv e-prints*.
- Coker, R. F. and Melia, F. (1997). Hydrodynamical Accretion onto Sagittarius A* from Distributed Point Sources. *ApJ*, **488**, L149–L152.
- Contini, M. (2011). The low-luminosity active galactic nucleus in the centre of the Galaxy. *MNRAS*, **418**, 1935–1947.
- Cuadra, J., Nayakshin, S., Springel, V., and Di Matteo, T. (2005). Accretion of cool stellar winds on to Sgr A*: another puzzle of the Galactic Centre? *MNRAS*, **360**, L55–L59.
- Cuadra, J., Nayakshin, S., Springel, V., and Di Matteo, T. (2006). Galactic Centre stellar winds and Sgr A* accretion. *MNRAS*, **366**, 358–372.
- Cuadra, J., Nayakshin, S., and Martins, F. (2008). Variable accretion and emission from the stellar winds in the Galactic Centre. *MNRAS*, **383**, 458–466.
- Degenaar, N., Reynolds, M. T., Miller, J. M., Kennea, J. A., and Wijnands, R. (2013). Large Flare from Sgr A* Detected by Swift. *The Astronomer's Telegram*, **5006**, 1.
- Devillard, N. (1999). Infrared Jitter Imaging Data Reduction: Algorithms and Implementation. In D. M. Mehringer, R. L. Plante, and D. A. Roberts, editors, *Astronomical Data Analysis Software and Systems VIII*, volume 172 of *Astronomical Society of the Pacific Conference Series*, page 333.
- Dexter, J., McKinney, J. C., Markoff, S., and Tchekhovskoy, A. (2014). Transient jet formation and state transitions from large-scale magnetic reconnection in black hole accretion discs. *MNRAS*, **440**, 2185–2190.
- Diolaiti, E., Bendinelli, O., Bonaccini, D., Close, L., Currie, D., and Parmeggiani, G. (2000). Analysis of isoplanatic high resolution stellar fields by the StarFinder code. *A&AS*, **147**, 335–346.

- Do, T., Ghez, A. M., Morris, M. R., Yelda, S., Meyer, L., Lu, J. R., Hornstein, S. D., and Matthews, K. (2009). A Near-Infrared Variability Study of the Galactic Black Hole: A Red Noise Source with NO Detected Periodicity. *ApJ*, **691**, 1021–1034.
- Dodds-Eden, K., Porquet, D., Trap, G., Quataert, E., Haubois, X., Gillessen, S., Grosso, N., Pantin, E., Falcke, H., Rouan, D., Genzel, R., Hasinger, G., Goldwurm, A., Yusef-Zadeh, F., Clenet, Y., Trippe, S., Lagage, P., Bartko, H., Eisenhauer, F., Ott, T., Paumard, T., Perrin, G., Yuan, F., Fritz, T. K., and Mascetti, L. (2009). Evidence for X-Ray Synchrotron Emission from Simultaneous Mid-Infrared to X-Ray Observations of a Strong Sgr A* Flare. *ApJ*, **698**, 676–692.
- Dodds-Eden, K., Gillessen, S., Fritz, T. K., Eisenhauer, F., Trippe, S., Genzel, R., Ott, T., Bartko, H., Pfuhl, O., Bower, G., Goldwurm, A., Porquet, D., Trap, G., and Yusef-Zadeh, F. (2011). The Two States of Sgr A* in the Near-infrared: Bright Episodic Flares on Top of Low-level Continuous Variability. *ApJ*, **728**, 37–+.
- Doi, K. (1978). Physical reality of shot noise model for the short-term variability of CYG X-1. *Nature*, **275**, 197.
- Dovčiak, M., Karas, V., and Yaqoob, T. (2004). An Extended Scheme for Fitting X-Ray Data with Accretion Disk Spectra in the Strong Gravity Regime. *ApJS*, **153**, 205–221.
- Dovčiak, M., Karas, V., Matt, G., and Goosmann, R. W. (2008). Variation in the primary and reprocessed radiation from an orbiting spot around a black hole. *MNRAS*, **384**, 361–369.
- Eckart, A. and Genzel, R. (1996). Observations of stellar proper motions near the Galactic Centre. *Nature*, **383**, 415–417.
- Eckart, A. and Genzel, R. (1997). Stellar proper motions in the central 0.1 PC of the Galaxy. *MNRAS*, **284**, 576–598.
- Eckart, A., Genzel, R., Hofmann, R., Sams, B. J., and Tacconi-Garman, L. E. (1995). High angular resolution spectroscopic and polarimetric imaging of the galactic center in the near-infrared. *ApJ*, **445**, L23–L26.
- Eckart, A., Ott, T., and Genzel, R. (1999). The Sgr A* stellar cluster: New NIR imaging and spectroscopy. *A&A*, **352**, L22–L25.
- Eckart, A., Genzel, R., Ott, T., and Schödel, R. (2002). Stellar orbits near Sagittarius A*. *MNRAS*, **331**, 917–934.
- Eckart, A., Baganoff, F. K., Morris, M., Bautz, M. W., Brandt, W. N., Garmire, G. P., Genzel, R., Ott, T., Ricker, G. R., Straubmeier, C., Viehmann, T., Schödel, R., Bower, G. C., and Goldston, J. E. (2004). First simultaneous NIR/X-ray detection of a flare from Sgr A*. *A&A*, **427**, 1–11.

- Eckart, A., Schödel, R., and Straubmeier, C. (2005). *The black hole at the center of the Milky Way*. London:Imperial College Press ; Hackensack, NJ : Distributed by World Scientific Pub. Co., c2005.
- Eckart, A., Schödel, R., Meyer, L., Trippe, S., Ott, T., Genzel, R., Muzic, K., Moulataka, J., Straubmeier, C., Baganoff, F. K., Morris, M., and Bower, G. C. (2006a). Multi-wavelength and polarimetric observations of Sagittarius A*. *Journal of Physics Conference Series*, **54**, 391–398.
- Eckart, A., Schödel, R., Meyer, L., Trippe, S., Ott, T., and Genzel, R. (2006b). Polarimetry of near-infrared flares from Sagittarius A*. *A&A*, **455**, 1–10.
- Eckart, A., Schödel, R., Meyer, L., Trippe, S., Ott, T., and Genzel, R. (2006c). Polarimetry of near-infrared flares from Sagittarius A*. *A&A*, **455**, 1–10.
- Eckart, A., Baganoff, F. K., Schödel, R., Morris, M., Genzel, R., Bower, G. C., Marrone, D., Moran, J. M., Viehmann, T., Bautz, M. W., Brandt, W. N., Garmire, G. P., Ott, T., Trippe, S., Ricker, G. R., Straubmeier, C., Roberts, D. A., Yusef-Zadeh, F., Zhao, J. H., and Rao, R. (2006d). The flare activity of Sagittarius A*. New coordinated mm to X-ray observations. *A&A*, **450**, 535–555.
- Eckart, A., Baganoff, F. K., Zamaninasab, M., Morris, M. R., Schödel, R., Meyer, L., Muzic, K., Bautz, M. W., Brandt, W. N., Garmire, G. P., Ricker, G. R., Kunneriath, D., Straubmeier, C., Duschl, W., Dovciak, M., Karas, V., Markoff, S., Najarro, F., Mauerhan, J., Moulataka, J., and Zensus, A. (2008a). Polarized NIR and X-ray flares from Sagittarius A*. *A&A*, **479**, 625–639.
- Eckart, A., Schödel, R., García-Marín, M., Witzel, G., Weiss, A., Baganoff, F. K., Morris, M. R., Bertram, T., Dovciak, M., Duschl, W. J., Karas, V., König, S., Krichbaum, T. P., Krips, M., Kunneriath, D., Lu, R., Markoff, S., Mauerhan, J., Meyer, L., Moulataka, J., Mužić, K., Najarro, F., Pott, J., Schuster, K. F., Sjouwerman, L. O., Straubmeier, C., Thum, C., Vogel, S. N., Wiesemeyer, H., Zamaninasab, M., and Zensus, J. A. (2008b). Simultaneous NIR/sub-mm observation of flare emission from Sagittarius A*. *A&A*, **492**, 337–344.
- Eckart, A., Schödel, R., García-Marín, M., Witzel, G., Weiss, A., Baganoff, F. K., Morris, M. R., Bertram, T., Dovciak, M., Duschl, W. J., Karas, V., König, S., Krichbaum, T. P., Krips, M., Kunneriath, D., Lu, R.-S., Markoff, S., Mauerhan, J., Meyer, L., Moulataka, J., Mužić, K., Najarro, F., Pott, J.-U., Schuster, K. F., Sjouwerman, L. O., Straubmeier, C., Thum, C., Vogel, S. N., Wiesemeyer, H., Zamaninasab, M., and Zensus, J. A. (2008c). Simultaneous NIR/sub-mm observation of flare emission from Sagittarius A*. *A&A*, **492**, 337–344.
- Eckart, A., García-Marín, M., Vogel, S. N., Teuben, P., Morris, M. R., Baganoff, F., Dexter, J., Schödel, R., Witzel, G., Valencia-S, M., Karas, V., Kunneriath, D., Bremer, M., Straubmeier, C., Moser, L., Sabha, N., Buchholz, R., Zamaninasab, M., Mužić, K., Moulataka, J.,

- and Zensus, J. A. (2012a). Flare emission from Sagittarius A*. *Journal of Physics Conference Series*, **372**(1), 012022.
- Eckart, A., Britzen, S., Horrobin, M., Zamaninasab, M., Muzic, K., Sabha, N., Shahzamanian, B., Yazici, S., Moser, L., Zuther, J., Garcia-Marin, M., Valencia-S., M., Bursa, M., Karssen, G., Karas, V., Jalali, B., Vitale, M., Bremer, M., Fischer, S., Smajic, S., Rauch, C., Kunneriath, D., Moulataka, J., Straubmeier, C., Rashed, Y. E., Iserlohe, C., Busch, G., Markakis, K., Borkar, A., and Zensus, A. J. (2012b). The Galactic Center as a paradigm for low-luminosity nuclei? What can be learned from SgrA* for the central engine and conditions of star formation in nuclei of Seyfert galaxies and low luminosity nearby QSOs; The K-band identification of the DSO/G2 source from VLT and Keck data. In *Proceedings of Nuclei of Seyfert galaxies and QSOs - Central engine & conditions of star formation (Seyfert 2012). 6-8 November, 2012. Max-Planck-Institut für Radioastronomie (MPIfR), Bonn, Germany.*, page 4.
- Eckart, A., Mužić, K., Yazici, S., Sabha, N., Shahzamanian, B., Witzel, G., Moser, L., Garcia-Marin, M., Valencia-S., M., Jalali, B., Bremer, M., Straubmeier, C., Rauch, C., Buchholz, R., Kunneriath, D., and Moulataka, J. (2013). Near-infrared proper motions and spectroscopy of infrared excess sources at the Galactic center. *A&A*, **551**, A18.
- Eckart, A., Horrobin, M., Britzen, S., Zamaninasab, M., Mužić, K., Sabha, N., Shahzamanian, B., Yazici, S., Moser, L., Garcia-Marin, M., Valencia-S., M., Borkar, A., Bursa, M., Karssen, G., Karas, V., Zajaček, M., Bronfman, L., Finger, R., Jalali, B., Vitale, M., Rauch, C., Kunneriath, D., Moulataka, J., Straubmeier, C., Rashed, Y. E., Markakis, K., and Zensus, A. (2014). The infrared K-band identification of the DSO/G2 source from VLT and Keck data. In L. O. Sjouwerman, C. C. Lang, and J. Ott, editors, *IAU Symposium*, volume 303 of *IAU Symposium*, pages 269–273.
- Eckart, A., Valencia-S., M., Shahzamanian, B., Garcia-Marin, M., Peissker, F., Zajacek, M., Parsa, M., Jalali, B., Saalfeld, R., Sabha, N., Yazic, S., Karssen, G. D., Borkar, A., Markakis, K., Zensus, J. A., and Straubmeier, C. (2015). The Center of the Milky Way from Radio to X-rays. *ArXiv e-prints*.
- Efron, B. (1982). *The Jackknife, the Bootstrap and other resampling plans*.
- Eisenhauer, F., Schödel, R., Genzel, R., Ott, T., Tecza, M., Abuter, R., Eckart, A., and Alexander, T. (2003). A Geometric Determination of the Distance to the Galactic Center. *ApJ*, **597**, L121–L124.
- Eisenhauer, F., Genzel, R., Alexander, T., Abuter, R., Paumard, T., Ott, T., Gilbert, A., Gillessen, S., Horrobin, M., Trippe, S., Bonnet, H., Dumas, C., Hubin, N., Kaufer, A., Kissler-Patig, M., Monnet, G., Ströbele, S., Szeifert, T., Eckart, A., Schödel, R., and Zucker, S. (2005). SINFONI in the Galactic Center: Young Stars and Infrared Flares in the Central Light-Month. *ApJ*, **628**, 246–259.

- Eisenhauer, F., Perrin, G., Brandner, W., Straubmeier, C., Richichi, A., Gillessen, S., Berger, J. P., Hippler, S., Eckart, A., Schöller, M., Rabiën, S., Cassaing, F., Lenzen, R., Thiel, M., Clénet, Y., Ramos, J. R., Kellner, S., Fédou, P., Baumeister, H., Hofmann, R., Gendron, E., Boehm, A., Bartko, H., Haubois, X., Klein, R., Dodds-Eden, K., Houairi, K., Hormuth, E., Gräter, A., Jocou, L., Naranjo, V., Genzel, R., Kervella, P., Henning, T., Hamaus, N., Lacour, S., Neumann, U., Haug, M., Malbet, F., Laun, W., Kolmeder, J., Paumard, T., Rohloff, R., Pfuhl, O., Perraut, K., Ziegler, J., Rouan, D., and Rousset, G. (2008). GRAVITY: getting to the event horizon of Sgr A*. In *Society of Photo-Optical Instrumentation Engineers (SPIE) Conference Series*, volume 7013 of *Society of Photo-Optical Instrumentation Engineers (SPIE) Conference Series*.
- Ekers, R. D., Goss, W. M., Schwarz, U. J., Downes, D., and Rogstad, D. H. (1975). A full synthesis map of Sgr A at 5 GHz. *A&A*, **43**, 159–166.
- Ekers, R. D., van Gorkom, J. H., Schwarz, U. J., and Goss, W. M. (1983). The radio structure of SGR A. *A&A*, **122**, 143–150.
- Falcke, H. and Markoff, S. (2000). The jet model for Sgr A*: Radio and X-ray spectrum. *A&A*, **362**, 113–118.
- Falcke, H., Goss, W. M., Matsuo, H., Teuben, P., Zhao, J., and Zylka, R. (1998). The Simultaneous Spectrum of Sagittarius A * from 20 Centimeters to 1 Millimeter and the Nature of the Millimeter Excess. *ApJ*, **499**, 731–+.
- Fried, D. L. (1996). Artificial guide star tilt-anisoplanatism: its magnitude and amelioration. In M. Cullum, editor, *European Southern Observatory Conference and Workshop Proceedings*, volume 54 of *European Southern Observatory Conference and Workshop Proceedings*, page 363.
- Fritz, T., Gillessen, S., Trippe, S., Ott, T., Bartko, H., Pfuhl, O., Dodds-Eden, K., Davies, R., Eisenhauer, F., and Genzel, R. (2010). What is limiting near-infrared astrometry in the Galactic Centre? *MNRAS*, **401**, 1177–1188.
- Gabuzda, D. C., Pushkarev, A. B., and Cawthorne, T. V. (2000). Analysis of $\lambda=6\text{cm}$ VLBI polarization observations of a complete sample of northern BL Lacertae objects. *MNRAS*, **319**, 1109–1124.
- Genzel, R., Crawford, M. K., Townes, C. H., and Watson, D. M. (1985). The neutral-gas disk around the galactic center. *ApJ*, **297**, 766–786.
- Genzel, R., Thatte, N., Krabbe, A., Kroker, H., and Tacconi-Garman, L. E. (1996). The Dark Mass Concentration in the Central Parsec of the Milky Way. *ApJ*, **472**, 153–+.
- Genzel, R., Schödel, R., Ott, T., Eckart, A., Alexander, T., Lacombe, F., Rouan, D., and Aschenbach, B. (2003). Near-infrared flares from accreting gas around the supermassive black hole at the Galactic Centre. *Nature*, **425**, 934–937.

- Genzel, R., Eisenhauer, F., and Gillessen, S. (2010). The Galactic Center massive black hole and nuclear star cluster. *Reviews of Modern Physics*, **82**, 3121–3195.
- Ghez, A. M., Klein, B. L., Morris, M., and Becklin, E. E. (1998). High Proper-Motion Stars in the Vicinity of Sagittarius A*: Evidence for a Supermassive Black Hole at the Center of Our Galaxy. *ApJ*, **509**, 678–686.
- Ghez, A. M., Morris, M., Becklin, E. E., Tanner, A., and Kremenek, T. (2000). The accelerations of stars orbiting the Milky Way’s central black hole. *Nature*, **407**, 349–351.
- Ghez, A. M., Duchêne, G., Matthews, K., Hornstein, S. D., Tanner, A., Larkin, J., Morris, M., Becklin, E. E., Salim, S., Kremenek, T., Thompson, D., Soifer, B. T., Neugebauer, G., and McLean, I. (2003). The First Measurement of Spectral Lines in a Short-Period Star Bound to the Galaxy’s Central Black Hole: A Paradox of Youth. *ApJ*, **586**, L127–L131.
- Ghez, A. M., Salim, S., Hornstein, S. D., Tanner, A., Lu, J. R., Morris, M., Becklin, E. E., and Duchêne, G. (2005a). Stellar Orbits around the Galactic Center Black Hole. *ApJ*, **620**, 744–757.
- Ghez, A. M., Hornstein, S. D., Lu, J. R., Bouchez, A., Le Mignant, D., van Dam, M. A., Wizinowich, P., Matthews, K., Morris, M., Becklin, E. E., Campbell, R. D., Chin, J. C. Y., Hartman, S. K., Johansson, E. M., Lafon, R. E., Stomski, P. J., and Summers, D. M. (2005b). The First Laser Guide Star Adaptive Optics Observations of the Galactic Center: Sgr A*’s Infrared Color and the Extended Red Emission in its Vicinity. *ApJ*, **635**, 1087–1094.
- Ghez, A. M., Salim, S., Weinberg, N. N., Lu, J. R., Do, T., Dunn, J. K., Matthews, K., Morris, M. R., Yelda, S., Becklin, E. E., Kremenek, T., Milosavljevic, M., and Naiman, J. (2008). Measuring Distance and Properties of the Milky Way’s Central Supermassive Black Hole with Stellar Orbits. *ApJ*, **689**, 1044–1062.
- Ghez, A. M., Witzel, G., Sitarski, B., Meyer, L., Yelda, S., Boehle, A., Becklin, E. E., Campbell, R., Canalizo, G., Do, T., Lu, J. R., Matthews, K., Morris, M. R., and Stockton, A. (2014). Detection of Galactic Center Source G2 at 3.8 micron during Periapse Passage Around the Central Black Hole. *The Astronomer’s Telegram*, **6110**, 1.
- Gillessen, S., Eisenhauer, F., Quataert, E., Genzel, R., Paumard, T., Trippe, S., Ott, T., Abuter, R., Eckart, A., Lagage, P. O., Lehnert, M. D., Tacconi, L. J., and Martins, F. (2006). Variations in the Spectral Slope of Sagittarius A* during a Near-Infrared Flare. *ApJ*, **640**, L163–L166.
- Gillessen, S., Eisenhauer, F., Trippe, S., Alexander, T., Genzel, R., Martins, F., and Ott, T. (2009a). Monitoring Stellar Orbits Around the Massive Black Hole in the Galactic Center. *ApJ*, **692**, 1075–1109.

- Gillessen, S., Eisenhauer, F., Fritz, T. K., Bartko, H., Dodds-Eden, K., Pfuhl, O., Ott, T., and Genzel, R. (2009b). The Orbit of the Star S2 Around Sgr A* from Very Large Telescope and Keck Data. *ApJ*, **707**, L114–L117.
- Gillessen, S., Genzel, R., Fritz, T. K., Quataert, E., Alig, C., Burkert, A., Cuadra, J., Eisenhauer, F., Pfuhl, O., Dodds-Eden, K., Gammie, C. E., and Ott, T. (2012). A gas cloud on its way towards the supermassive black hole at the Galactic Centre. *Nature*, **481**, 51–54.
- Gillessen, S., Genzel, R., Fritz, T. K., Eisenhauer, F., Pfuhl, O., Ott, T., Cuadra, J., Schartmann, M., and Burkert, A. (2013). New Observations of the Gas Cloud G2 in the Galactic Center. *ApJ*, **763**, 78.
- Ginzburg, V. L. and Syrovatskii, S. I. (1965). Cosmic Magnetobremstrahlung (synchrotron Radiation). *ARA&A*, **3**, 297.
- Goldston, J. E., Quataert, E., and Igumenshchev, I. V. (2005). Synchrotron Radiation from Radiatively Inefficient Accretion Flow Simulations: Applications to Sagittarius A*. *ApJ*, **621**, 785–792.
- Goosmann, R. W. and Gaskell, C. M. (2007). Modeling optical and UV polarization of AGNs. I. Imprints of individual scattering regions. *A&A*, **465**, 129–145.
- Guesten, R., Genzel, R., Wright, M. C. H., Jaffe, D. T., Stutzki, J., and Harris, A. I. (1987). Aperture synthesis observations of the circumnuclear ring in the Galactic center. *ApJ*, **318**, 124–138.
- Haggard, D., Baganoff, F. K., Ponti, G., Heinke, C. O., Rea, N., Neilsen, J., Nowak, M., Markoff, S., Degenaar, N., Yusef-Zadeh, F., Roberts, D. A., Brinkerink, C., Law, C. J., Gillessen, S., and Connors, R. (2015). An Update on Chandra/VLA Galactic Center Campaigns Targeting Sgr A* and G2. In *American Astronomical Society Meeting Abstracts*, volume 225 of *American Astronomical Society Meeting Abstracts*, page 102.09.
- Hamaus, N., Paumard, T., Müller, T., Gillessen, S., Eisenhauer, F., Trippe, S., and Genzel, R. (2009). Prospects for Testing the Nature of Sgr A*'s Near-Infrared Flares on the Basis of Current Very Large Telescope and Future Very Large Telescope Interferometer Observations. *ApJ*, **692**, 902–916.
- Herrnstein, R. M. and Ho, P. T. P. (2002). Hot Molecular Gas in the Galactic Center. *ApJ*, **579**, L83–L86.
- Hornstein, S. D., Matthews, K., Ghez, A. M., Lu, J. R., Morris, M., Becklin, E. E., Baganoff, F. K., and Rafelski, M. (2006). Infrared/X-ray intensity variations and the color of Sgr A*. *Journal of Physics Conference Series*, **54**, 399–405.

- Jalali, B., Pelupessy, F. I., Eckart, A., Portegies Zwart, S., Sabha, N., Borkar, A., Moultaqa, J., Mužić, K., and Moser, L. (2014). Star formation in the vicinity of nuclear black holes: young stellar objects close to Sgr A*. *MNRAS*, **444**, 1205–1220.
- Johnstone, D., Hollenbach, D., and Bally, J. (1998). Photoevaporation of Disks and Clumps by Nearby Massive Stars: Application to Disk Destruction in the Orion Nebula. *ApJ*, **499**, 758–776.
- Kennea, J. A., Burrows, D. N., Kouveliotou, C., Palmer, D. M., Göğüş, E., Kaneko, Y., Evans, P. A., Degenaar, N., Reynolds, M. T., Miller, J. M., Wijnands, R., Mori, K., and Gehrels, N. (2013). Swift Discovery of a New Soft Gamma Repeater, SGR J1745-29, near Sagittarius A*. *ApJ*, **770**, L24.
- Knacke, R. F. and Capps, R. W. (1977). Infrared polarization of the galactic center. II. *ApJ*, **216**, 271–276.
- Koyama, K., Maeda, Y., Sonobe, T., Takeshima, T., Tanaka, Y., and Yamauchi, S. (1996). ASCA View of Our Galactic Center: Remains of Past Activities in X-Rays? *PASJ*, **48**, 249–255.
- Krabbe, A., Genzel, R., Eckart, A., Najarro, F., Lutz, D., Cameron, M., Kroker, H., Tacconi-Garman, L. E., Thatte, N., Weitzel, L., Drapatz, S., Geballe, T., Sternberg, A., and Kudritzki, R. (1995). The Nuclear Cluster of the Milky Way: Star Formation and Velocity Dispersion in the Central 0.5 Parsec. *ApJ*, **447**, L95+.
- Lau, R. M., Herter, T. L., Morris, M. R., Becklin, E. E., and Adams, J. D. (2013). SOFIA/FORCAST Imaging of the Circumnuclear Ring at the Galactic Center. *ApJ*, **775**, 37.
- Lenzen, R., Hartung, M., Brandner, W., Finger, G., Hubin, N. N., Lacombe, F., Lagrange, A.-M., Lehnert, M. D., Moorwood, A. F. M., and Mouillet, D. (2003). NAOS-CONICA first on sky results in a variety of observing modes. In M. Iye and A. F. M. Moorwood, editors, *Instrument Design and Performance for Optical/Infrared Ground-based Telescopes*, volume 4841 of *Society of Photo-Optical Instrumentation Engineers (SPIE) Conference Series*, pages 944–952.
- Liu, S. and Melia, F. (2002). An Accretion-induced X-Ray Flare in Sagittarius A*. *ApJ*, **566**, L77–L80.
- Liu, S., Petrosian, V., and Melia, F. (2004). Electron Acceleration around the Supermassive Black Hole at the Galactic Center. *ApJ*, **611**, L101–L104.
- Liu, S., Petrosian, V., Melia, F., and Fryer, C. L. (2006). A Testable Stochastic Acceleration Model for Flares in Sagittarius A*. *ApJ*, **648**, 1020–1025.

- Lucy, L. B. (1974). An iterative technique for the rectification of observed distributions. *Astronomical Journal*, **79**, 745–+.
- Macquart, J.-P., Bower, G. C., Wright, M. C. H., Backer, D. C., and Falcke, H. (2006). The Rotation Measure and 3.5 Millimeter Polarization of Sagittarius A*. *ApJ*, **646**, L111–L114.
- Markoff, S., Falcke, H., Yuan, F., and Biermann, P. L. (2001). The Nature of the 10 kilosecond X-ray flare in Sgr A*. *A&A*, **379**, L13–L16.
- Markoff, S., Bower, G. C., and Falcke, H. (2007). How to hide large-scale outflows: size constraints on the jets of Sgr A*. *MNRAS*, **379**, 1519–1532.
- Marrone, D. P., Moran, J. M., Zhao, J., and Rao, R. (2006). Interferometric Measurements of Variable 340 GHz Linear Polarization in Sagittarius A*. *ApJ*, **640**, 308–318.
- Marrone, D. P., Moran, J. M., Zhao, J., and Rao, R. (2007). An Unambiguous Detection of Faraday Rotation in Sagittarius A*. *ApJ*, **654**, L57–L60.
- Marrone, D. P., Baganoff, F. K., Morris, M. R., Moran, J. M., Ghez, A. M., Hornstein, S. D., Dowell, C. D., Muñoz, D. J., Bautz, M. W., Ricker, G. R., Brandt, W. N., Garmire, G. P., Lu, J. R., Matthews, K., Zhao, J., Rao, R., and Bower, G. C. (2008). An X-Ray, Infrared, and Submillimeter Flare of Sagittarius A*. *ApJ*, **682**, 373–383.
- Melia, F. (1992). An accreting black hole model for Sagittarius A. *ApJ*, **387**, L25–L28.
- Melia, F. and Falcke, H. (2001). The Supermassive Black Hole at the Galactic Center. **39**, 309–352.
- Meyer, L. (2008). *The near-infrared activity of Sagittarius A**. Ph.D. thesis.
- Meyer, L., Schödel, R., Eckart, A., Karas, V., Dovčiak, M., and Duschl, W. J. (2006a). K-band polarimetry of an Sgr A* flare with a clear sub-flare structure. *A&A*, **458**, L25–L28.
- Meyer, L., Eckart, A., Schödel, R., Duschl, W. J., Mužić, K., Dovčiak, M., and Karas, V. (2006b). Near-infrared polarimetry setting constraints on the orbiting spot model for Sgr A* flares. *A&A*, **460**, 15–21.
- Meyer, L., Schödel, R., Eckart, A., Duschl, W. J., Karas, V., and Dovčiak, M. (2007). On the orientation of the Sagittarius A* system. *A&A*, **473**, 707–710.
- Meyer, L., Do, T., Ghez, A., Morris, M. R., Yelda, S., Schödel, R., and Eckart, A. (2009). A Power-Law Break in the Near-Infrared Power Spectrum of the Galactic Center Black Hole. *ApJ*, **694**, L87–L91.
- Meyer, L., Witzel, G., Longstaff, F. A., and Ghez, A. M. (2014a). A Formal Method for Identifying Distinct States of Variability in Time-varying Sources: Sgr A* as an Example. *ApJ*, **791**, 24.

- Meyer, L., Ghez, A. M., Witzel, G., Do, T., Phifer, K., Sitarski, B. N., Morris, M. R., Boehle, A., Yelda, S., Lu, J. R., and Becklin, E. (2014b). The Keplerian orbit of G2. In L. O. Sjouwerman, C. C. Lang, and J. Ott, editors, *IAU Symposium*, volume 303 of *IAU Symposium*, pages 264–268.
- Mezger, P. G., Zylka, R., Salter, C. J., Wink, J. E., Chini, R., Kreysa, E., and Tuffs, R. (1989). Continuum observations of SGR A at mm/submm wavelengths. *A&A*, **209**, 337–348.
- Moffet, A. T. (1975). *Strong Nonthermal Radio Emission from Galaxies*, page 211. the University of Chicago Press.
- Mori, K., Gotthelf, E. V., Zhang, S., An, H., Baganoff, F. K., Barrière, N. M., Beloborodov, A. M., Boggs, S. E., Christensen, F. E., Craig, W. W., Dufour, F., Grefenstette, B. W., Hailey, C. J., Harrison, F. A., Hong, J., Kaspi, V. M., Kennea, J. A., Madsen, K. K., Markwardt, C. B., Nynka, M., Stern, D., Tomsick, J. A., and Zhang, W. W. (2013). NuSTAR Discovery of a 3.76 s Transient Magnetar Near Sagittarius A*. *ApJ*, **770**, L23.
- Morris, M., Howard, C., Muno, M., Baganoff, F. K., Park, S., Feigelson, E., Garmire, G., and Brandt, N. (2004). The Hot Interstellar Medium of the Galactic Center: Observations with Chandra. In S. Pfalzner, C. Kramer, C. Staubmeier, and A. Heithausen, editors, *The Dense Interstellar Medium in Galaxies*, page 281.
- Murakawa, K. (2010). Polarization disks in near-infrared high-resolution imaging. *A&A*, **518**, A63.
- Murray-Clay, R. A. and Loeb, A. (2012). Disruption of a proto-planetary disc by the black hole at the milky way centre. *Nature Communications*, **3**, 1049.
- Mužić, K., Schödel, R., Eckart, A., Meyer, L., and Zensus, A. (2008). IRS 13N: a new comoving group of sources at the Galactic center. *A&A*, **482**, 173–178.
- Mužić, K., Eckart, A., Schödel, R., Buchholz, R., Zamaninasab, M., and Witzel, G. (2010). Comet-shaped sources at the Galactic center. Evidence of a wind from the central 0.2 pc. *A&A*, **521**, A13.
- Naghizadeh-Khouei, J. and Clarke, D. (1993). On the statistical behaviour of the position angle of linear polarization. *A&A*, **274**, 968.
- Narayan, R. and McClintock, J. E. (2008). Advection-dominated accretion and the black hole event horizon. *NewAR*, **51**, 733–751.
- Narayan, R., Yi, I., and Mahadevan, R. (1995). Explaining the spectrum of Sagittarius A* with a model of an accreting black hole. *Nature*, **374**, 623–625.
- O'dell, C. R. and Wen, Z. (1994). Postrefurbishment mission Hubble Space Telescope images of the core of the Orion Nebula: Proplyds, Herbig-Haro objects, and measurements of a circumstellar disk. *ApJ*, **436**, 194–202.

- Ott, T., Eckart, A., and Genzel, R. (1999). Variable and Embedded Stars in the Galactic Center. *ApJ*, **523**, 248–264.
- Park, J.-H., Trippe, S., Krichbaum, T. P., Kim, J.-Y., Kino, M., Bertarini, A., Bremer, M., and de Vicente, P. (2015). No asymmetric outflows from Sagittarius A* during the pericenter passage of the gas cloud G2. *A&A*, **576**, L16.
- Paumard, T., Genzel, R., Martins, F., Nayakshin, S., Beloborodov, A. M., Levin, Y., Trippe, S., Eisenhauer, F., Ott, T., Gillessen, S., Abuter, R., Cuadra, J., Alexander, T., and Sternberg, A. (2006). The Two Young Star Disks in the Central Parsec of the Galaxy: Properties, Dynamics, and Formation. *ApJ*, **643**, 1011–1035.
- Pfuhl, O., Gillessen, S., Eisenhauer, F., Genzel, R., Plewa, P. M., Ott, T., Ballone, A., Schartmann, M., Burkert, A., Fritz, T. K., Sari, R., Steinberg, E., and Madigan, A.-M. (2015). The Galactic Center Cloud G2 and its Gas Streamer. *ApJ*, **798**, 111.
- Phifer, K., Do, T., Meyer, L., Ghez, A. M., Witzel, G., Yelda, S., Boehle, A., Lu, J. R., Morris, M. R., Becklin, E. E., and Matthews, K. (2013). Keck Observations of the Galactic Center Source G2: Gas Cloud or Star? *ApJ*, **773**, L13.
- Pineault, S. (1980). Giant flares on supermassive accretion disks - Polarization properties and energetics. *ApJ*, **241**, 528–533.
- Pollack, L. K., Taylor, G. B., and Zavala, R. T. (2003). VLBI Polarimetry of 177 Sources from the Caltech-Jodrell Bank Flat-Spectrum Survey. *ApJ*, **589**, 733–751.
- Ponti, G., De Marco, B., Morris, M. R., Merloni, A., Munoz-Darias, T., Clavel, M., Haggard, D., Zhang, S., Nandra, K., Gillessen, S., Mori, K., Neilsen, J., Rea, N., Degenaar, N., Terrier, R., and Goldwurm, A. (2015). Fifteen years of XMM-Newton and Chandra monitoring of Sgr A*: Evidence for a recent increase in the bright flaring rate. *ArXiv e-prints*.
- Porquet, D., Predehl, P., Aschenbach, B., Grosso, N., Goldwurm, A., Goldoni, P., Warwick, R. S., and Decourchelle, A. (2003). XMM-Newton observation of the brightest X-ray flare detected so far from Sgr A*. *A&A*, **407**, L17–L20.
- Press, W. H., Teukolsky, S. A., Vetterling, W. T., and Flannery, B. P. (1992). *Numerical recipes in C. The art of scientific computing*.
- Rauch, C., Mužić, K., Eckart, A., Buchholz, R. M., García-Marín, M., Sabha, N., Straubmeier, C., Valencia-S., M., and Yazici, S. (2013). A peek behind the dusty curtain: K_S-band polarization photometry and bow shock models of the Galactic center source IRS 8. *A&A*, **551**, A35.
- Reid, M. J. (1993). The distance to the center of the Galaxy. **31**, 345–372.

- Reid, M. J., Readhead, A. C. S., Vermeulen, R. C., and Treuhaft, R. N. (1999). The Proper Motion of Sagittarius A*. I. First VLBA Results. *ApJ*, **524**, 816–823.
- Requena-Torres, M. A., Güsten, R., Weiß, A., Harris, A. I., Martín-Pintado, J., Stutzki, J., Klein, B., Heyminck, S., and Risacher, C. (2012). GREAT confirms transient nature of the circum-nuclear disk. *A&A*, **542**, L21.
- Revnivtsev, M. G., Churazov, E. M., Sazonov, S. Y., Sunyaev, R. A., Lutovinov, A. A., Gilfanov, M. R., Vikhlinin, A. A., Shtykovsky, P. E., and Pavlinsky, M. N. (2004). Hard X-ray view of the past activity of Sgr A* in a natural Compton mirror. *A&A*, **425**, L49–L52.
- Richardson, R. (1972). Bayesian-Based Iterative Method of Image Restoration. *JOSA*, **62**, 55.
- Rockefeller, G., Fryer, C. L., Melia, F., and Warren, M. S. (2004). Diffuse X-Rays from the Inner 3 Parsecs of the Galaxy. *ApJ*, **604**, 662–670.
- Rost, S., Eckart, A., and Ott, T. (2008). Near-infrared polarization images of the Orion proplyds. *A&A*, **485**, 107–116.
- Rousset, G., Lacombe, E., Puget, P., Hubin, N. N., Gendron, E., Fusco, T., Arsenault, R., Charton, J., Feautrier, P., Gigan, P., Kern, P. Y., Lagrange, A.-M., Madec, P.-Y., Mouillet, D., Rabaud, D., Rabou, P., Stadler, E., and Zins, G. (2003). NAOS, the first AO system of the VLT: on-sky performance. In P. L. Wizinowich and D. Bonaccini, editors, *Adaptive Optical System Technologies II*, volume 4839 of *Society of Photo-Optical Instrumentation Engineers (SPIE) Conference Series*, pages 140–149.
- Sabha, N., Witzel, G., Eckart, A., Buchholz, R. M., Bremer, M., Gießübel, R., García-Marín, M., Kunneriath, D., Muzic, K., Schödel, R., Straubmeier, C., Zamaninasab, M., and Zernicke, A. (2010). The extreme luminosity states of Sagittarius A*. *A&A*, **512**, A2.
- Sabha, N., Eckart, A., Merritt, D., Zamaninasab, M., Witzel, G., García-Marín, M., Jalali, B., Valencia-S., M., Yazici, S., Buchholz, R., Shahzamanian, B., Rauch, C., Horrobin, M., and Straubmeier, C. (2012). The S-star cluster at the center of the Milky Way. On the nature of diffuse NIR emission in the inner tenth of a parsec. *A&A*, **545**, A70.
- Sądowski, A., Sironi, L., Abarca, D., Guo, X., Özel, E., and Narayan, R. (2013). Radio light curves during the passage of cloud G2 near Sgr A*. *MNRAS*, **432**, 478–491.
- Schartmann, M., Burkert, A., Alig, C., Gillessen, S., Genzel, R., Eisenhauer, F., and Fritz, T. K. (2012). Simulations of the Origin and Fate of the Galactic Center Cloud G2. *ApJ*, **755**, 155.

- Schödel, R., Ott, T., Genzel, R., Hofmann, R., Lehnert, M., Eckart, A., Mouawad, N., Alexander, T., Reid, M. J., Lenzen, R., Hartung, M., Lacombe, F., Rouan, D., Gendron, E., Rousset, G., Lagrange, A., Brandner, W., Ageorges, N., Lidman, C., Moorwood, A. F. M., Spyromilio, J., Hubin, N., and Menten, K. M. (2002). A star in a 15.2-year orbit around the supermassive black hole at the centre of the Milky Way. *Nature*, **419**, 694–696.
- Schödel, R., Ott, T., Genzel, R., Eckart, A., Mouawad, N., and Alexander, T. (2003). Stellar Dynamics in the Central Arcsecond of Our Galaxy. *ApJ*, **596**, 1015–1034.
- Schödel, R., Najarro, E., Muzic, K., and Eckart, A. (2010). Peering through the veil: near-infrared photometry and extinction for the Galactic nuclear star cluster. Accurate near infrared H, Ks, and L' photometry and the near-infrared extinction-law toward the central parsec of the Galaxy. *A&A*, **511**, A18.
- Scoville, N. and Burkert, A. (2013). The Galactic Center Cloud G2a Young Low-mass Star with a Stellar Wind. *ApJ*, **768**, 108.
- Serkowski, K. (1958). Statistical Analysis of the Polarization and Reddening of the Double Cluster in Perseus. *Acta Astronomica*, **8**, 135.
- Serkowski, K. (1962). *Advances in Astronomy and Astrophysics*, eds. Z. Kopal. Academic Press 1. page 289.
- Shahzamanian, B., Eckart, A., Valencia-S., M., Witzel, G., Zamaninasab, M., Sabha, N., García-Marín, M., Karas, V., Karssen, G. D., Borkar, A., Dovčiak, M., Kunneriath, D., Bursa, M., Buchholz, R., Moultaqa, J., and Straubmeier, C. (2015). Polarized light from Sagittarius A* in the near-infrared K_s-band. *A&A*, **576**, A20.
- Shahzamanian, B., Eckart, A., Zajaček, M., Valencia-S., M., Sabha, N., Moser, L., Parsa, M., Peissker, F., and Straubmeier, C. (2016). Polarized near-infrared light of the Dusty S-cluster Object (DSO/G2) at the Galactic center. *A&A*, **593**, A131.
- Shakura, N. I. and Sunyaev, R. A. (1973). Black holes in binary systems. Observational appearance. *A&A*, **24**, 337–355.
- Shcherbakov, R. V. (2014). The Properties and Fate of the Galactic Center G2 Cloud. *ApJ*, **783**, 31.
- Shcherbakov, R. V. and Baganoff, F. K. (2010). Inflow-Outflow Model with Conduction and Self-consistent Feeding for Sgr A*. *ApJ*, **716**, 504–509.
- Silant'ev, N. A., Piotrovich, M. Y., Gnedin, Y. N., and Natsvlshvili, T. M. (2009). Magnetic fields of AGNs and standard accretion disk model: testing by optical polarimetry. *A&A*, **507**, 171–182.

- Simmons, J. F. L. and Stewart, B. G. (1985). Point and interval estimation of the true unbiased degree of linear polarization in the presence of low signal-to-noise ratios. *A&A*, **142**, 100–106.
- Stewart, B. G. (1991). Polynomial FITS for Polarization Estimation. *A&A*, **246**, 280.
- Störzner, H. and Hollenbach, D. (1999). Photodissociation Region Models of Photoevaporating Circumstellar Disks and Application to the Proplyds in Orion. *ApJ*, **515**, 669–684.
- Sunyaev, R. A., Markevitch, M., and Pavlinsky, M. (1993). The center of the Galaxy in the recent past - A view from GRANAT. *ApJ*, **407**, 606–610.
- Symington, N. H., Harries, T. J., and Kurosawa, R. (2005). Emission-line profile modelling of structured T Tauri magnetospheres. *MNRAS*, **356**, 1489–1500.
- Tanner, A., Ghez, A. M., Morris, M., Becklin, E. E., Cotera, A., Ressler, M., Werner, M., and Wizinowich, P. (2002). Spatially Resolved Observations of the Galactic Center Source IRS 21. *ApJ*, **575**, 860–870.
- Terrier, R., Ponti, G., Bélanger, G., Decourchelle, A., Tatischeff, V., Goldwurm, A., Trap, G., Morris, M. R., and Warwick, R. (2010). Fading Hard X-ray Emission from the Galactic Center Molecular Cloud Sgr B2. *ApJ*, **719**, 143–150.
- Trippe, S. (2014). [Review] Polarization and Polarimetry. *Journal of Korean Astronomical Society*, **47**, 15–39.
- Trippe, S., Paumard, T., Ott, T., Gillessen, S., Eisenhauer, F., Martins, F., and Genzel, R. (2007). A polarized infrared flare from Sagittarius A* and the signatures of orbiting plasma hotspots. *MNRAS*, **375**, 764–772.
- Valencia-S., M., Eckart, A., Zajaček, M., Peissker, F., Parsa, M., Grosso, N., Mossoux, E., Porquet, D., Jalali, B., Karas, V., Yazici, S., Shahzamanian, B., Sabha, N., Saalfeld, R., Smajić, S., Grellmann, R., Moser, L., Horrobin, M., Borkar, A., García-Marín, M., Dovčiak, M., Kunneriath, D., Karssen, G. D., Bursa, M., Straubmeier, C., and Bushouse, H. (2015). Monitoring the Dusty S-cluster Object (DSO/G2) on its Orbit toward the Galactic Center Black Hole. *ApJ*, **800**, 125.
- Vinokur, M. (1965). Optimisation dans la recherche d'une sinusoïde de période connue en présence de bruit. Application à la radioastronomie. *Annales d'Astrophysique*, **28**, 412.
- Wall, J. V. and Jenkins, C. R. (2012). *Practical Statistics for Astronomers*.
- Whitney, B. A. and Wolff, M. J. (2002). Scattering and Absorption by Aligned Grains in Circumstellar Environments. *ApJ*, **574**, 205–231.

- Witzel, G., Eckart, A., Buchholz, R. M., Zamaninasab, M., Lenzen, R., Schödel, R., Araujo, C., Sabha, N., Bremer, M., Karas, V., Straubmeier, C., and Muzic, K. (2011). The instrumental polarization of the Nasmyth focus polarimetric differential imager NAOS/CONICA (NACO) at the VLT. Implications for time-resolved polarimetric measurements of Sagittarius A*. *A&A*, **525**, A130.
- Witzel, G., Eckart, A., Bremer, M., Zamaninasab, M., Shahzamanian, B., Valencia-S., M., Schödel, R., Karas, V., Lenzen, R., Marchili, N., Sabha, N., Garcia-Marin, M., Buchholz, R. M., Kunneriath, D., and Straubmeier, C. (2012). Source-intrinsic Near-infrared Properties of Sgr A*: Total Intensity Measurements. *ApJS*, **203**, 18.
- Witzel, G., Ghez, A. M., Morris, M. R., Sitarski, B. N., Boehle, A., Naoz, S., Campbell, R., Becklin, E. E., Canalizo, G., Chappell, S., Do, T., Lu, J. R., Matthews, K., Meyer, L., Stockton, A., Wizinowich, P., and Yelda, S. (2014). Detection of Galactic Center Source G2 at 3.8 μm during Periapse Passage. *ApJ*, **796**, L8.
- Wright, M. C. H., Coil, A. L., McGary, R. S., Ho, P. T. P., and Harris, A. I. (2001). Molecular Tracers of the Central 12 Parsecs of the Galactic Center. *ApJ*, **551**, 254–268.
- Yuan, F and Narayan, R. (2014). Hot Accretion Flows Around Black Holes. *ARA&A*, **52**, 529–588.
- Yuan, F, Quataert, E., and Narayan, R. (2003). Nonthermal Electrons in Radiatively Inefficient Accretion Flow Models of Sagittarius A*. *ApJ*, **598**, 301–312.
- Yuan, F, Quataert, E., and Narayan, R. (2004). On the Nature of the Variable Infrared Emission from Sagittarius A*. *ApJ*, **606**, 894–899.
- Yuan, F, Lin, J., Wu, K., and Ho, L. C. (2009). A magnetohydrodynamical model for the formation of episodic jets. *MNRAS*, **395**, 2183–2188.
- Yudin, R. V. and Evans, A. (1998). Polarimetry of southern peculiar early-type stars. *A&AS*, **131**, 401–429.
- Yusef-Zadeh, F, Roberts, D. A., and Biretta, J. (1998). Proper Motions of Ionized Gas at the Galactic Center: Evidence for Unbound Orbiting Gas. *ApJ*, **499**, L159+.
- Yusef-Zadeh, F, Bushouse, H., Dowell, C. D., Wardle, M., Roberts, D., Heinke, C., Bower, G. C., Vila-Vilaró, B., Shapiro, S., Goldwurm, A., and Bélanger, G. (2006a). A Multiwavelength Study of Sgr A*: The Role of Near-IR Flares in Production of X-Ray, Soft γ -Ray, and Submillimeter Emission. *ApJ*, **644**, 198–213.
- Yusef-Zadeh, F, Roberts, D., Wardle, M., Heinke, C. O., and Bower, G. C. (2006b). Flaring Activity of Sagittarius A* at 43 and 22 GHz: Evidence for Expanding Hot Plasma. *ApJ*, **650**, 189–194.

- Yusef-Zadeh, F., Wardle, M., Cotton, W. D., Heinke, C. O., and Roberts, D. A. (2007). The Variability of Polarized Radiation from Sagittarius A*. *ApJ*, **668**, L47–L50.
- Yusef-Zadeh, F., Wardle, M., Heinke, C., Dowell, C. D., Roberts, D., Baganoff, F. K., and Cotton, W. (2008). Simultaneous Chandra, CSO, and VLA Observations of Sgr A*: The Nature of Flaring Activity. *ApJ*, **682**, 361–372.
- Yusef-Zadeh, F., Bushouse, H., Wardle, M., Heinke, C., Roberts, D. A., Dowell, C. D., Brunthaler, A., Reid, M. J., Martin, C. L., Marrone, D. P., Porquet, D., Grosso, N., Dodds-Eden, K., Bower, G. C., Wiesemeyer, H., Miyazaki, A., Pal, S., Gillessen, S., Goldwurm, A., Trap, G., and Maness, H. (2009). Simultaneous Multi-Wavelength Observations of Sgr A* During 2007 April 1–11. *ApJ*, **706**, 348–375.
- Yusef-Zadeh, F., Bushouse, H., Schödel, R., Wardle, M., Cotton, W., Roberts, D. A., Nogueras-Lara, F., and Gallego-Cano, E. (2015). Compact Radio Sources within 30' of Sgr A*: Proper Motions, Stellar Winds, and the Accretion Rate onto Sgr A*. *ApJ*, **809**, 10.
- Zajaček, M., Karas, V., and Eckart, A. (2014). Dust-enshrouded star near supermassive black hole: predictions for high-eccentricity passages near low-luminosity galactic nuclei. *A&A*, **565**, A17.
- Zamaninasab, M., Eckart, A., Meyer, L., Schödel, R., Dovciak, M., Karas, V., Kunneriath, D., Witzel, G., Gießübel, R., König, S., Straubmeier, C., and Zensus, A. (2008). An evolving hot spot orbiting around Sgr A*. *Journal of Physics Conference Series*, **131**(1), 012008–+.
- Zamaninasab, M., Eckart, A., Witzel, G., Dovciak, M., Karas, V., Schödel, R., Gießübel, R., Bremer, M., García-Marín, M., Kunneriath, D., Mužić, K., Nishiyama, S., Sabha, N., Straubmeier, C., and Zensus, A. (2010). Near infrared flares of Sagittarius A*. Importance of near infrared polarimetry. *A&A*, **510**, A3.
- Zhao, J.-H., Bower, G. C., and Goss, W. M. (2001). Radio Variability of Sagittarius A*-a 106 Day Cycle. *ApJ*, **547**, L29–L32.
- Zylka, R., Mezger, P. G., Ward-Thompson, D., Duschl, W. J., and Lesch, H. (1995). Anatomy of the Sagittarius A complex. 4: SGR A* and the Central Cavity revisited. *A&A*, **297**, 83–97.

LIST OF FIGURES

1.1	Composite image of the Galactic Center	2
1.2	Chandra X-ray image of Sagittarius A	3
1.3	Multi-wavelength image of the central few parsecs of the Galactic Center	4
1.4	H, K, and L' band composite image of the GC	5
1.5	Astrometric positions of S2 and stellar orbits around Sgr A*	6
1.6	Spectral energy distribution of Sgr A*	8
2.1	The Very Large Telescope	15
2.2	Polarimetry image of GC in K_s -band	16
2.3	Illustration of the Adaptive Optics system	18
2.4	Central few arcseconds region of GC in K_s -band in 2012	22
3.1	K_s -band deconvolved image of the GC	29
3.2	Light curves of Sgr A* for 2011 and 2012 data	30
3.3	Flux density distributions of Sgr A* flux calibrators and their standard deviation	32
3.4	Sgr A* light curves and polarization measurements of our data set	35
3.5	Simulated values of the polarization degree and angle for the high flux densities	39
3.6	Simulated values of the polarization degree and angle for the low flux densities	41
3.7	Relation between simulated values of total flux density and polarization degree	42
3.8	Distribution of polarization degrees of Sgr A* by considering the significant measurements	43
3.9	Distribution of polarization angles of Sgr A* by considering the significant measurements	44
3.10	The relation between polarization degree and angle uncertainties	45
3.11	The relation of polarization angle with Altitude and total flux density of Sgr A* for significant measurements	46
3.12	Polarized flux density histogram for the significant measurements in logarithmic scale	47
3.13	Different PDFs fitted to the polarized flux density distribution	50
3.14	Total flux density distribution of Sgr A*	51
3.15	Heuristic model describing polarized flux density distribution	52

3.16	Relation between total flux density and polarization measurements for significant data	54
3.17	Direction of intrinsic polarization angle of Sgr A* in the GC	59
4.1	Deconvolved <i>L</i> -band images of the central arcsecond at the GC	62
4.2	DSO spectrum decomposition	63
4.3	NIR spectrum of the DSO	64
4.4	Infrared excess sources at the central few arcseconds of the GC	65
4.5	K_s -band deconvolved median images of the central arcsecond of the GC in polarimetry mode	67
4.6	Light curve of the DSO observed in polarimetry mode	69
4.7	A sketch showing the DSO polarization angle variation	70
4.8	Distribution of polarization degree	72
.1	Distribution of the polarization angles and degrees of Sgr A* for the entire data set	77
.2	The relation of the polarization angle with Altitude and total flux density of Sgr A* for the whole data set	78
.3	Polarized flux density distribution for the whole data set	78
.4	The relation of total flux density with polarization angle and degree for the whole data set	79

LIST OF TABLES

3.1	Observations Log	27
3.2	List of calibrators and their calculated flux densities	28
3.3	Average values of recovered polarization degrees obtained by simulation	40
3.4	Average values of recovered polarization angles obtained by simulation	40
3.5	Fit parameters to the polarized flux density distribution.	50
3.6	Comparison of the obtained polarization measurements of Sgr A* with the ones reported in the literature	58
4.1	Galactic Center Observations Log	66
4.2	Polarimetry results of the DSO	70

LIST OF ACRONYMS

ADAF	Advection-Dominated Accretion Flow
ADC	Analog-to-Digital Converter
AGB	Asymptotic-Giant-Branch;sequence of stellar evolution identified in the H-R diagram
AGN	Active Galactic Nucleus
AO	Adaptive Optics
BH	Black Hole
CDF	Cumulative Distribution Function
CND	Circumnuclear Disk
DSO	Dusty S-cluster Object
ESO	European Southern Observatory
FOV	Field of View
FWHM	Full Width Half Maximum
GC	Galactic Center
HST	Hubble Space Telescope
KS	Kolmogorov-Smirnov
LGS	Laser Guide Star
LLAGN	Low Luminosity AGN
LOS	Line Of Sight
LR	Lucy-Richardson
mas	milli arcsecond
MLE	Maximum Likelihood Estimator
NACO	Nasmyth Adaptive Optics System/Coude Near Infrared Camera
NIR	Near-InfraRed
NSC	Nuclear Stellar Cluster
pc	parsec
PDF	Probability Density Function
PSF	Point Spread Function
QPO	Quasi Periodic Oscillation
RIAF	Radiatively Inefficient Accretion Flow
rms	Root Mean Square
S/N	Signal to Noise ratio

SED	Spectral Energy Distribution; brightness or flux density versus frequency or wavelength of light
Sgr A*	Sagittarius A*
SMA	Submillimeter Array
SMBH	Super Massive Black Hole; black hole whose mass exceeds $10^6 M_{\odot}$
SSC	Synchrotron Self-Compton
VLBI	Very Large Baseline Interferometry
VLT	Very Large Telescope
VLTI	Very Large Telescope Interferometer
WFS	Wave Front Sensor
WR	Wolf-Rayet
YSO	Young Stellar Object

ACKNOWLEDGEMENTS

There are many people who have supported me during my PhD work. I would like to thank all and express my gratitude to them. First of all, I would like to give my warmest thanks to my supervisor, Prof. Dr. Andreas Eckart. Whenever I had questions he was there to suggest new and creative ideas. I thank him for the support, encouragement, giving me the opportunity to work on a fascinating topic and have a great experience of performing observations. And for translating the thesis abstract to German.

Thanks to Prof. Andreas Eckart, Prof. Anton Zensus, Dr. Mohammad Zamaninasab, Dr. Macarena Garcia-Marin, and Dr. Monica Valencia-S. for being members of my IMPRS PhD thesis committee. This work was partially supported by the Bonn Cologne Graduate School (BCGS) for Physics and Astronomy, the German Deutsche Forschungsgemeinschaft, DFG, via grant SFB 956, and the International Max Planck Research School (IMPRS) for Astronomy and Astrophysics at the MPIfR and the Universities of Bonn and Cologne.

I am grateful to Mohammad Zamaninasab who helped me kindly during the difficult part of my research topic, on the interpretation of the data, with his great knowledge in astrophysics. I thank him because of his patience, time, and all the motivating scientific discussions. To Gunther Witzel, for introducing me to the fascinating world of observation and data, and supporting me in the data reduction process. To Monica Valencia-S., for fruitful scientific discussions, for helping with the error analysis by performing the simulations, and answering to my emails directly. Thanks to all the ESO staff who have helped me during my trips to Paranal.

I am grateful to all the Ph1 secretaries, for their assistance with all the bureaucratic problems that made my life as a PhD student much easier. To Dr. Petra Neubauer-Guenther, for being helpful regarding all the BCGS concerns. And to the Physics Institute library where I spent the last 3 months of my PhD, during which I wrote the major parts of my thesis, and read many papers.

Special thanks goes to Nadeen Sabha, Lydia Moser, and Behrang Jalali for reading the contents of my thesis and commenting on it.

I would like to thank the entire aegroup for the friendly and productive working atmosphere, for the friendly chats, the technical support, and helping with German translation. A big thank you to my officemates across the years, Gerold, Markus, Kostas, Gunther, and Balaji for the fun times, cookies, chats, and the support they provided me.

I thank my Cologne and Bonn friends, Abhijeet, Angela, Nadeen, Hananeh, Silvia, Lydia, Senol, Mohammad, Gerold, Nastaran, Monica, Markus, Gunther, Zeinab, Maryam, Behrang, Fabio, Jan, Juan Andres, Yasir, Rebekka, Eric, Anas, Ati, Balaji, Elena, Ketki, Prasanna, and Nandita for all the good times and making these last years enjoyable and great. Especially, Zeinab and Gunther, for their support and help during my first months in Bonn and Cologne. To Gerold for sitting 3 hours to help me when the Latex file of my thesis behaved "scarily". To Behrang, for encouraging me with a positive attitude during the PhD and providing help time to time.

My special thanks to my friends since old times especially Shiva, Maryam, and Nafiseh, for being such good and caring friends.

To my extended family, for all the good wishes and encouragements. To my aunts, for being with my Mum back home when I was not there. To the dear memory of my aunt, Shahla, that I will never forget all her kindness. To my uncle, Bijan, who was my first idol of knowledge and encouraged me to continue my studies in physics.

To Angela and Silvia, for the fun times including IMPRS gatherings and retreats in the beginning, for being supportive and for the delicious Italian dishes. To my good friend, Hananeh, who encouraged and supported me emotionally during the last years, for the home parties, for working together, and for all the fun times.

A big thanks goes to my kind friend, Nadeen, for the motivating scientific/non-scientific conversations and all the fun times. For commenting on my work, for always providing IDL support, and for providing help whenever I needed. Her encouragement and support helped me to face the challenging times of my PhD, especially the last months. I appreciate her huge support till the last minutes before the submission of the thesis. The trips to Paranal became more exciting with her presence.

Last but not least, I would like to thank my lovely family for their love, support and encouraging me to go after my dreams in life. I thank my mother, Behnaz, for her patience, and everything that made it possible for me to reach this stage of my life. I thank my father, Reza, for initiating my interest in mathematics and physics, and advising me to never give up! I thank my brother, Behzad, for his support through the last years and always. I also thank Mansoureh, for all the support. And finally, I thank Mahmoud, my old good friend, for being so supportive and understanding during all the time of my PhD, I admire his patience and I am very grateful for all the good times we had.

ERKLÄRUNG

Ich versichere, daß ich die von mir vorgelegte Dissertation selbständig angefertigt, die benutzten Quellen und Hilfsmittel vollständig angegeben und die Stellen der Arbeit – einschließlich Tabellen, Karten und Abbildungen –, die anderen Werken im Wortlaut oder dem Sinn nach entnommen sind, in jedem Einzelfall als Entlehnung kenntlich gemacht habe; daß diese Dissertation noch keiner anderen Fakultät oder Universität zur Prüfung vorgelegen hat; daß sie – abgesehen von unten angegebenen Teilpublikationen – noch nicht veröffentlicht worden ist sowie, daß ich eine solche Veröffentlichung vor Abschluß des Promotionsverfahrens nicht vornehmen werde. Die Bestimmungen dieser Promotionsordnung sind mir bekannt. Die von mir vorgelegte Dissertation ist von Prof. Dr. Andreas Eckart betreut worden.

Köln, 07.09.2015

Teilpublikationen

- **Shahzamanian, B.**; Eckart, A.; Zajacek, M.; Valencia-S., M., Sabha, N.; Moser, L.; Parsa, M.; Peissker, F.; Straubmeier, C. (2016) *Polarized near-infrared light of the Dusty S-cluster Object (DSO/G2) at the Galactic center* A&A, 593, A131
- **Shahzamanian, B.**; Eckart, A.; Valencia-S., M.; Witzel, G.; Zamaninasab, M.; Sabha, N.; Garcia-Marin, M.; Karas, V.; Karssen, G. D.; Borkar, A.; Dovciak, M.; Kunneriath, D.; Bursa, M.; Buchholz, R.; Moulataka, J.; Straubmeier, C. (2015) *Polarized light from Sagittarius A* in the near-infrared K_s-band* A&A, 576, A20
- **Shahzamanian, B.**; Eckart, A.; Valencia-S., M.; Witzel, G.; Zamaninasab, M.; Zajacek, M.; Sabha, N.; Garcia-Marin, M.; Karas, V. et al. (2015) *Variable and Polarised Near-infrared Emission from the Galactic Centre* in Messenger, 159, 41-45
- **Shahzamanian, B.**; Eckart, A.; Zamaninasab, M.; Witzel, G.; Sabha, N. (2014) *Ob-*

*servations of NIR polarized light from Sagittarius A** in IAU, 303, 283-287

- **Shahzamanian, B.**; Eckart, A.; Witzel, G.; Sabha, N.; Zamaninasab, M. (2012) *Polarized NIR observations of Sagittarius A** in PoS, Seyfert 2012, 074
- Eckart, A.; Valencia-S., M.; **Shahzamanian, B.**; Garcia-Marin, M.; Peissker, F.; Zajacek, M.; Parsa, M.; Jalali, B.; Saalfeld, R.; Sabha, N.; Yazic, S.; Karssen, G. D.; Borkar, A.; Markakis, K.; Zensus, J. A.; Straubmeier, C. (2015) *The Center of the Milky Way from Radio to X-rays* in PoS-SISSA

Weitere Publikationen

- Valencia-S., M.; Eckart, A.; Zajacek, M.; Peissker, F.; Parsa, M.; Grosso, N.; Mossoux, E.; Porquet, D.; Jalali, B.; Karas, V.; Yazici, S.; **Shahzamanian, B.**; Sabha, N.; Saalfeld, R.; Smajic, S.; Grellmann, R.; Moser, L.; Horrobin, M.; Borkar, A.; Garcia-Marin, M.; Dovciak, M.; Kunneriath, D.; Karssen, G. D.; Bursa, M.; Straubmeier, C.; Bushouse, H. (2015) *Monitoring the Dusty S-cluster Object (DSO/G2) on its Orbit toward the Galactic Center Black Hole* ApJ, 800, 2, article id. 125, 21 pp
- Eckart, A.; Valencia-S., M.; Peissker, F.; Grosso, N.; Mossoux, E.; Porquet, D.; Karas, V.; Dovciak, M.; Smajic, S.; Yazici, S.; Moser, L.; **Shahzamanian, B.**; Garcia-Marin, M.; Zajacek, M.; Karssen, G. D.; Bursa, M.; Kunneriath, D.; Straubmeier, C. (2014) *Monitoring the Dusty S-cluster Object (DSO/G2) on its orbit towards the Galactic Center Black Hole: Periapse not yet reached* in Astronomer's Telegram, #6285
- Eckart, A.; Horrobin, M.; Britzen, S.; Zamaninasab, M.; Muzic, K.; Sabha, N.; **Shahzamanian, B.**; Yazici, S.; Moser, L.; Garcia-Marin, M.; Valencia-S., M.; Borkar, A.; Bursa, M.; Karssen, G.; Karas, V.; Zajacek, M.; Bronfman, L.; Finger, R.; Jalali, B.; Vitale, M.; Rauch, C.; Kunneriath, D.; Moulataka, J.; Straubmeier, C.; Rashed, Y. E.; Markakis, K.; Zensus, A. *The infrared K-band identification of the DSO/G2 source from VLT and Keck data* (2014) in IAU, 303, 269-273
- Moser, Lydia; Eckart, A.; Borkar, A.; Garcia-Marin, M.; Kunneriath, D.; Jalali, B.; Sabha, N.; **Shahzamanian, B.**; Valencia-S., M.; Zamaninasab, M.; Bronfman, L.; Finger, R. *Sgr A West in the light of molecules: cold and dense gas east of the circumnuclear disk* (2014) in IAU, 303, 86-88
- Eckart, A.; Muzic, K.; Yazici, S.; Sabha, N.; **Shahzamanian, B.**; Witzel, G.; Moser, L.; Garcia-Marin, M.; Valencia-S., M.; Jalali, B.; Bremer, M.; Straubmeier, C.; Rauch,

C.; Buchholz, R.; Kunneriath, D.; Moulataka, J. (2013) *Near-infrared proper motions and spectroscopy of infrared excess sources at the Galactic center* A&A, 551, id.A18, 31 pp

- Eckart, A.; Muzic, K.; Yazici, S.; Sabha, N.; **Shahzamanian, B.**; Witzel, G.; Moser, L.; Garcia-Marin, M.; Valencia-S., M.; Jalali, B.; Bremer, M.; Straubmeier, C.; Rauch, C.; Buchholz, R.; Kunneriath, D.; Moulataka, J. (2013) *The broad band spectral properties of SgrA* . The fate of the dusty object approaching the center* in Memorie della Societa Astronomica Italiana, 84, 618

- Witzel, G.; Eckart, A.; Bremer, M.; Zamaninasab, M.; **Shahzamanian, B.**; Valencia-S., M.; Schoedel, R.; Karas, V.; Lenzen, R.; Marchili, N.; Sabha, N.; Garcia-Marin, M.; Buchholz, R. M.; Kunneriath, D.; Straubmeier, C. (2012) *Source-intrinsic Near-infrared Properties of Sgr A* : Total Intensity Measurements* ApJS, 203, 2, article id. 18, 36 pp

- Sabha, N.; Eckart, A.; Merritt, D.; Zamaninasab, M.; Witzel, G.; Garcia-Marin, M.; Jalali, B.; Valencia-S., M.; Yazici, S.; Buchholz, R.; **Shahzamanian, B.**; Rauch, C.; Horrobin, M.; Straubmeier, C. (2012) *The S-star cluster at the center of the Milky Way. On the nature of diffuse NIR emission in the inner tenth of a parsec* A&A, 545, id.A70, 12 pp

- Eckart, A.; Sabha, N.; Witzel, G.; Straubmeier, C.; **Shahzamanian, B.**; Valencia-S., M.; Garcia-Marin, Macarena; Horrobin, M.; Moser, L.; Zuther, J.; Fischer, S.; Rauch, C.; Rost, S.; Iserlohe, C.; Yazici, S.; Smajic, S.; Wiest, M.; Araujo-Hauck, C.; Wank, I. (2012) *Beating the confusion limit: the necessity of high angular resolution for probing the physics of Sagittarius A* and its environment: opportunities for LINC-NIRVANA (LBT), GRAVITY (VLT) and METIS (E-ELT)* in SPIE Proceedings, 8445, article id. 84451F, 10 pp

- Eckart, A.; Britzen, S.; Horrobin, M.; Zamaninasab, M.; Muzic, K.; Sabha, N.; **Shahzamanian, B.**; Yazici, S.; Moser, L.; Zuther, J.; Garcia-Marin, M.; Valencia-S., M.; Bursa, M.; Karssen, G.; Karas, V.; Jalali, B.; Vitale, M.; Bremer, M.; Fischer, S.; Smajic, S.; Rauch, C.; Kunneriath, D.; Moulataka, J.; Straubmeier, C.; Rashed, Y. E.; Iserlohe, C.; Busch, G.; Markakis, K.; Borkar, A.; Zensus, A. J. (2012) *The Galactic Center as a paradigm for low-luminosity nuclei? What can be learned from SgrA* for the central engine and conditions of star formation in nuclei of Seyfert galaxies and low luminosity nearby QSOs; The K-band identification of the DSO/G2 source from VLT and Keck data* in PoS, Seyfert 2012, 4

Lebenslauf

Name: Banafsheh Shahzamanian Sichani
Anschrift: I. Physikalisches Institut, Universität zu Köln
Zülpicher Str. 77, 50937 Köln, Deutschland
Email: shahzaman@ph1.uni-koeln.de
Geburtsort: Isfahan, Iran
Geburtsdatum: 20.09.1982
Staatsangehörigkeit: Iranisch

Ausbildung

Seit August 2011 Promotionsstudentin an der Universität zu Köln und dem
Max-Planck-Institut für Radioastronomie
wiss. Betreuer: Prof. Dr. Andreas Eckart
2008-2011 Lehrerin für Astronomie und Astrophysik an der
Adib Astronomie Center
Isfahan, Iran
2006-2009 Master der Astrophysik an der University of Zanjan
Zanjan, Iran
wiss. Betreuer: Prof. Sadollah Nasiri und Dr. Sepehr Arbabi
Titel: "A study of galaxy evolution in low density environments
as compared to the high density regions of galaxy clusters and groups"
2001-2005 Bachelor der Physik an der University of Isfahan
Isfahan, Iran

Stipendium

2012-2014 Stipendium der *Bonn Cologne Graduate School (BCGS)*
of Physics and Astronomy

Astronomy and Astrophysics

Editor in Chief: T. Forveille

T. Forveille

Astronomy & Astrophysics
Observatoire de Paris
61, avenue de l'Observatoire
75014 Paris, France

Tel.: 33 0(1) 43 29 05 41
Fax: 33 0(1) 43 29 05 57
e-mail: aanda.paris@obspm.fr
Web: <http://www.aanda.org>

merging
Annales d'Astrophysique
Arkiv for Astronomi
Bulletin of the Astronomical Institutes
of the Netherlands
Bulletin Astronomique
Journal des Observateurs
Zeitschrift fur Astrophysik
Bulletin of the Astronomical Institutes
of Czechoslovakia

Paris, April 4, 2016

Reprint Permission

Material:

All tables and figures from Shahzamanian et al. 2015, A&A 576, A20

To be used in:

PhD thesis entitled "Near-Infrared polarimetry in the Galactic Center-on properties of Sagittarius A* and a dusty S-cluster object", University of Cologne

Permission granted to:

Banafsheh Shahzamanian
shahzaman@ph1.uni-koeln.de

I hold copyright on the material referred to above, and hereby grant permission for its use as requested herewith. The credit should be given as follows:

Credit: Author, A&A, vol, page, year, reproduced with permission © ESO.



Thierry Forveille
A&A Editor-in-Chief

Astronomy and Astrophysics

Editor in Chief: T. Forveille

T. Forveille

Astronomy & Astrophysics
Observatoire de Paris
61, avenue de l'Observatoire
75014 Paris, France

Tel.: 33 0(1) 43 29 05 41
Fax: 33 0(1) 43 29 05 57
e-mail: aanda.paris@obspm.fr
Web: <http://www.aanda.org>

merging
Annales d'Astrophysique
Arkiv for Astronomi
Bulletin of the Astronomical Institutes
of the Netherlands
Bulletin Astronomique
Journal des Observateurs
Zeitschrift fur Astrophysik
Bulletin of the Astronomical Institutes
of Czechoslovakia

Paris, October 24, 2016

Reprint Permission

Material:

all the figures and tables of the paper Shahzamanian et al. 2016, A&A 593, A131

To be used in:

PhD thesis entitled "Near-Infrared polarimetry in the Galactic Center-on properties of Sagittarius A* and a dusty S-cluster object", University of Cologne

Permission granted to:

Banafsheh Shahzamanian
shahzaman@ph1.uni-koeln.de

I hold copyright on the material referred to above, and hereby grant permission for its use as requested herewith. The credit should be given as follows:

Credit: Author, A&A, vol, page, year, reproduced with permission © ESO.



Thierry Forveille
A&A Editor-in-Chief